6-12-2024

Characterization of Developed QCM Sensors with Novel Topologies, Utilizing Energy Trapping Effect for Improved Mass Sensitivity

Youssef Ezzat Youssef Elnemr
University of Windsor

Characterization of Developed QCM Sensors with Novel Topologies, Utilizing Energy Trapping Effect for Improved Mass Sensitivity

By

Youssef Ezzat Youssef Elnemr

A Thesis
Submitted to the Faculty of Graduate Studies
through the Department of Electrical and Computer Engineering
in Partial Fulfillment of the Requirements for
the Degree of Master of Applied Science
at the University of Windsor

Windsor, Ontario, Canada

2024

Characterization of Developed QCM Sensors with Novel Topologies, Utilizing Energy Trapping Effect for Improved Mass Sensitivity

by

Youssef Ezzat Youssef Elnemr

APPROVED BY:

_____

Y.H. Kim

Department of Civil and Environmental Engineering

_____

M. Azzouz

Department of Electrical and Computer Engineering

_____

A. Emadi, Advisor

Department of Electrical and Computer Engineering

May 17, 2024

DECLARATION OF CO-AUTHORSHIP / PREVIOUS PUBLICATION

I hereby declare that this thesis incorporates material that is result of joint research, as follows:

This thesis includes the outcome of publications which also have co-authors who are/were students supervised by Dr. Arezoo Emadi. The co-authors are Haleh Nazemi, Yumna Birjis, Gian Carlo Antony Raj, Pavithra Munirathinam, Aya Abu-Libdeh, Bruce Ye, and Dr. Arezoo Emadi. In all cases, only primary contributions of the author towards these publications are included in this thesis.

Chapter 2 of this thesis includes a paper published in MDPI Sensors Journal. The paper was co-authored with Aya Abu-Libdeh, Gian Carlo Antony Raj, Yumna Birjis, Haleh Nazemi, Pavithra Munirathinam, and Dr. Arezoo Emadi. Chapter 3-6 of this thesis includes a paper, to be submitted to IEEE Sensors Journal for publication. The paper was co-authored with Gian Carlo Antony Raj, Bruce Le, Mohamed Rinzan, and Dr. Arezoo Emadi. Chapters 6 of this thesis include a paper submitted to the EUROSENSORS Conference. The paper was co-authored with Haleh Nazemi and Dr. Arezoo Emadi.

I am aware of the University of Windsor Senate Policy on Authorship, and I certify that I have properly acknowledged the contribution of other researchers to my thesis and have obtained written permission from each of the co-authors to include the above materials in my thesis.

I certify that, with the above qualification, this thesis, and the research to which it refers, is the product of my own work.

This thesis includes 3 original papers that have been previously published/submitted/under preparation for publication in peer reviewed journals, as follows:

Thesis Chapter	Publication Title	Publication Status
Chapter 2	**Elnemr, Y.E.**; Abu-Libdeh, A.; Raj, G.C.A.; Birjis, Y.; Nazemi, H.; Munirathinam, P.; Emadi, A. "Multi-Transduction Mechanism Technology, an Emerging Approach to Enhance Sensor Performance: A review" MDPI Sensors Journal, 2023	Published
Chapter 3-6	**Elnemr, Y.E**.; Raj, G.C.A.; Ye, B.; Rinzan, M.; Emadi, A. "Characterization of Developed QCM Sensors with Novel Configuration, Leveraging Energy Trapping Effect" IEEE Sensors Journal, 2024	Under Preparation
Chapter 6	**Elnemr, Y.E.**; Nazemi, H.; Emadi, A. "Polymer-coated QCM Sensor Leveraging Energy Trapping Effect for Enhanced Detection of Volatile Organic Compounds" EUROSENSORS Conference, 2024	Submitted

I certify that I have obtained written permission from the copyright owners to include the above published materials in my thesis. I certify that the above materials describe work completed during my registration as a graduate student at the University of Windsor. I declare that, to the best of my knowledge, my thesis does not infringe upon anyone's copyright nor violate any proprietary rights and that any ideas, techniques, quotations, or any other material from the work of other people included in my thesis, published or otherwise, are fully acknowledged in accordance with the standard referencing practices. Furthermore, to the extent that I have included copyrighted material that surpasses the bounds of fair dealing within the meaning of the Canada Copyright Act, I certify that I have obtained a written permission from the copyright owners to include such materials in my thesis.

I declare that this is a true copy of my thesis, including any final revisions, as approved by my thesis committee and the Graduate Studies office, and that this thesis has not been submitted for a higher degree to any other University or Institution.

ABSTRACT

The detection of volatile organic compounds (VOCs) has garnered attention due to its wide-range applications in environmental monitoring, industrial safety, and public health. Among diverse sensing technologies, the quartz crystal microbalance (QCM), a resonator sensor, stands out as a widely used device for mass sensing application, owing to its ability to detect mass changes in the nanogram range. In this thesis, the QCM sensor forms the cornerstone, where a novel configuration termed DAIS, is developed and introduced as a promising approach to enhance the sensing capabilities of QCM sensor. The development of QCM sensors, featuring a unique configuration, involves studying the impact of mass loading area on a 5 MHz AT-cut QCM sensor performance through Finite Element Analysis (FEA). The objective of the conducted study is to identify areas of opportunity where localized energy trapping occurs. Simulation results demonstrate that strategic replacing of conventional topology that features a singular circular electrode, with smaller electrodes leads to improvements in both mass sensitivity and its distribution. This enhancement is attributed to effectively utilizing the identified areas of opportunities for maximizing energy trapping. Theoretical models are validated experimentally the precisely fabricated QCM sensors through the utilization of a fully automated controlled environment system to eliminate the presence of human errors. The acquired shift in resonant frequency serves as indicator for the QCM sensing performance during the characterization process. This involves evaluating the QCM sensors as a standalone device, and further with a polymer sensing layer applied on top of the QCM sensors. The findings reveal that the proposed novel topologies, featuring unique patterns of distributed small electrodes to effectively utilize the energy trapping effect, outperform the conventional QCM design by over 10%. This thesis validates the concept of DAIS, offering a promising avenue for enhancing the sensing capabilities of QCM sensors for next generation sensing technologies to meet evolving current needs for various applications and address the current limitations.

ACKNOWLEDGEMENTS

I would like to express my most sincere appreciation to my advisor Dr. Arezoo Emadi for being supportive and a source of encouragement. It was a great pleasure working under her supervision. I wish to express my sincere thanks to my committee members, Dr. Maher Azzouz, and Dr. Yong Hoon Kim for providing their invaluable guidance and support in reviewing my thesis. A very special thanks to all the members of the e-Minds lab for their invaluable support. Extra special thanks to my family for being such supportive and affectionate human beings. Thank you all for being such supportive and affectionate people.

TABLE OF CONTENTS

DECLARATION OF C0-AUTHORSHIP / PREVIOUS PUBLICATION iii

ABSTRACT vi

ACKNOWLEDGEMENTS vii

LIST OF TABLES x

LIST OF FIGURES xi

LIST OF ABBREVIATIONS/SYMBOLS xvi

CHAPTER 1 **Introduction** 1

1.1 Thesis Contributions 1

1.2 Thesis Outline 2

CHAPTER 2 **Gas Sensors Based on Transduction Mechanisms** 4

2.1 Introduction 4

2.2 Gas Sensors based on Sensing Transduction Mechanisms 4

2.2.1 Capacitive Gas Sensors 4

2.2.2 Rresistive Gas Sensors 6

2.2.3 Piezoelectric Gas Sensors 7

2.2.4 Triboelectric Gas Sensors 9

2.2.5 Comparison of Gas Sensors based on Various Sensing Transduction Mechanisms 11

2.3 Common Gas Sensors for VOCs Detection 12

2.3.1 Metal Oxide Semiconductor Sensor (MOS) 12

2.3.2 Piezoelectric Micromachined Ultrasonic Transducer Sensor (PMUT) 14

2.3.3 Capacitive Micromachined Ultrasonic Transducer Sensor (CMUT) 15

2.3.4 Quartz Crystal Microbalance Sensor (QCM) 18

2.4 Conclusion 19

CHAPTER 3 **Fundamental of the Quartz Crystal Microbalance (QCM)** 21

3.1 Introduction 21
3.2 QCM Principle of Operation and Device Structure 21
3.2.1 Piezoelectricity Theory 22
3.2.2 Quartz Vibration Modes Based on Crystal Cut 25
3.2.3 QCM Resonance Frequency 26
3.2.4 Sauerbrey Assumption Vs Practical Model of QCM Mass Sensitivity 28
3.3 Equivalent Circuit Model of QCM 30
3.3.1 Mechanical Equivalent Circuit of QCM 30
3.3.2 Electrical Equivalent Circuit of QCM 31
3.4 Conclusion 32

CHAPTER 4 **Finite Element Analysis on QCM Mass Sensitivity** 34
4.1 Introduction 34
4.2 COMSOL Multiphysics Setup for QCM Mass Sensitivity Analysis 34
4.3 Effect of Mass Loading Area on QCM Mass Sensitivity 40
4.4 Newly Developed Electrode Configurations Based on Distribution of Mass Loading Area for Improving Mass Sensitivity (DAIS) 47
4.5 Conclusion 53

CHAPTER 5 **Fabrication of Proposed QCM Sensors & Experimental Setup** 56
5.1 Introduction 56
5.2 Fabrication of the Newly Developed QCM Sensors 56
5.3 Controlled Environmental Measurement Setup 61

CHAPTER 6 **Characteriztion of Proposed QCM Sensors** 66
6.1 Introduction 66
6.2 Experimental Process Phase I: QCM as a Standalone Device 66
6.3 Experimental Process Phase II: QCM for VOC Detection 72

CHAPTER 7 **Conclusion and Proposed Future Work** 80

REFERENCES/BIBLIOGRAPHY 82

VITA AUCTORIS 95

LIST OF TABLES

Table 1: Piezoelectric coefficient (d33) of common piezoelectric materials [21] 9

Table 2: Comparison of gas sensors based on various sensing transduction mechanisms. 12

Table 3: Material properties used in COMSOL simulations. [52] 35

Table 4: Conventional design parameters of a 5 MHz QCM used for mesh dependency study. 37

Table 5: Conventional design parameters of a 5 MHz QCM with changing mass loading area coverage from 10% to 100%. 41

Table 6: Conventional design parameters of a 5 MHz QCM with changing mass loading area coverage from 10% to 100%. 44

Table 7: Design parameters of Novelcircular-QCM. 50

Table 8: Comparison of mass sensitivity and its distribution for a 5 MHz QCM with circular and DIAS electrode configurations. 54

Table 9: Regulated flow rates and adjusted RH concentrations injected into the test chamber. 68

Table 10: Adjusted parameters of spinner device. 73

Table 11: Frequency shifts for polymer- coated QCM sensors responding to shift in RH concentration from 0 to 1500 ppm. 74

Table 12: Regulated flow rates and adjusted methanol concentrations injected into the test chamber. 76

Table 13: Regulated flow rates and adjusted ethanol concentrations injected into the test chamber. 78

LIST OF FIGURES

Figure 1. Schematic side-view of the capacitive gas sensor based on changes in the dielectric property when target molecules adsorbed. 5

Figure 2. Schematic depiction of the resistive gas sensor with integrated electrodes (IDE). 6

Figure 3. Schematic depiction of the piezoelectric sensor based on thin films of piezoelectric material (PZT). 8

Figure 4. Schematic depiction of the triboelectric sensor. 10

Figure 5. Schematic side-view of the metal oxide semiconductor (MOS) sensor with a micro heater unit. 14

Figure 6. Schematic depiction of the piezoelectric micromachined ultrasonic transducer (PMUT). 14

Figure 7. Schematic depiction of the capacitive micromachined ultrasonic transducer (CMUT). 17

Figure 8. Schematic depiction of the QCM sensor. 19

Figure 9. Schematic depiction of a QCM, consisting of a quartz crystal sandwiched between a top and bottom electrode. 22

Figure 10. Schematic side-view illustrating the operational mechanism of the QCM, wherein alternating voltage is applied to the electrodes to induce thickness-shear oscillations. 23

Figure 11. Schematic depiction illustrating dipole displacement resulting from the application of a direct current DC field. 23

Figure 12. Schematic depiction of the radial variation in displacement amplitude across the quartz crystal attributed to the energy trapping effect. 28

Figure 13. Schematic depiction of BVD mechanical equivalent model of the QCM, comprising of a mass component ‘M’, spring constant ‘K’ and a dashpot element ‘Y’... 31

Figure 14. Schematic depiction illustration of (a) BVD electrical equivalent circuit (b) Motional components of electrical equivalent circuit..... 32

Figure 15. Schematic depiction of QCM geometry in COMSOL Multiphysics (Not Drawn to Scale)..... 35

Figure 16. Schematic depiction representing diverse meshing sequence of QCM namely (a) Normal mesh (b) Fine Mesh (c) Finer Mesh (d) Extra Fine Mesh (e) User Controlled (swept mesh). 36

Figure 17. 2D plots of the COMSOL mesh dependency analysis results presenting (a) number of meshing elements (b) the resonant frequency obtained for different mesh type. 38

Figure 18. Schematic depiction of a QCM with a mass loading area coverage from 10 % to 100 % (highlighted & not to scale) on the top electrode. 40

Figure 19. 2D plots of from COMSOL simulation results illustrating (a) the frequency shift (kHz) obtained for different values of radius of mass loading area (mm) for an added mass per unit area of 20 µg/mm² (b) the individual frequency shift values for changing radius of mass loading area as the slope of frequency shift vs radius of mass loading area for radii values. 42

Figure 20. Mass loading area coverage is varied for QCM devices with electrode radii values of (a) 1 mm, (b) 1.5 mm, (c) 2.5 mm, (d) 4.25 mm, and (e) 5.5 mm to determine the frequency shift for an added mass per unit area of 20 µg/mm2..... 44

Figure 21. 2D plots of the results from COMSOL simulation illustrating (a) the frequency shift (kHz) obtained for different values of radius of mass loading area (mm) for an added mass per unit area of 20 µg/mm² (b) the individual frequency shift values for changing radius of mass loading area as the slope of frequency shift vs radius of mass loading area for radii values. 46

Figure 22. 2D plot of the results form COMSOL simulation illustrating the individual frequency shift values against the percentage of mass loading area as the slope of

frequency shift vs percentage of mass loading area for electrode radii values 5.5 mm and 1 mm. 48

Figure 23. Schematic depiction of a 5 MHz QCM with conventional circular electrode configuration with a novel radius 2.96 mm, equivalent to inde..... 49

Figure 24. Schematic depiction of a 5 MHz QCM with novel DAIS electrode configuration of outer radius of 2.96 mm comprising of several smaller circular electrodes of radius 0.76 mm. 51

Figure 25. Schematic depiction of a 5 MHz QCM with novel DAIS electrode configuration (second generation) of outer radius of 2.96 mm comprising of a central circular electrode radius of 1.75 mm surrounded by smaller circular electrodes of radius 0.76 mm. 52

Figure 26. Schematic depiction of a 5 MHz QCM with novel DAIS electrode configuration (third generation) of outer radius of 2.96 mm comprising of several smaller circular electrodes of radius 0.62 mm. 53

Figure 27. 2D plots of the results from COMSOL simulation illustrating (a) the mass loading area (mm^2) (b) the frequency shift (kHz) obtained for an added mass per unit area of 20 $\mu g/mm^2$ (c) the mass sensitivity distribution values (d) the mass sensitivity values ($Hz/\mu g\ mm^2$). 55

Figure 28. Schematic depiction of QCM sensor featuring (a) conventional configuration (b) wrap-around configuration. 57

Figure 29. Schematic bottom-view of the proposed QCM design with detailed dimensions in mm. 57

Figure 30. Schematic top-view of the proposed QCM designs with detailed dimensions in mm. 58

Figure 31. Schematic (a) bottom-view (b) top-view of the generated mask used to fabricate the proposed QCM sensors. 59

Figure 32. Schematic depiction of designed QCM device illustrating the layers and material used. 59

Figure 33. Depiction 5 MHz QCMs fabricated with varied topologies (a) Conventional-QCM (b) Novelcircular-QCM (c) DAIS(G1)-QCM (d) DAIS(G2)-QCM (e) DAIS(G3)-QCM. 60

Figure 34. The experimental setup employed to establish the controlled environment necessary to evaluate the sensitivity of the fabricated QCM sensors. 61

Figure 35. Schematic depiction of the Plasmionique FLO07-TSV, used to facilitate the controlled environment necessary to evaluate the sensitivity of the fabricated QCM sensors. 62

Figure 36. Schematic depiction of the designed test chamber , detailing elevation, side, and plan views..... 63

Figure 37. Depiction of the IMM-200 deposition monitor, used to acquire QCM sensor resonant frequency to evaluate the mass sensitivity of the fabricated QCM sensors. 64

Figure 38. Flowchart of the state machine structure in the developed QCMView, illustrating the process from initialization to data storage. 64

Figure 39. 2D plot of experimental results illustrating fundamental resonant frequency for QCM sensor, featuring both DAIS and conventional QCM designs. 69

Figure 40. Bar graph of experimental results revealing the required time to reach saturation levels, which is found to not exceed 800 seconds indicated by the shift in sensors resonant frequencies. 70

Figure 41. 3D plot of experimental results illustrating the responses of QCMs to variations in target analyte RH, which is modulated to follow a distinct pattern. 71

Figure 42. 3D bar graph of experimental results presenting a comparative frequency shift characterization of the candidate QCM designs for RH concentrations 2300, 4600, 6900, 9200, 11500 ppm..... 72

Figure 43. 3D plot of experimental results illustrating the response of both DAIS and conventional QCMs to variation in VOC target analyte methanol. 76

Figure 44. 3D bar graph of experimental results illustrating a Comparative frequency shift characterization for methanol concentrations 12600, 25200, 37800, 50500, and 63100 ppm. 77

Figure 45. 3D plot of experimental results illustrating the response of both DAIS and conventional QCMs to variation in VOC target analyte ethanol. 79

Figure 46. 3D bar graph of experimental results illustrating a Comparative frequency shift characterization for ethanol concentrations 1100, 2300, 3400, 4600, and 5700 ppm. 79

LIST OF ABBREVIATIONS/SYMBOLS

Abbreviation	Explanation
AUC	Area Under Curve
BKG	Background Gases
CNT	Carbon Nanotube
CMUT	Capacitive Micromachined Ultrasonic Transducer
DAIS	Distribution of Area for Improving Mass Sensitivity
FEA	Finite Element Analysis
FBAR	Film Bulk Acoustic Wave Resonator
IDE	Interdigitated Electrodes
MOS	Metal Oxide Semiconductor
PDMS	Polydimethylsiloxane
PMUT	Piezoelectric Micromachined Ultrasonic Transducer
PPM	Part Per Million
PTFE	Polytetrafluoroethylene
PVP	Polyvinylpyrrolidone
QCM	Quartz Crystal Microbalance
RH	Relative Humidity
SAW	Surface Acoustic Wave
VOCs	Volatile Organic Compounds

CHAPTER 1

Introduction

1.1 Thesis Contributions

The interest in VOCs detection has surged due to its wide range of applications, including environmental monitoring, industrial safety, and public health [1], [2], [3], [4]. The VOCs are a diverse group of carbon-containing compounds with low boiling points [5]. The detection of such gases which are presented in relatively low concentrations, reaching to part per million (ppm) level, poses challenges necessitating highly sensitive technologies. Among various technologies that can be differentiated based on transduction mechanisms including piezoelectricity, resistance, capacitance, and triboelectricity, the QCM is widely used as a mass sensor with ability to detect mass changes in the nanogram level [6]. This is achieved based on the principle of piezoelectricity owing to the piezoelectric nature of quartz crystal substrate employed in the QCM structure. The QCM high sensitivity along with the simple structure of the QCM enable its use in diverse applications where the targets present in low concentrations [7], [8], [9], [10].

The primary objective herein is to enhance the QCM mass sensitivity which is indicated by the shift in sensor resonant frequency in response to target gases exposure where the higher frequency shift indicates better sensing capabilities of the QCM sensors [11]. To achieve this objective, FEA in COMSOL simulation is utilized to investigate the impact of energy trapping effect on mass sensitivity [6]. The conducted FEA results show that the utilization of energy trapping effect regions, which is identified as areas of opportunity, for mass loading area atop of the QCM sensor, would potentially enhance mass sensitivity, thereby the QCM sensing performance. Derived from this, 5 MHz QCM sensors, featuring novel electrode configurations are developed based on distribution area for improving mass sensitivity (DAIS) to maximize the energy trapping region, resulting in enhanced mass sensitivity.

The derivative QCM sensors are then fabricated via e-beam technology in order to validate the simulation findings through precisely designed characterization process. This

is achieved by establishing a controlled environment necessary to evaluate the sensors performance. This characterization is divided into two phases that can be differentiated by the presence of an applied sensing layer on top of the QCM sensors. The shift in sensors resonant frequencies in response to varying concentration of target gases is indicative of their sensing performance. The targets gases in the experimental work include relative humidity, methanol, and ethanol and they are chosen to serve as a proof of concept. During the entire development process, including both simulation and experimental work, the conventional QCM sensor is used as a baseline reference. The experimental results demonstrate enhanced mass sensitivity exhibited by the proposed DAIS QCM sensors in comparison with the QCM with a conventional design. This emphasis the FEA findings, where the replacement of the conventional circular electrode by a strategically distributed smaller electrodes to maximize the energy trapping region, yielding enhancements in sensor mass sensitivity. This work offers the concept of DAIS as a promising approach for enhancing the sensing capabilities of QCM sensors across various applications.

1.2 Thesis Outline

In Chapter 1, an introduction is presented to highlight the contribution of this thesis and overview the objectives and the corresponding methodologies in order to achieve the primary objective, which is improved sensing capabilities of QCM sensor.

In Chapter 2, a comparative analysis is conducted on different sensing technologies employed in gas detection. It comprises two main sections: Gas Sensors based on Sensing Transduction Mechanisms, Common Gas Sensors for VOCs Detection. The focus is on reviewing different gas sensors, introducing their transduction mechanisms, merits, and applications.

In Chapter 3, the operational mechanic of the QCM sensor is explored while identifying its design parameters. This chapter comprises two main sections. The first section, Principle of Operation of QCM and Device Structure, covers Piezoelectricity Theory, Quartz Vibration Modes, QCM Resonance Frequency, and the Sauerbrey Assumption vs. Practical Model of QCM Mass Sensitivity. The second section,

Equivalent Circuit Model of QCM, introduces mechanical and electrical equivalent circuits for the QCM, discussing parameters governing its performance.

In Chapter 4, information on simulations conducted for proposed novel designs is presented. Sections cover the COMSOL Multiphysics Setup, where the conducted mesh dependency study and the boundary conditions (physics and electrostatic) are detailed. Effect of Mass Loading Area on QCM Mass Sensitivity, where the section covers the conducted FEA studies to identify the area of opportunity, utilizing the phenomena of energy trapping for mass loading area to improve the QCM sensitivity. The proposed designs were introduced, and their sensitivities and mass sensitivity distributions were investigated and analyzed.

In Chapter 5, the experimental framework is outlined, covering: sensor fabrication, polymer selection and preparation, and the controlled environment used to regulate target gases within test chambers.

In Chapter 6, the experimental results conducted in two phases: Phase I: involves measurements without sensor coating, targeting relative humidity (RH) detection, Phase II: comprises measurements with polymer-coated sensors, detecting three different target gases separately. The evaluation of proposed designs versus the conventional QCM is conducted by analyzing their resonant frequency shift for different target concentration levels.

In Chapter 7, findings from both simulation and experimental works are highlighted. It draws conclusions based on the obtained results and suggests potential opportunities for future work.

CHAPTER 2

Gas Sensors Based on Transduction Mechanisms

2.1 Introduction

The detection of VOCs is crucial due to its various applications, ranging from environmental monitoring and industrial safety to public health [4], [10], [12]. However, it is challenging to detect these volatiles in complex environment due to their low concentration presence [5], [13]. Electronic nose (eNose) technology has emerged as a solution with a promising potential to mimic the mammalian olfactory system for portable and real-time VOC analysis [4], [14]. Through this chapter, Various gas sensors based on varying sensing transduction mechanisms, including capacitance, resistance, piezoelectricity, and triboelectricity, are literately reviewed to identify their structures and working mechanisms. These sensors rely on the interaction between the target gas and the sensor material, causing a change in a measurable parameter that can be mapped to determine the concentration or presence of the target gas [15], [16]. The effectiveness of sensors is evaluated based on several factors, including sensitivity, selectivity, reversibility, accuracy, range of detection, recovery time, and response time [17], [18].

2.2 Gas Sensors based on Sensing Transduction Mechanisms

2.2.1 Capacitive Gas Sensors

Capacitive gas sensor is a type of electrical sensor that operates based on changes in the dielectric constant or dielectric layer thickness of a material when it adsorbs a target molecule [15], [19], [20], [21]. They are composed of electrodes, substrate and active layer that is commonly a dielectric material such as PDMS, as shown in Figure 1 [22].

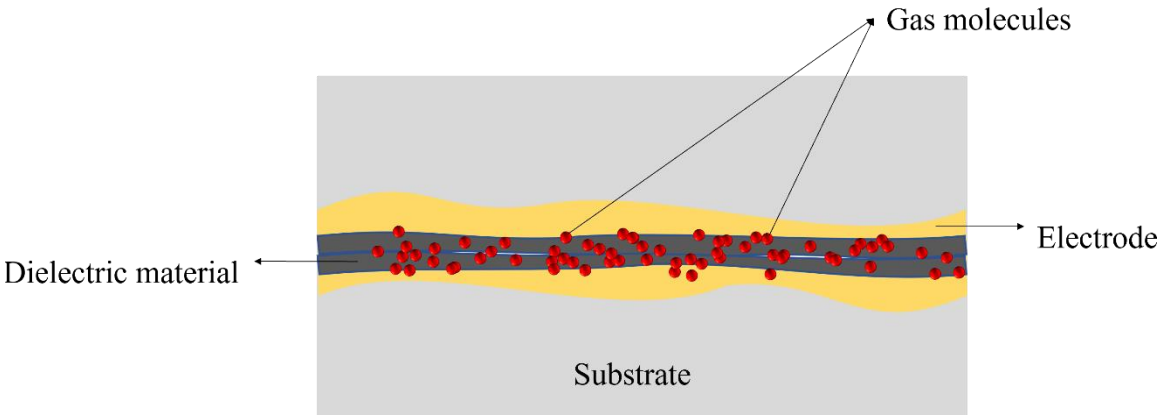

Figure 1. Schematic side-view of the capacitive gas sensor based on changes in the dielectric property when target molecules adsorbed.

When the target gas molecules are adsorbed by the dielectric layer, they cause an electrical deformation that leads to changes in capacitance. This change in capacitance can be used to detect the presence and concentration of the target gas. The governing equation for capacitance-based sensors is given by Equation (1) [19], [21],

$$C = \frac{\varepsilon_0 \varepsilon_r A}{d} \tag{1}$$

where C is the capacitance of the sensor, A is the overlapping area of the two electrodes, d is the separation distance between the electrodes, ε_o is the space permittivity, and ε_r is the relative permittivity of the dielectric material [21].

Capacitive gas sensors offer several advantages, including a simple design and ease of fabrication [15], [21], [23]. However, they have some limitations, including temperature dependency [24]. They are also prone to external electromagnetic interference, affecting the accuracy of the sensors reading [25].

2.2.2 Resistive Gas Sensors

Resistive gas sensor is a type of sensor that operates based on changes in its resistivity. These sensors exhibit simple structure, comprise a substrate and conductive electrodes coated with a sensing material [26], [27]. The sensing material interacts with gas molecules, which cause a change in the resistance of the coated electrodes [28]. This change in resistance can be used to detect the presence and concentration of the target gas. Integrated electrodes (IDEs) are a commonly used in resistive gas sensors, as illustrated in Figure 2 [29], [30].

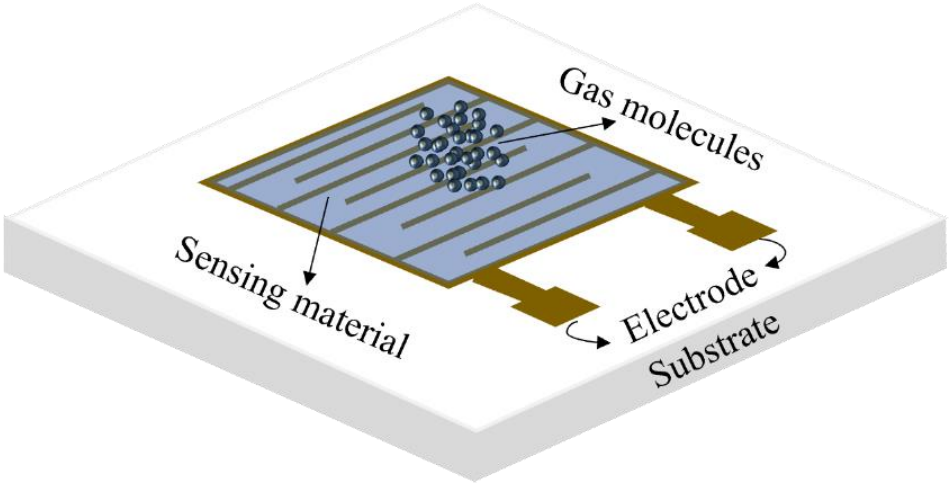

Figure 2. Schematic depiction of the resistive gas sensor with integrated electrodes (IDE).

This change in resistance is then measured and used to identify the presence and concentration of the gas. The operational principle of resistive sensors can be described by two different mechanisms: changes in geometrical parameters and electrical conductor resistance given by Equation (2), or changes in material resistivity given by Equation (3) [15].

$$R = \frac{k}{F} \tag{2}$$

$$R = \frac{\rho l}{A} \tag{3}$$

In Equations (2) and (3), R represents electrical resistance of electrodes, k represents a constant, F represents force, ρ represents material resistivity, l represents the length of the conductor, and A represents area of electrodes.

Resistive gas sensors have simple design and readout mechanism [21], making them candidate for use in portable and wearable devices. However, the gas sensors are sensitive to environmental conditions such as temperature and humidity, necessitating careful calibration and compensation measures [26], [31].

2.2.3 Piezoelectric Gas Sensors

Piezoelectric gas sensor is a type of sensor that utilizes the piezoelectric effect to detect gas molecules. The piezoelectric effect is understood as the linear interaction between mechanical and electrical quantities. Materials offering a pronounced interaction are usually referred to as piezoelectric materials such as lead zirconate titanate (PZT) [21], [32], [33], [34], zinc oxide (ZnO) [21], [35], [36], and barium titanate (BaTiO3) [21], [37]. Figure 3 presents piezoelectric sensor based on thin films to illustrate the design and materials [21], [33].

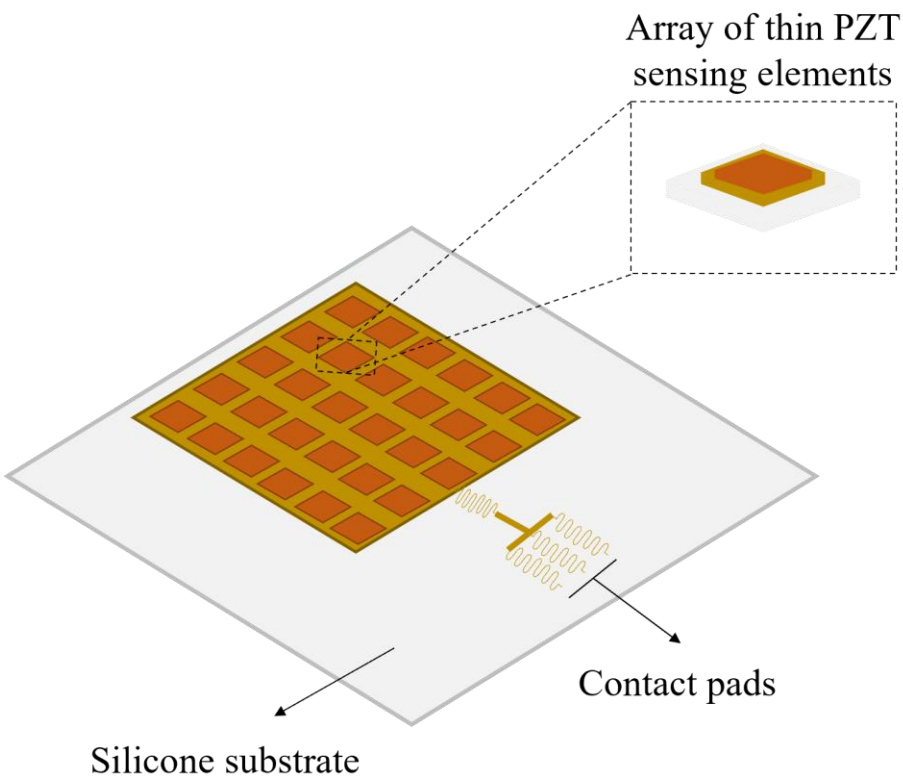

Figure 3. Schematic depiction of the piezoelectric sensor based on thin films of piezoelectric material (PZT).

A mechanical deformation of such material due to an applied mechanical load results in a macroscopic change of the electric polarization. In case of appropriate electrodes covering the material, enabling the measure of electric voltages that are directly related to the mechanical deformation by Equation (4) [15], [21]. The piezoelectric coefficient d_{33}, which is a measure of the sensitivity of the material, can be found in Table 1.

$$V = \frac{d_{33} \times F}{C} \tag{4}$$

where V is the voltage produced by the sensor, C is the capacitance, and F is the force applied to the sensor and the piezoelectric coefficient, d_{33}, which is a measure of the sensitivity of the material, can be found in Table 1.

Table 1: Piezoelectric coefficient (d_{33}) of common piezoelectric materials [21]

Material	$\boldsymbol{d_{33}(pC \cdot N^{-1})}$
PZT	593 [38] / 67 [34]
ZnO	7.5 [39]
BaTiO3	31.1 [40]

Piezoelectric gas sensors notable benefits such as self-powering, fast response time and high sensitivity, making them candidate for gas detection applications [21], [32], [41], [42]. However, they exhibit certain limitations including the vulnerability to noise from vibrations or high-frequency stimuli, and the possibility of sensor response drifting over time. Temperature interference can also affect their performance. Therefore, it is important to take temperature into consideration when interpreting the output of these sensors [21], [23], [32], [42].

2.2.4 Triboelectric Gas Sensors

Triboelectric gas sensor is a type of contact-mode gas sensor that uses triboelectricity to detect the presence of gases [15]. The principle of triboelectrification involves the generation of charges, when two different triboelectric materials come into contact, where electron flow from the positive surface with lower electron affinity to the negative surface with higher electron affinity [15], [21], [43], [44]. After separation, compensating charges are generated at the respective electrodes of each material to

maintain electrostatic equilibrium [21], [45]. Figure 4 presents triboelectric sensor to illustrate the design and materials [46].

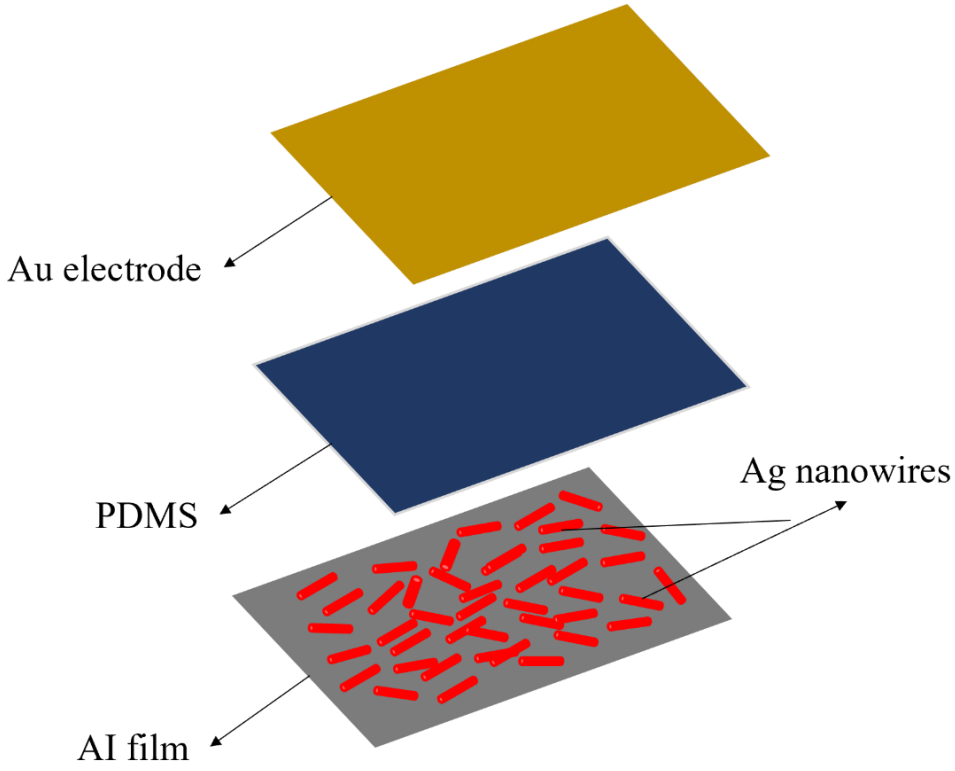

Figure 4. Schematic depiction of the triboelectric sensor.

An external circuit connected to both electrodes allow for the flow of electrons between them, which can be amplified by increasing the contact area of the materials and by having a high separation-distance change [21], [45].

Polydimethylsiloxane (PDMS) [46], Polyvinyl chloride (PVC), polytetrafluoroethylene (PTFE), and fluorinated ethylene propylene (FEP) are examples of triboelectric [15], [47]. The micro-structuring of these materials can be explored to increase the friction area and, therefore, the triboelectrification [21], [48], [49]. Furthermore, when mixing nanoparticles in a polymeric matrix, the composite acquires a

different permittivity and surface electrification compared to the bare polymer, thus changing its triboelectric potential [21].

Triboelectric gas sensors offer advantages such as self-powering and ability to detect gas molecules [21], [49]. However, the principle of triboelectrification itself is a challenge to quantitatively observe and predict, given the variety of factors that can influence it, including the type and composition of the materials, the humidity and temperature of the environment, and the speed and pressure of the contact between the materials [15], [50].

2.2.5 Comparison of Gas Sensors based on Various Sensing Transduction Mechanisms

Table 2 compares gas sensors that employ diverse sensing transduction mechanisms, as discussed earlier in section 2.2. Each of these transduction mechanisms exhibits unique advantages and drawbacks, thus rendering them differently suitable for diverse applications based on specific requirements.

Table 2: Comparison of gas sensors based on various sensing transduction mechanisms.

Gas Sensors	Advantages	Disadvantages
Capacitive	Simple governing equation and design, ease of fabrication [15], [21], [23]	Temperature dependency [24], Prone to external electromagnetic interference, affecting the accuracy of the sensors reading [25].
Piezoresistive	High sensitivity [31], very simple design and readout mechanism [21]	Highly sensitive to environmental conditions temperature, requiring calibration and compensation measures [26], [31].
Piezoelectric	Self-powering, fast response time, high sensitivity [21], [32], [41], [42]	Inability to detect static pressure [42], vulnerability to noise from vibrations or high-frequency stimuli, possibility of sensor response drift over time. Temperature interference can also affect performance.
Triboelectric	Self-powering, ability to detect dynamic pressures [21], [48]	Variety of factors that can influence performance, including type and composition of materials, humidity and temperature of environment, and speed and pressure of contact between materials [15], [50].

2.3 Common Gas Sensors for VOCs Detection

2.3.1 Metal Oxide Semiconductor Sensor (MOS)

Metal oxide semiconductor (MOS) sensors, which incorporate metal oxides as their sensing materials and a micro heater unit [51], [52]. These sensors are preferred due

to their low cost, simple preparation methods, and exceptional physical and chemical properties [53], [54]. At the nanoscale, MOSs exhibit unique properties, including significant changes in electrical properties that make them widely used gas sensors [53], [55], [56]. Moreover, they are capable of exhibiting high stability and quick response in harsh and high-temperature environments [53], [57]. The popularity of MOS sensors is further attributed to their low-cost manufacturing processes [53], [58].

There are two main types of semiconducting metal oxide-based sensors: n-type whose majority carrier is an electron such as TiO2, ZnO, SnO_2 and WO_3, and p-type whose majority carrier is a hole such as NiO, $Mn_3O_4$and Cr_2O_3 [59]. MOS-based gas sensors function based on an equilibrium shift of the surface reactions associated with the target analyte [51]. Reducing gases such as NH_3, CO, H_2, HCHO increase conductivity for n-type semiconductors and decrease conductivity for p-type semiconductors. Conversely, oxidizing gases such as NO_2, O_3, C_{l2} have the opposite effect [51]. The p-type MOS has advantages, including low humidity dependence [51], [60] and high catalytic properties [51], [61]. However, the integration of a micro heater unit in MOS gas sensors results in complex geometries that require electrical isolation areas in the design, as shown in Figure 5 [59].

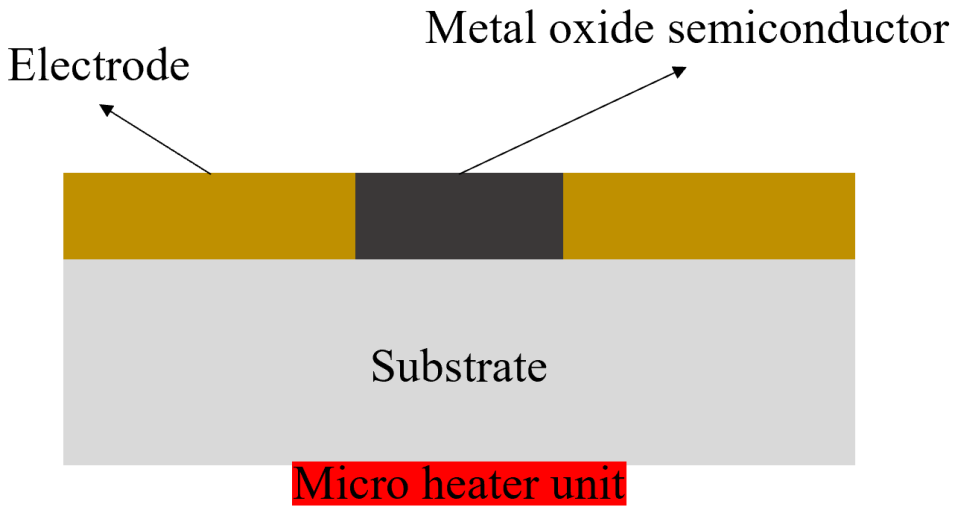

Figure 5. Schematic side-view of the metal oxide semiconductor (MOS) sensor with a micro heater unit.

2.3.2 Piezoelectric Micromachined Ultrasonic Transducer Sensor (PMUT)

The piezoelectric Micromachined Ultrasonic Transducer (PMUT) is a device that utilizes the piezoelectric effect to detect gas molecules. The sensor's structure includes a piezoelectric membrane that is deflectable and sandwiched between a top and bottom electrode, as shown in Figure 6 [62], [63]. The edges of the structure are clamped. Applying an AC voltage to the top electrode causes the piezo layer to vibrate at its resonant frequency due to the piezoelectric effect [62], [64].

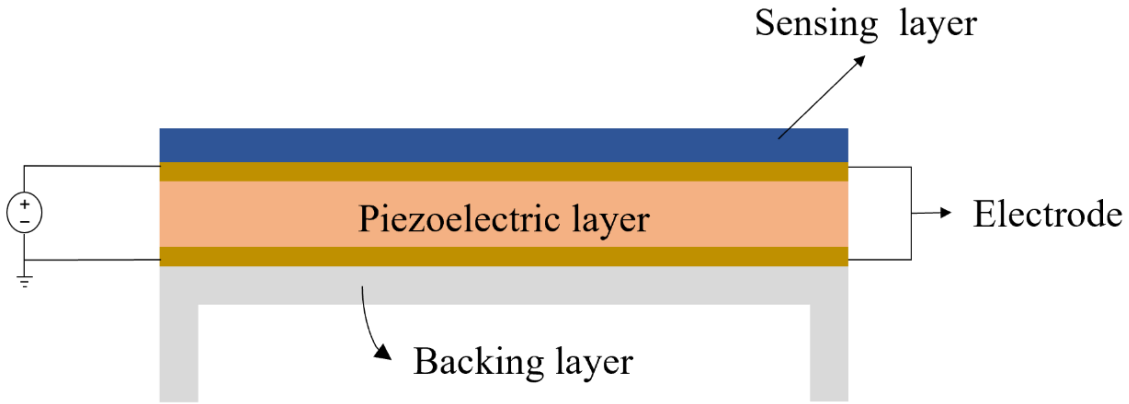

Figure 6. Schematic depiction of the piezoelectric micromachined ultrasonic transducer (PMUT).

PMUT sensor uses frequency shift as an output, achieved unconventionally by using the direct piezoelectric effect. This can be accomplished by placing a sensing layer on top of the PMUT structure [62]. When PMUT sensor is exposed to target gas, the sensing layer undergoes a mass change due to analyte gas molecule adsorption. As a result, stress is produced on the piezoelectric layer, resulting in a shift in the resonant frequency estimated by the Equation 5 [52]. The resonant frequency and sensitivity of the PMUT sensor are predominantly determined by the sensing layer's material.

$$\Delta f = -\frac{f_0}{2}\frac{\Delta m}{m} \tag{5}$$

where Δf represents the resonant frequency shift, f_0 represents the fundamental resonant frequency, Δm is the change in mass and m denotes the mass of the piezoelectric layer. This change in resonant frequency is utilized to evaluate the sensitivity of the device.

PMUT sensor offers several advantages, including the ability to operate at lower voltages [62] and achieve higher sensitivity potential [52], [62], [65], [66]. Moreover, The PMUT sensor has an inherent electromechanical coupling due to its piezoelectric nature, and it does not require a DC bias voltage for its operation [52], [67]. Consequently, the PMUT does not necessitate an intricate or complex fabrication process [52], [68].

2.3.3 Capacitive Micromachined Ultrasonic Transducer Sensor (CMUT)

The Capacitive Micromachined Ultrasonic Transducer (CMUT) was originally developed for medical and underwater ultrasonic imaging but can be utilized for mass sensing, including gas detection [62], [69], [70]. A typical CMUT comprises numerous vacuum-backed resonating membranes connected in parallel, actuated by electrostatic

forces. Its inherent properties and manufacturing advantages make it a suitable device for gas detection [62]. Resonant characteristics of a CMUT are mainly determined by the mechanical properties and dimensions of the resonating membrane. For a circular membrane, the resonant frequency f_0 is expressed by [71]:

$$f_0 = \frac{0.83}{a}\sqrt{\frac{Et^3}{m(1-v^2)}} \tag{6}$$

where t, a, m are the thickness, the radius, and the mass of the membrane respectively. E is the Young modulus. v is the Poisson ratio.

Due to the unique structure of the CMUTs, as shown in Figure 7 [62], they can also act as a mass resonant sensor [62]. Therefore, in an unconventional approach, they are proposed to be used for VOC detection applications. A CMUT benefits from a simple parallel plate structure and, as a gas sensor, it can be functionalized by depositing a polymer sensing layer. The designed sensing material absorbs the gas molecules and hence, the sensor reacts to a change in the sensing layer mass when exposed to target gas molecules.

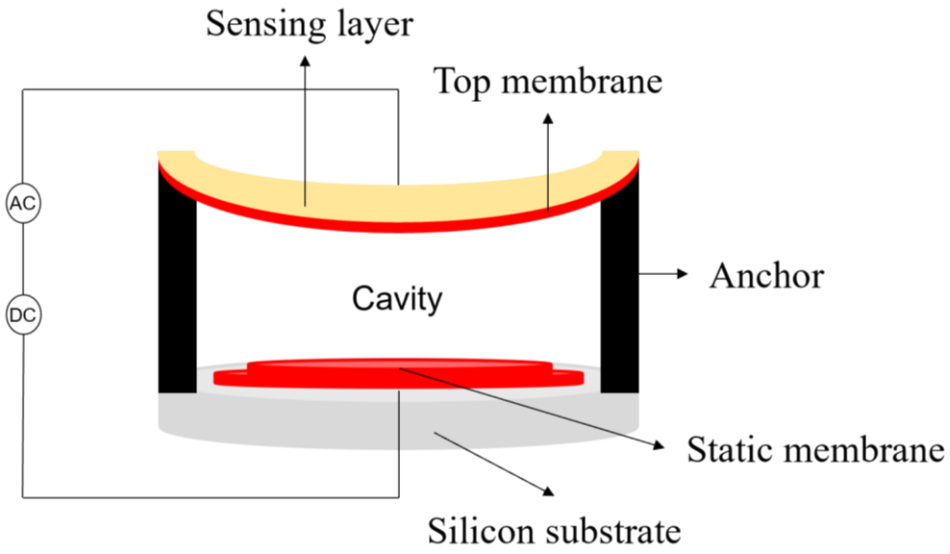

Figure 7. Schematic depiction of the capacitive micromachined ultrasonic transducer (CMUT).

In this design, a DC bias voltage is applied to the top membrane, while the bottom electrode is grounded and shorted. When used as a gas sensor, the top membrane is functionalized by a sensing material. Various polymers can be used as sensing materials in gas sensing applications including polyisobutylene (PIB) [62], [72] and polydimethylsiloxane (DKAP) [62], [73]. When a CMUT gas sensor is exposed to a target gas, the sensing material adsorbs gas molecules, altering the effective mass and thickness of the top membrane, causing a shift in the device's central resonant frequency, as shown in Equation (7), which can be correlated to the target gas molecule concentration level [62].

$$\omega_r = 2\pi f_r = \sqrt{k/m_m} \tag{7}$$

where m_m, f_r represent the effective mass of the membrane, the central resonant frequency of the device respectively [62].

2.3.4 Quartz Crystal Microbalance Sensor (QCM)

Quartz Crystal Microbalance is a mass sensor that is widely employed for the detection of target gases in various applications [59], [74]. The inverse of piezoelectric effect is operated by the QCM gas sensor to detects analytes based on change in frequency due to an added mass on top of sensing electrode, which is referred to be the active area [52], [75]. When the AC voltage is applied on the top electrode and the bottom electrode is grounded, a mechanical deformation is produced, causing the crystal to thickness shear mode of oscillation at the resonant frequency [59]. The resonant frequency can be determined by [59],

$$f_0 = \frac{\sqrt{\mu_q/\rho_q}}{2t_q} \tag{8}$$

where f_o is the resonant frequency of the resonating quartz crystal, μ_q is the shear modulus of the quartz crystal 2.947 × 1011 $g \cdot cm^{-1} \cdot s^{-2}$, ρ_q is the density of the quartz crystal 2.648 × $g \cdot cm^{-3}$ and t_q is the thickness of the quartz crystal. Since μ_q and ρ_q are constant values, the resonant frequency is directly influenced by the thickness of the quartz crystal [59].

This resonant frequency f_0 of the quartz changes either by addition or removal of the mass on the electrically active sensing area. This mass and frequency relation is devised in an equation by Sauerbrey [59],

$$\Delta f = -S_c \frac{\Delta m}{A} \tag{9}$$

where A is the area of electrodes of the QCM, Δf is the change in the resonant frequency, S_c is the Sauerbrey constant equals to 2.264 × 10-6 $g^{-1} \cdot cm^{-2} \cdot s$ and Δm is the change

in mass on the surface of electrode. The negative sign denotes the reduction in the resonant frequency by addition of mass on the top of electrode [59].

The QCM sensor comprises an AT cut quartz substrate sandwiched between the two electrodes made if gold or silver, with chromium used as the adhesive layer for the electrodes and substrate, as shown in Figure 8 [59]. Gold is preferred as the electrode material due to its high conductivity and inertness property [52].

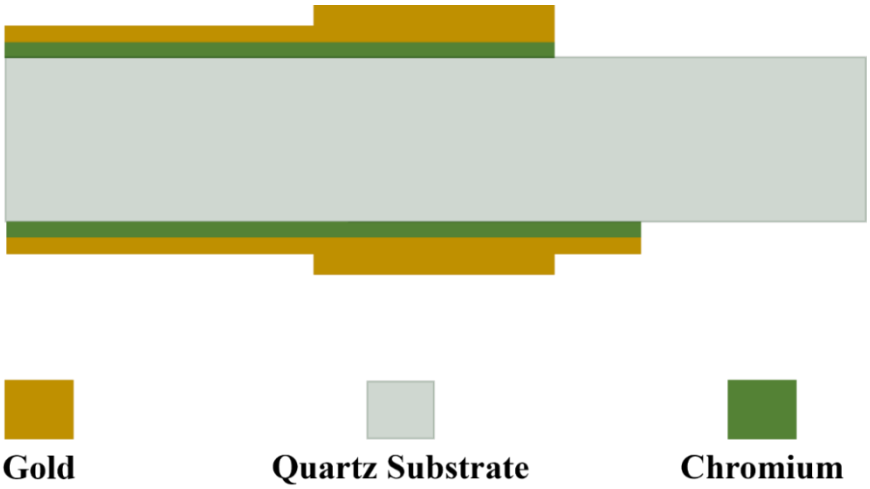

Figure 8. Schematic depiction of the QCM sensor.

The QCM sensor's simple design allows for easy modifications and has the potential to detect multiple gas targets simultaneously in the array configuration. Additionally, the QCM sensor is preferred in practical applications due to its sensitivity, simple geometry, and low cost of fabrication while maintaining gas sensing performance [59].

2.4 Conclusion

Through a comprehensive analysis of commercial and common gas sensors, the advantages and disadvantages of each individual sensor are evaluated and interpreted.

The analysis reveals that various gas sensors can be utilized to detect volatiles; however, there are specific quality requirements for sensor performance in complex environments. Of all the investigated sensors, the quartz QCM exhibits promising competitive advantages, including long lifetime, robustness, simple design, ease of fabrication, and low cost of fabrication. Therefore, the research objective in this work is to enhance the sensing performance of the QCM by investigating different electrode configurations and developing a novel approach to design advanced electrode configurations for detecting volatiles in complex environments.

CHAPTER 3

Fundamental of the Quartz Crystal Microbalance (QCM)

3.1 Introduction

The QCM has emerged for gravimetric sensing applications in both liquid and gas phases [8], [76]. Founded upon the principle of resonant frequency variation due to added mass, the QCM has evolved to detect analytes in gas sensing applications across diverse domains such as environmental monitoring [77], thin film deposition [78], etching analysis [79], and biochemical applications [80]. This chapter expounds upon the theoretical framework of the QCM, and further studies the operational mechanism, design parameters, materials, and structure of the QCM. The primary objective of exploring the theoretical framework of the QCM is to identify the knowledge gap in enhancements of QCM sensor technology, while understanding its potential in detecting volatile organic compounds.

3.2 QCM Principle of Operation and Device Structure

The conventional structure of a QCM includes an AT cut quartz crystal as the primary piezoelectric layer. This AT cut quartz crystal is sandwiched between two metal plates [11], [81], as illustrated in Figure 9. These metallic plates serve as the upper and lower electrodes, receiving an alternating voltage for its operational function. The upper electrode serves as the sensing component, while the lower electrode functions as the reference point [11], [81].

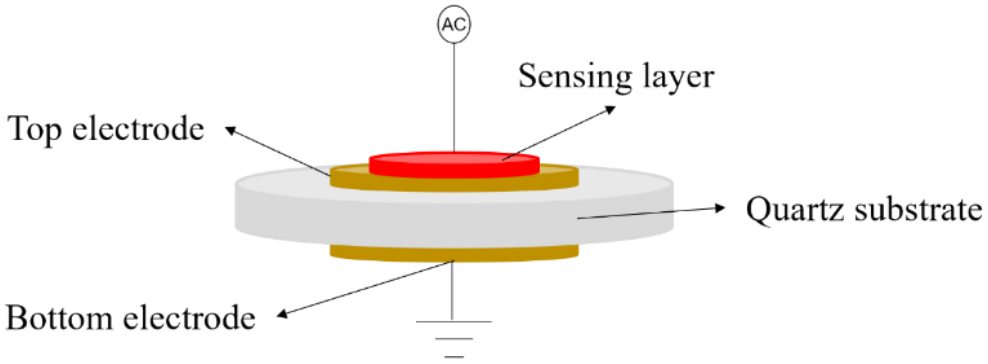

Figure 9. Schematic depiction of a QCM, consisting of a quartz crystal sandwiched between a top and bottom electrode.

For the active electrodes of the QCM, metals such as gold or platinum are commonly favored due to their high conductivity and non-reactive characteristics [82]. Gold is commonly preferred due to its cost-effectiveness in comparison to platinum. In addition, gold possesses desirable attributes like malleability, conductivity, and inertness, making it a prevalent choice in commercial QCM applications. While gold finds extensive usage, alternative metals such as silver and aluminum have also been experimented with as electrode materials for investigating corrosion-related phenomena [83].

3.2.1 Piezoelectricity Theory

The QCM functions based on the principle of piezoelectricity, wherein it undergoes deformation upon the application of an alternating voltage to the crystal [78], [84], as depicted in Figure 10.

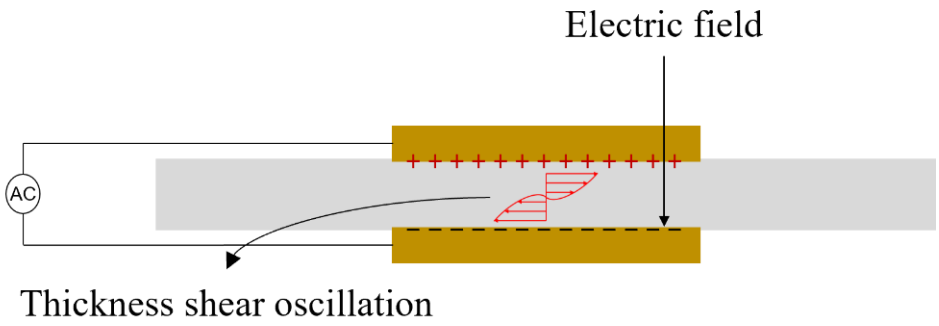

Figure 10. Schematic side-view illustrating the operational mechanism of the QCM, wherein alternating voltage is applied to the electrodes to induce thickness-shear oscillations.

The piezoelectric effect describes the ability of a material to generate an electric charge in response to mechanical stress[15], [85]. In the QCM, the inverse piezoelectric effect is utilized for mass sensing: an electric field induces mechanical stress, causing the quartz crystal to vibrate with fundamental resonant frequency and the change in its frequency is indicative for added mass. Initially, the quartz crystal's structure possesses a random dipole moment [86]. However, upon the application of a DC electric field (poling), polarization occurs, aligning the dipoles in a specific direction, resulting in the crystal's piezoelectric behavior as depicted in Figure 11 [86].

Figure 11. Schematic depiction illustrating dipole displacement resulting from the application of a direct current DC field.

The QCM employs the AT-cut quartz operating in the d_{31} mode, where 'd' signifies the piezoelectric coefficient [87]. This constant represents the ratio between the charge generated in the thickness (k-direction) and the stress applied across the length (i-

direction). In the d_{31} mode, the voltage is applied in the thickness direction (k-direction) or 3-direction, while stress is exerted in the length direction (i-direction). Contrarily, in modes like d_{33}, both voltage and stress occur in the thickness direction [52], [88].

The fundamental equations governing piezoelectric transduction are represented as follows in Equations (10) and (11):

$$D = dT + \varepsilon^T E \tag{10}$$

$$S = s^E T + d^t E \tag{11}$$

where D denotes electric displacement, d is piezoelectric coefficient, d^t is the piezoelectric constant, T represents stress, E stands for electric field intensity, ε^T is the related dielectric constant, S denotes strain, and s^E indicates compliance.

The quartz crystal consists of two electrodes: the sensing electrode (top) and the reference electrode (bottom). To measure the resonant frequency, these electrodes are connected to an impedance analyzer utilizing a series-through method. Conductance of the QCM is measured across frequencies near its theoretical resonant frequency. The frequency corresponding to maximum conductance is recorded as the device's resonant frequency. This increase in conductance is attributed to amplified piezoelectric polarization, causing heightened vibrational amplitude and an accompanying rise in current drawn by the electrodes at resonance [89].

A recently developed technique for determining the resonant frequency is the ring-down or dissipation method [90], [91]. In this approach, the QCM is momentarily excited to its expected resonant frequency by applying a driving voltage. Subsequently, upon discontinuing the excitation, the resonance decay is assessed by monitoring the

reduction in current across the electrodes over time [92]. Through numerical equations correlating the decay curve to vibration amplitude, the resonant frequency and dissipation factor of the QCM can be determined [93].

3.2.2 Quartz Vibration Modes Based on Crystal Cut

The angular orientation of a quartz crystal's principal axis significantly impacts its properties [94]. These properties encompass the vibration mode, temperature coefficient, which moderates temperature's frequency effect, and frequency stability defined as the ratio of stored to dissipated energy [94], [95]. Prominent crystal cuts comprise the AT cut, BT cut, and SC cut. The BT cut is acquired by cleaving a quartz crystal at a 49° angle to the z-axis, yet its frequency stability is relatively inferior to AT and SC cuts [96]. The AT cut, generated by sectioning the quartz at a 35°25’ angle to the z-axis, facilitates anti-parallel motion of crystal surfaces, yielding thickness-shear oscillations [97].

AT cut crystals exhibit a notably low temperature coefficient, ensuring resonance stability at 0 to 50°C [98], [99]. This renders them preferable for room-temperature gas and liquid sensing. SC cut quartz serves as an AT cut alternative, boasting high frequency stability during thickness-shear oscillations [100]. However, the SC cut demands dual rotations about its axes (21.9°, 33.9°) and extra blank-cutting steps, resulting in a more arduous production compared to the AT cut [101]. Although QCM sensors exhibit stability at room temperature, humidity in the detection environment induces frequency drift [102]. To counter this, recent efforts employ artificial neural networks for post-processing measured data, effectively mitigating humidity-induced variance [103]. Additionally, during the evaluation process of QCM sensor it is important to maintain the humidity level to ensure that fair evaluation.

3.2.3 QCM Resonance Frequency

The resonant frequency of the QCM, generated through the application of voltage in accordance with the piezoelectric principle, is termed as its mechanical oscillating frequency [104], [105]. For bulk piezoelectric materials like AT-cut quartz crystal, resonance transpires when the crystal's thickness equals an odd multiple of half the wavelength of the propagating wave. Thus, the resonant frequency can be expressed by Equation (12):

$$f = N\frac{v_q}{2t_q} = Nf_0 \tag{12}$$

where N represents the harmonic overtone number, v_q is the wave velocity in quartz (3340 m/s), t_q is the quartz thickness, and f_0 is the fundamental resonant frequency.

Frequencies apart from the natural oscillation frequency of the quartz are known as harmonic overtones and are harnessed to elicit higher resonant frequencies for the QCM. This approach enables the QCM to attain frequencies as high as 100 MHz without altering the quartz crystal's thickness [105]. While other approach has employed high-frequency QCMs in the range of 70–100 MHz for liquid phase sensing applications [106]. The fundamental resonant frequency f_0 can also be represented by Equation (13), where μ_q is the shear modulus of the quartz crystal, ρ_q is the quartz crystal density, and t_q is the quartz thickness.

$$f_0 = \frac{\sqrt{\mu_q/\rho_q}}{2 \cdot t_q} \tag{13}$$

QCM is used in gravimetric analysis, where the addition of mass on the quartz crystal induces strain on its surface [84], [107]. This strain leads to a change in the resonant frequency, which adheres to Sauerbrey's Equation (14):

$$\Delta f = -\frac{2f_0^2}{A\sqrt{\rho_q \mu_q}}\,\Delta m \tag{14}$$

where f_0 is the fundamental resonant frequency, A represents the active area of the quartz crystal situated between the electrodes, and Δm signifies the alteration in mass on the QCM surface due to analyte absorption.

An assumption in Sauerbrey's equation is that the added mass due to analyte interaction is considered an augmentation in the quartz's strain. Hence, Sauerbrey's equation can be simplified as presented in Equation (15), with C as the constant representing the quartz crystal property. For a conventional 5 MHz QCM operating at room temperature, the value of C is approximately 17.7 $ng \cdot cm2\ /\ Hz$ [108]:

$$\Delta f = -C \cdot \Delta m \tag{15}$$

QCM can function at elevated frequencies, ranging from 50 MHz to several hundred MHz, by operating in its harmonic overtone. In this mode, Sauerbrey's equation considers the harmonic overtone number N, which is an odd integer such as 1, 2, or 3, as demonstrated in Equation (14) [109]. When utilized in the overtone mode, the frequency shift obtained is N times the frequency shift of the fundamental mode.

3.2.4 Sauerbrey Assumption Vs Practical Model of QCM Mass Sensitivity

The mass sensitivity, denoted as 'S,' of a QCM is defined as the alteration in its resonant frequency resulting from an increase in mass due to interaction with a target analyte. This relationship can be expressed by Equation (16).

$$S = \frac{\Delta f}{\Delta m} \tag{16}$$

Sauerbrey's equation postulates that the accumulated mass on the QCM is analogous to a change in the effective mass of the quartz itself. It asserts that the mass absorbed rigidly by the quartz has an impact on the QCM's resonant frequency, with the frequency change influenced by the quantity of mass deposited on the QCM [107], [110]. An additional assumption tied to Sauerbrey's equation assumes even distribution of mass sensitivity across the active electrode area [6]. Nevertheless, observations indicate that vibration amplitude peaks at the electrode center (R=0) and diminishes in a Gaussian pattern towards the electrode edges (Rn), as illustrated in Figure 12.

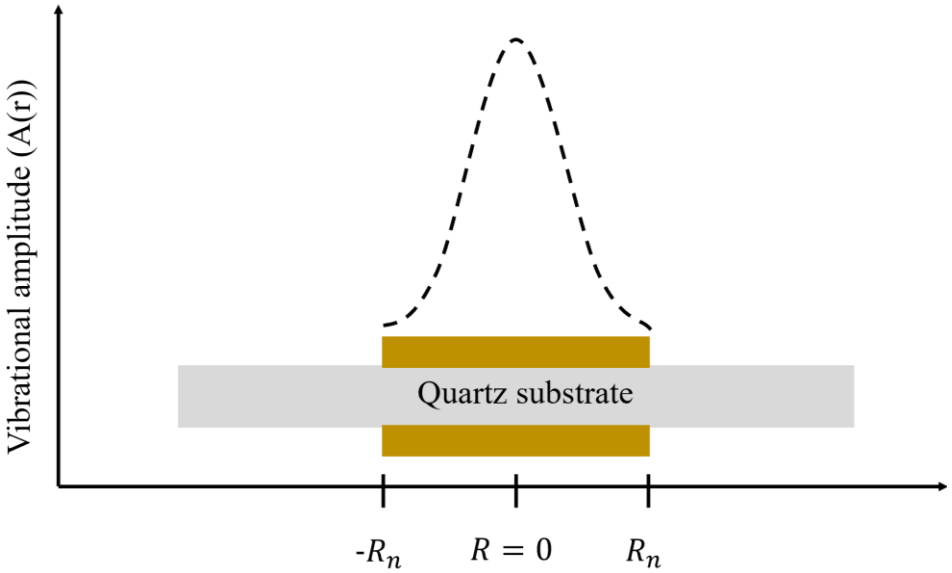

Figure 12. Schematic depiction of the radial variation in displacement amplitude across the quartz crystal attributed to the energy trapping effect.

This outcome stems from the energy trapping effect [6], [111], a phenomenon resulting from internal reflection of bulk waves within the quartz region sandwiched between the electrodes. This effect governs the radial distribution of mass sensitivity across the QCM electrode, commonly referred to as uniformity or mass sensitivity distribution, and contributes to the frequency stability of the AT-cut quartz crystal by constraining vibration closer to the device's center [111].

Huang et al. introduced a practical model to describe the energy trapping effect and determine QCM sensitivity based on Sauerbrey's mass sensitivity function [112].

$$S_f(r,\theta) = -\frac{|A(r,\theta)|^2}{2\pi \int_0^\infty r|A(r,\theta)|^2 dr} \times C_f \tag{17}$$

where $S_f(r,\theta)$ represents the mass sensitivity function, C_f is the Sauerbrey's sensitivity constant 17.7 ng·cm²/Hz, and $A(r,\theta)$ is the particle displacement amplitude, where r signifies radial distance from the center. This practical model emphasizes that mass sensitivity is influenced by electrode size and radial distance from the center.

Both the practical model and Sauerbrey's mass sensitivity equation indicate that the frequency change due to added mass is inversely linked to QCM's radius and mass loading area. Consequently, a smaller electrode could offer higher mass sensitivity, although this entails the drawback of limited analyte interaction due to reduced mass loading area. In real-time sensing scenarios, a larger mass loading area fosters increased analyte interaction with the QCM, thereby yielding a more pronounced shift in resonant frequency [6], [113].

For a deeper exploration of energy trapping's influence on mass sensitivity and its distribution across the QCM electrode, Chapter 4 employs FEA in Multiphysics simulations. The depicted uniformity distribution across the QCM surface in Figure 13 demonstrates an upsurge in radial mass sensitivity within regions of energy trapping accumulation. This phenomenon undergoes further investigation within this thesis to assess the sensing performance of diverse electrode configurations.

3.3 Equivalent Circuit Model of QCM

The operation of a QCM relies on the generation of an electric field resulting from the application of an alternating voltage across its electrodes. The varying voltage across these electrodes gives rise to an electric field that, in turn, induces a current. The ratio of the applied voltage to the induced current is defined as the electrical impedance [105], [114]. Therefore, it becomes essential to establish an electrical model for piezoelectric elements, incorporating their electromechanical effects into electrical circuits. One notable model used for this purpose is Butterworth Van Dyke (BVD) model, which represents a mechanically oscillating system driven by an electrostatic source through an equivalent circuit representation. The BVD model finds applicability in characterizing the unloaded QCM in terms of both electrical and mechanical components [115], [116].

3.3.1 Mechanical Equivalent Circuit of QCM

The mechanical equivalent circuit in BVD model , as illustrated in Figure 13, consists of an inertial mass component denoted as 'M,' which is linked to two branches. Each branch comprises a spring constant represented by 'K' and a dashpot element represented by 'Y.'

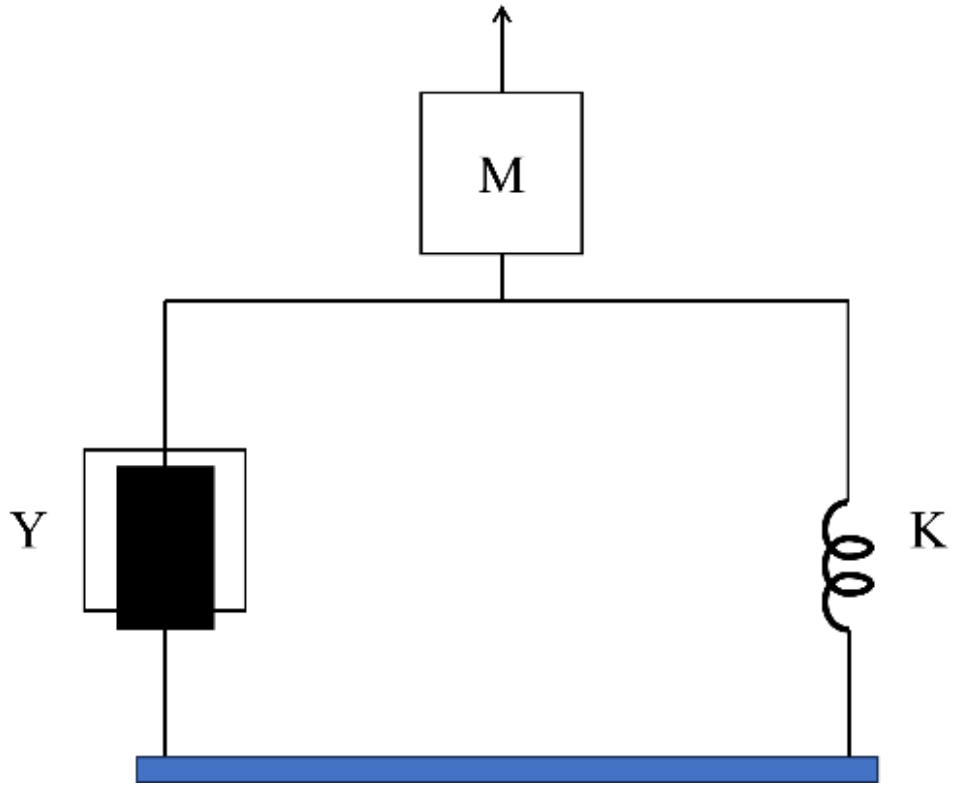

Figure 13. Schematic depiction of BVD mechanical equivalent model of the QCM, comprising of a mass component ‘M’, spring constant ‘K’ and a dashpot element ‘Y’.

where 'M' signifies the inertial mass, 'K' symbolizes the stored energy accumulation during oscillation, and 'Y' represents the dissipated energy during the operational process [104], [117].

3.3.2 Electrical Equivalent Circuit of QCM

The parallel branch in Figure 14 is composed of a singular capacitance element denoted as 'Cp', which signifies the unchanging or steady dielectric capacitance intrinsic to the QCM. Concurrently, the series arrangement of the RLC components forms a parallel branch with Cp branch, representing the dynamic attributes of the QCM's motion-related characteristics [115]. In this context, 'R' symbolizes the energy dissipation during oscillation, a consequence of factors such as inherent friction and external

damping from the quartz housing. Moreover, 'Cs' denotes the energy stored within the oscillation process, while 'L' represents the mass-related inertial component linked with the motional impedance [115], [118].

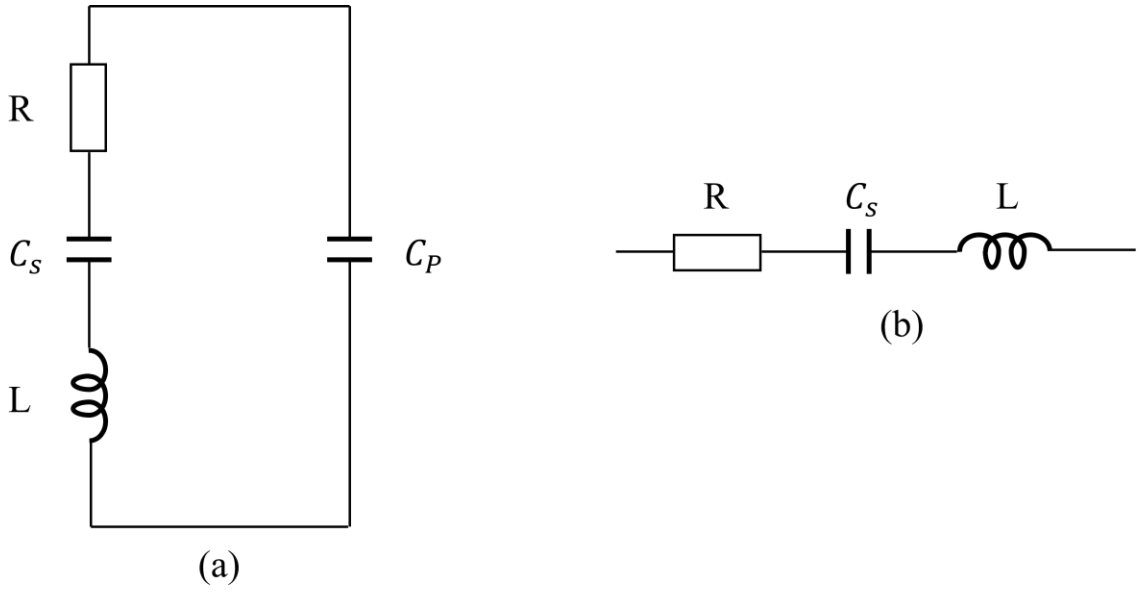

Figure 14. Schematic depiction illustration of (a) BVD electrical equivalent circuit (b) Motional components of electrical equivalent circuit.

3.4 Conclusion

In this chapter, an investigation is carried out into the theory, operational mechanism, and structural configuration of the QCM. It is presented as a piezoelectric device that operates based on the thickness-shear oscillations of a quartz crystal. The inverse piezoelectric effect, a fundamental principle of quartz crystals, is discussed, along with the pertinent governing equations that significantly influence the operation of the QCM. Employing both a mechanical model and an electrical BVD model, an equivalent circuit model is introduced to understand the functionality of the QCM. Diverse electrode configurations of the QCM are introduced and analyzed based on their advantages and their applicability in gravimetric sensing.

The utilization of Sauerbrey's equation is a key aspect in establishing the relationship between changes in resonant frequency and alterations in mass on the quartz crystal. This equation elucidates how the resonant frequency is contingent upon both the physical properties of the quartz crystal and the added mass. A fundamental precondition of this equation is the assumption that the mass deposited onto the QCM is uniformly spread across the electrode area. The term mass sensitivity denotes the ratio of the change in resonant frequency due to the added mass, and it serves as a crucial metric to quantify the sensing performance of the device. The distribution of mass sensitivity across the QCM surface exhibits a Gaussian characteristic, attributed to the accumulation of acoustic energy within the quartz crystal. This phenomenon is a consequence of the energy trapping effect, and the corresponding parameter dictating the radial distribution of mass sensitivity is referred to as 'mass sensitivity distribution.' The distribution of mass sensitivity is found to be directly proportional to the amplitude of particle displacement across the QCM surface. This correlation is subsequently exploited to harness the energy trapping effect, thereby enhancing the sensing capabilities of the QCM. To analyze the resonant frequency and mass sensitivity of the QCM, Multiphysics simulations are conducted, and the outcomes of these simulations will be expounded upon in the upcoming chapters.

CHAPTER 4

Finite Element Analysis on QCM Mass Sensitivity

4.1 Introduction

In Chapter 3, various parameters are introduced that affect the performance of the QCM, determining the natural oscillating frequency of the QCM, which's in turn influence the QCM mass sensitivity. These parameters involve the quartz crystal cutting angle, thickness, and radius, as well as the electrodes' thickness, radius, and material. Among these parameters, the Mass Loading Area (MLA) on top electrode of the QCM was reported to be as key factor in influencing the device's sensing performance [1]. The energy trapping effect within the QCM leads to concentrated energy in specific regions, resulting in a higher frequency shift and consequently, increased mass sensitivity in those regions atop of the sensing electrode. Identifying these regions would potentially enhance the QCM's response. This chapter employs Finite Element Analysis to identify the areas of opportunity, where energy trapping occurs and investigate the impact of utilizing such regions for mass loading area on the QCM's mass sensitivity by analyzing the device's resonant frequency shift for an added mass.

4.2 COMSOL Multiphysics Setup for QCM Mass Sensitivity Analysis

This section presents the configuration and methodologies utilized in COMSOL Multiphysics 6.0, which is reported to be applicable in evaluating the QCM's sensing performance [52], [119], [120]. Within this chapter, FEA is employed to study the impact of utilizing energy trapping regions for mass loading area on the mass sensitivity of QCMs, concurrently exploring device performance across various electrode topologies.

The QCM geometry is constructed, and its resonant frequency analyzed using COMSOL Multiphysics simulation software, version 6.0.

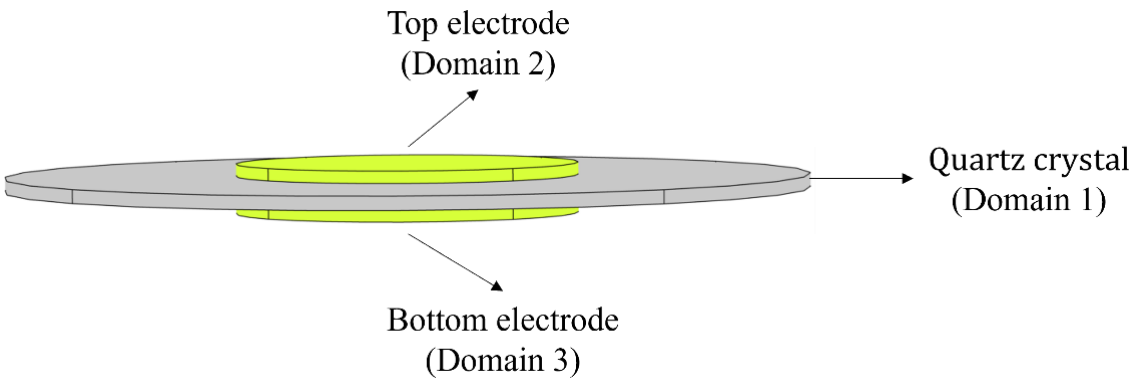

Figure 15. Schematic depiction of QCM geometry in COMSOL Multiphysics (Not Drawn to Scale).

The geometry of the QCM is built within COMSOL Multiphysics utilizing the three-dimensional spatial dimension. Figure 15 depicts the construction of a conventional QCM geometry within the COMSOL software. This configuration encompasses domains within the software framework, representing the quartz crystal (Domain 1), top electrode (Domain 2), and bottom electrode (Domain 3). The material properties essential for the COMSOL simulations are detailed in Table 3.

Table 3: Material properties used in COMSOL simulations. [52]

Material	**Domain**	**Density**	**Shear (μ) / Young's (Y) Modulus**	**Permittivity**
Quartz	1	2,468 g/cm3	μ = 2.947 x 1011 g/cm/s2	1
Gold	2,3	1,93,000 g/cm3	Y = 70 GPa	1

A crucial aspect of the setup is the exploration of Mesh Dependency, targeting enhanced meshing sequences to strike a balance between computational efficiency and result accuracy. By varying meshing sequences including Normal, Fine, Finer, Extra Fine, and User Controller (swept mesh), presented in Figure 16.

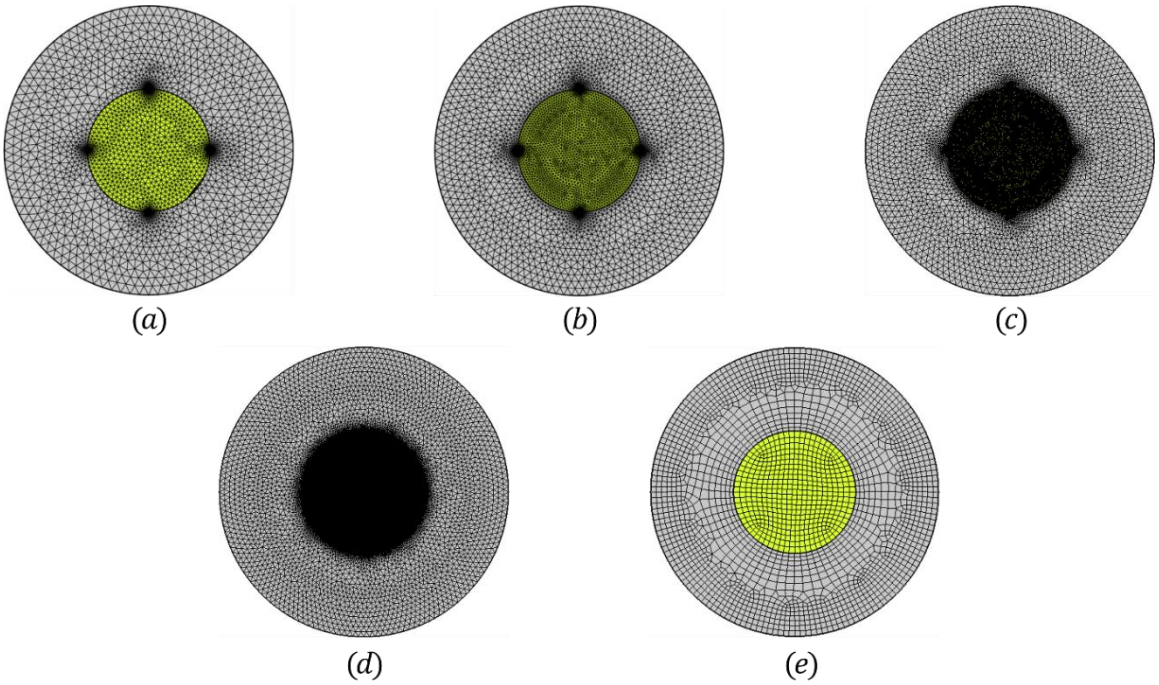

Figure 16. Schematic depiction representing diverse meshing sequence of QCM namely (a) Normal mesh (b) Fine Mesh (c) Finer Mesh (d) Extra Fine Mesh (e) User Controlled (swept mesh).

For this study, a 5 MHz conventional QCM is established following the specifications outlined in prior research investigations [52], [59], [121], utilizing the design parameters detailed in Table 4. These specified design parameters establish a foundational model for the 5 MHz circular electrode QCMs employed in this investigation. Importantly, the research conducted herein holds broader applicability for other conventional QCM devices, as the models rely on identical material properties and governing equations [52].

Table 4: Conventional design parameters of a 5 MHz QCM used for mesh dependency study.

Parameter	**Value**
Quartz radius	10 [mm]
Quartz thickness	333 [μm]
Electrode radius	4.25 [mm]
Electrode thickness	300 [nm]
Voltage	10 [V]

As depicted in Figure 17, the employed swept mesh technique effectively achieved the resonant frequency of the 5 MHz QCM employing a reduced number of meshing elements. This resulted in a notable reduction in computational resource consumption and subsequent simulation time. The utilization of the user-controlled swept mesh methodology proves its applicability for the simulation of 5 MHz QCM devices within this thesis, primarily due to the uniformity in material properties and governing equations employed across the models.

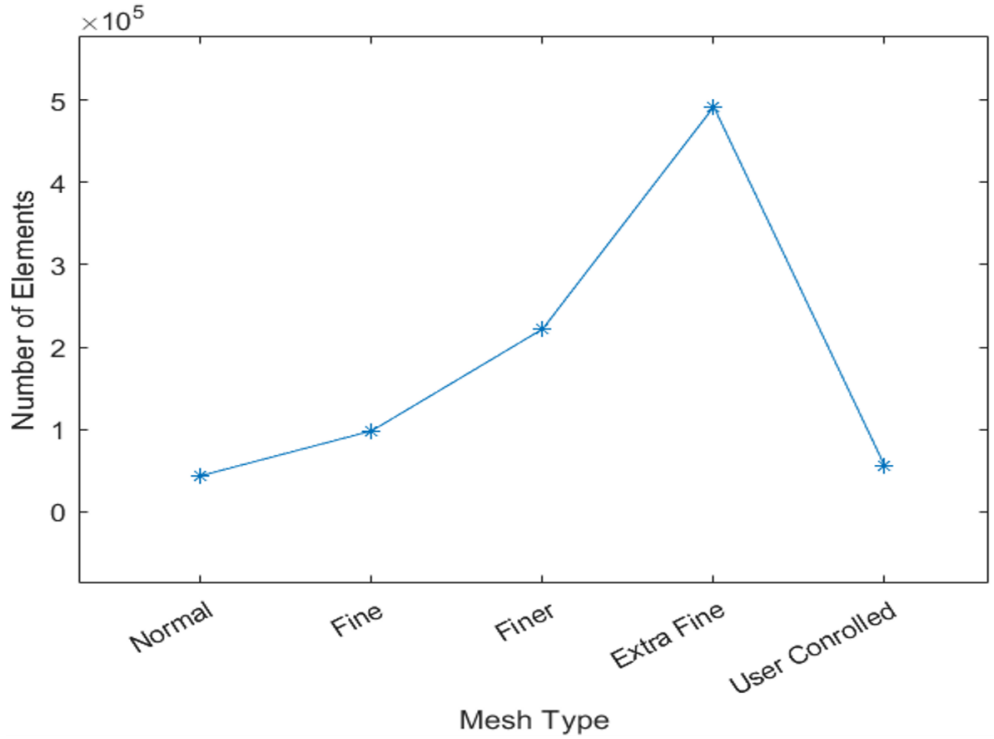

(*a*)

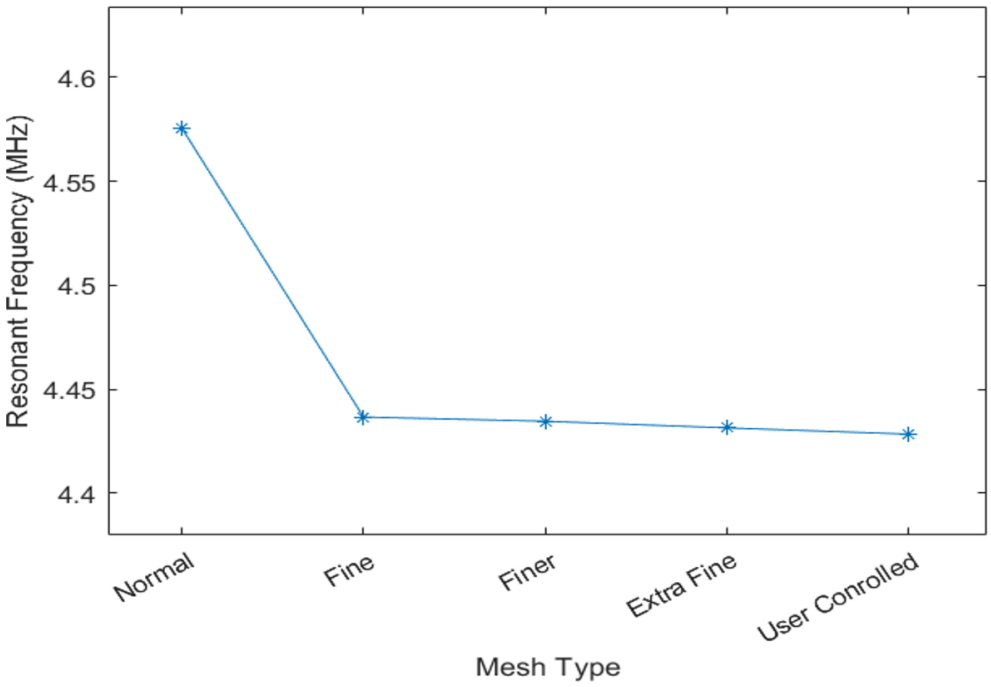

(*b*)

Figure 17. 2D plots of the COMSOL mesh dependency analysis results presenting (a) number of meshing elements (b) the resonant frequency obtained for different mesh type.

Furthermore, the establishment of boundary conditions within COMSOL Multiphysics is crucial. The Physics node plays a essential role in defining domain conditions, simulating the operational dynamics of the QCM. The Piezoelectricity Multiphysics setup harnesses the stress-charge relation to generate the inverse-piezoelectric effect within the QCM [52].

$$T = c_E S - e^T E \tag{18}$$

$$D = eS + \varepsilon_0 \varepsilon_{rS} E \tag{19}$$

where T represents stress, D stands for electric displacement, S signifies strain, and E denotes the electric field. The material parameters e, c_E, ε_0, and ε_{rS} correspond to coupling properties, material stiffness, relative permittivity, and permittivity of free space, respectively. Additionally, the model employs Electrostatics and Solid Mechanics nodes to induce the electric field and mechanical deformation.

In addition, the electrostatics node is instrumental in applying electrical voltage to the QCM electrodes. This configuration, with the terminal condition sub-node applying voltage to the top electrode (domain 2) while grounding the bottom electrode (domain 3), simulates realistic operational scenarios [52], [122].

Furthermore, solid mechanics conditions within COMSOL Multiphysics enable the imposition of mass loading onto the QCM using the added mass condition. Here, the top boundary of the top electrode (domain 2) acts as the designated mass loading area [52], [123]. The condition provides an option, mass per unit area, facilitating the consideration of added mass relative to the sensing electrode's area.

$$F_A = -\rho_A\left(\omega^2 u + a_f\right) \tag{20}$$

where the mass, considered as a force F_A acting on the chosen surface, incorporates the mass per unit denoted by ρ_A. the angular frequency denoted as ω, and u representing displacement. Additionally, a_f signifies the force contribution due to external factors, such as gravitational acceleration.

4.3 Effect of Mass Loading Area on QCM Mass Sensitivity

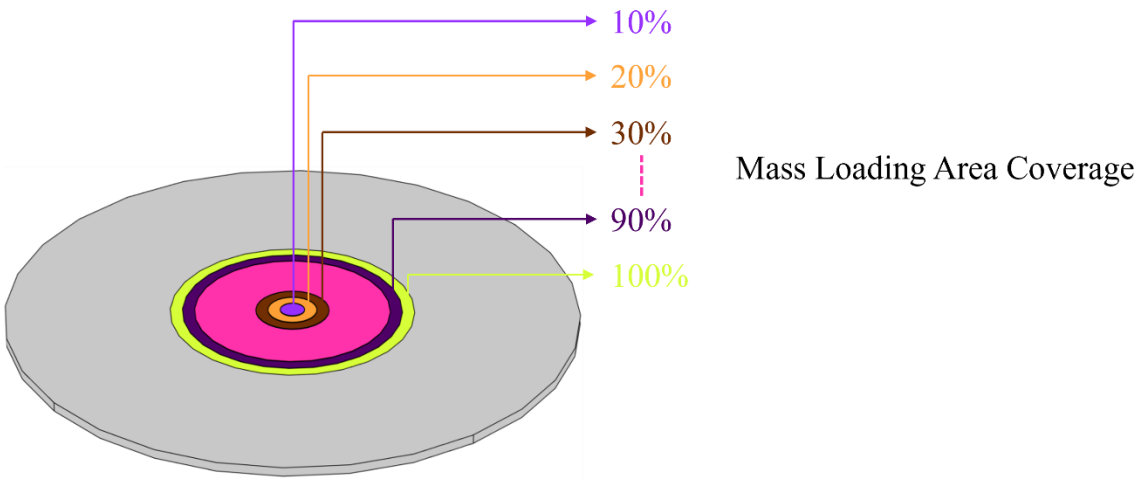

Figure 18. Schematic depiction of a QCM with a mass loading area coverage from 10 % to 100 % (highlighted & not to scale) on the top electrode.

The observed change in the QCM's resonant frequency owing to the mass loading effect identifies a specific area, known as the mass loading area, depicted in Figure 18. According to Sauerbrey's equation [107], the frequency shift of the QCM exhibits an inverse relationship with its mass loading area. However, a larger mass loading area facilitates increased mass loading, consequently enhancing the QCM's frequency shift. This prompts a necessity to investigate the impact of the QCM's mass loading area on its sensing capabilities. Hence, an analysis is conducted specifically targeting the effect of the mass loading area on a fundamental 5 MHz QCM featuring a conventional circular electrode configuration. Key design parameters, such as quartz radius, quartz thickness,

electrode radius, and electrode thickness, are held constant at specified values outlined in Table 5.

Table 5: Conventional design parameters of a 5 MHz QCM with changing mass loading area coverage from 10% to 100%.

Parameter	**Value**
Quartz radius	10 [mm]
Quartz thickness	333 [μm]
Electrode radius	4.25 [mm]
Electrode thickness	300 [nm]
Voltage	10 [V]

Within this analysis, the mass loading area is conceptualized as a boundary layer of negligible thickness atop the top electrode, possessing an adsorption capacity of 20 μg/mm² [52]. The investigation involves varying the mass loading area across dimensions ranging from 0.425 mm to 4.25 mm, corresponding to 10% to 100% coverage of the entire top electrode.

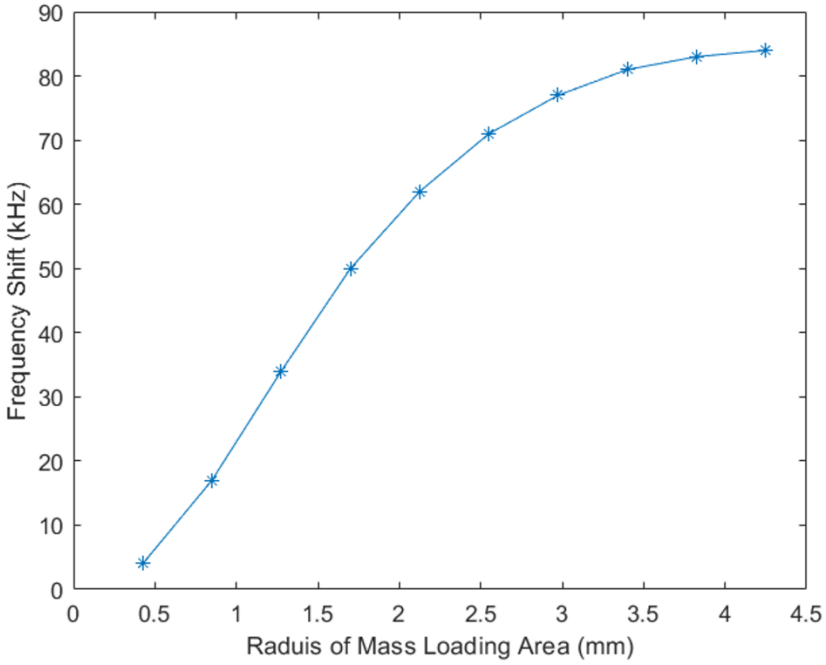

(*a*)

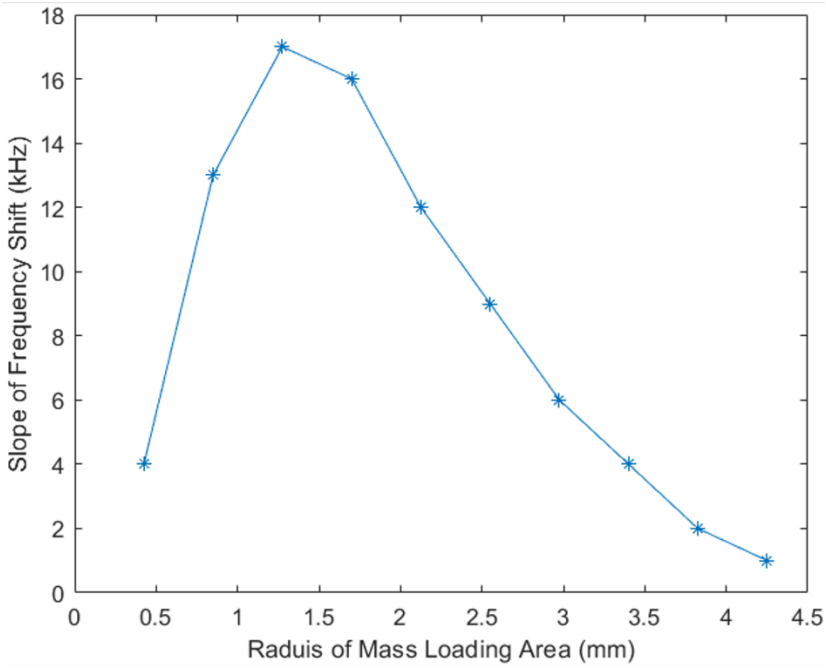

(*b*)

Figure 19. 2D plots of from COMSOL simulation results illustrating (a) the frequency shift (kHz) obtained for different values of radius of mass loading area (mm) for an added mass per unit area of 20 μg/mm² (b) the individual frequency shift values for changing radius of mass loading area as the slope of frequency shift vs radius of mass loading area for radii values.

The graphical representation in Figure 19 (a) demonstrates a gradual increase in frequency shift concurrent with an increase in the mass loading area. Furthermore, Figure 19 (b) delineates individual frequency shift values against the varied mass loading areas, reaching a peak at 1.275 mm, followed by a gradual decline. This observed spike in resonant frequency shift signifies the presence of localized energy trapping, designating the corresponding region as an advantageous area of opportunity. Leveraging this region for mass loading would yield a higher resonant frequency shift with reduced mass loading area, thereby enhancing mass sensitivity. The analysis outcomes indicate that strategic electrode placement on the QCM can significantly enhance mass sensitivity while employing a diminished mass loading area compared to conventional setups.

Expanding upon the foundational analysis, this study delves deeper into exploring the impact of mass loading area on the mass sensitivity of a 5 MHz QCM, considering various electrode radii values of 1 mm, 1.5 mm, 2.5 mm, 4.25 mm, and 5.5 mm, depicted in Figure 20.

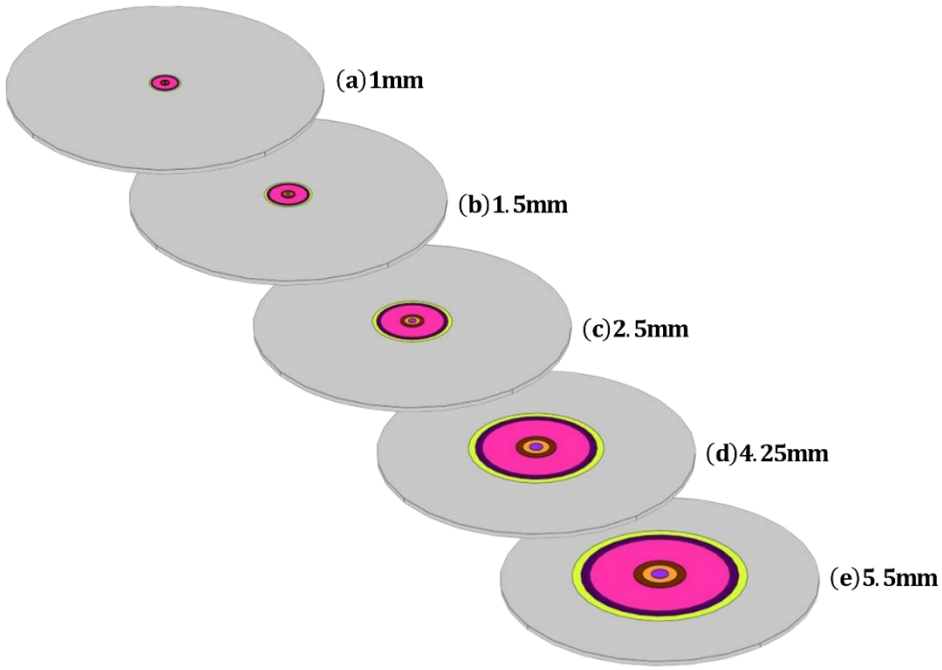

Figure 20. Mass loading area coverage is varied for QCM devices with electrode radii values of (a) 1 mm, (b) 1.5 mm, (c) 2.5 mm, (d) 4.25 mm, and (e) 5.5 mm to determine the frequency shift for an added mass per unit area of 20 μg/mm2.

The objective is to pinpoint the areas on the QCM electrode that yield the maximum resonant frequency shift for these distinct electrode radii values. The design parameters, such as quartz radius, quartz thickness, electrode radius, and electrode thickness, are held constant at specified values outlined in Table 6.

Table 6: Conventional design parameters of a 5 MHz QCM with changing mass loading area coverage from 10% to 100%.

Parameter	**Value**
Quartz radius	10 [mm]
Quartz thickness	333 [μm]
Electrode thickness	300 [nm]
Voltage	10 [V]

In this investigation, the mass loading area is conceptualized as a boundary layer of negligible thickness atop the top electrode, featuring an adsorption capability of 20 $\mu g/mm^2$. The analysis involves varying the mass loading area across dimensions corresponding to 10% to 100% coverage of the entire top electrode.

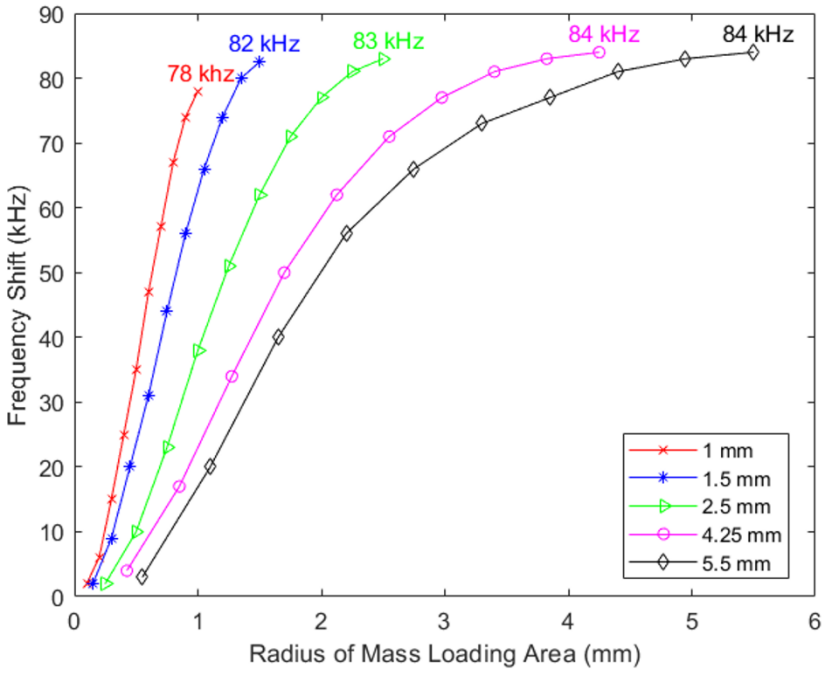

(*a*)

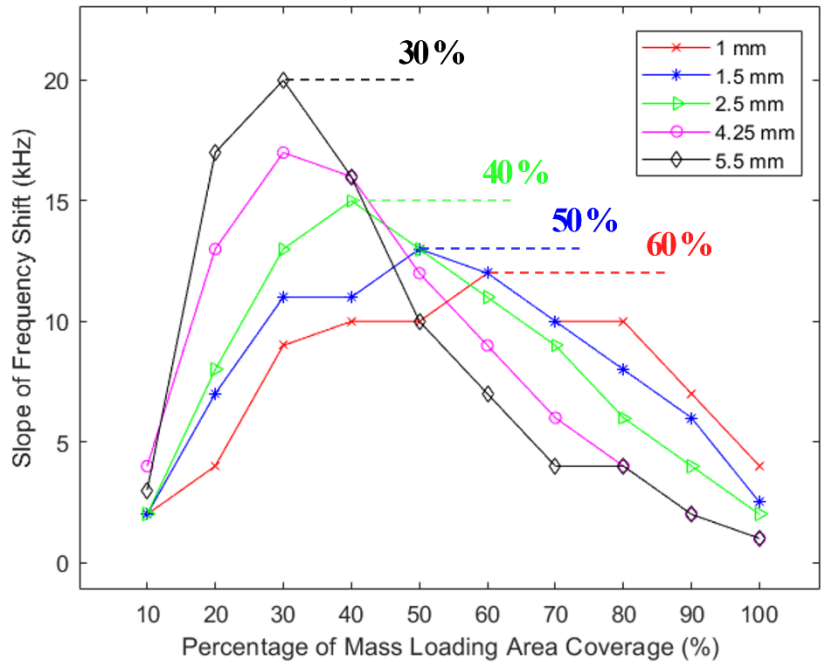

(*b*)

Figure 21. 2D plots of the results from COMSOL simulation illustrating (a) the frequency shift (kHz) obtained for different values of radius of mass loading area (mm) for an added mass per unit area of 20 μg/mm² (b) the individual frequency shift values for changing radius of mass loading area as the slope of frequency shift vs radius of mass loading area for radii values.

Figure 21 (a) represents a plot of the resonant frequency shift across the radius of the mass loading area for different electrode radii values. The results reveal a slightly greater frequency shift by less than 5% for devices with larger electrode radii when fully loaded. This can be attributed to larger electrodes accommodating a greater mass loading area, thereby generating a higher resonant frequency shift. However, exploring individual frequency shift values while altering the coverage of mass loading area on the QCM electrode, illustrated in Figure 21 (b), reveals specific points where the frequency shift is notably higher. These distinct areas of opportunity, providing maximum frequency shift, vary concerning different electrode radii values. Notably, for larger radii devices (5.5 mm and 4.25 mm), the point of maximum frequency shift tends to be nearer to the center, specifically at 30% coverage. Conversely, reducing the electrode radii shifts the maximum frequency shift point towards higher electrode coverage 40%, 50%, and 60% for electrode radii values of 2.5 mm, 1.5 mm, and 1 mm, respectively.

This analysis highlights that smaller electrode radii necessitate a greater mass loading area coverage to achieve the maximum frequency shift, thereby distributing the area of opportunity more uniformly across the QCM electrode. While larger electrode radii devices achieve slightly higher total frequency shifts, their maximum frequency shift point occurs at a lower mass loading area coverage, thereby limiting the area of opportunity.

4.4 Newly Developed Electrode Configurations Based on Distribution of Mass Loading Area for Improving Mass Sensitivity (DAIS)

Building upon previous studies, the strategic adoption of smaller electrodes, as opposed to a single larger conventional electrode, presents a promising avenue to enhance

the mass sensitivity of the device by effectively utilizing the areas of opportunity on the QCM surface. This approach aims to capitalize on these specific areas while concurrently ensuring heightened mass sensitivity. Leveraging this concept, novel electrode configurations for the QCM are conceptualized, focusing on redistributing the mass loading area to enhance mass sensitivity.

These newly devised electrode configurations are analyzed and compared against the established conventional electrode setup of the QCM. One such configuration, termed the DAIS electrode configuration, is developed to exploit the energy trapping effect by strategically distributing the mass loading area. This analysis specifically entails evaluating a 5 MHz QCM featuring the novel DAIS electrode configuration to ascertain the resonant frequency shift corresponding to an added mass.

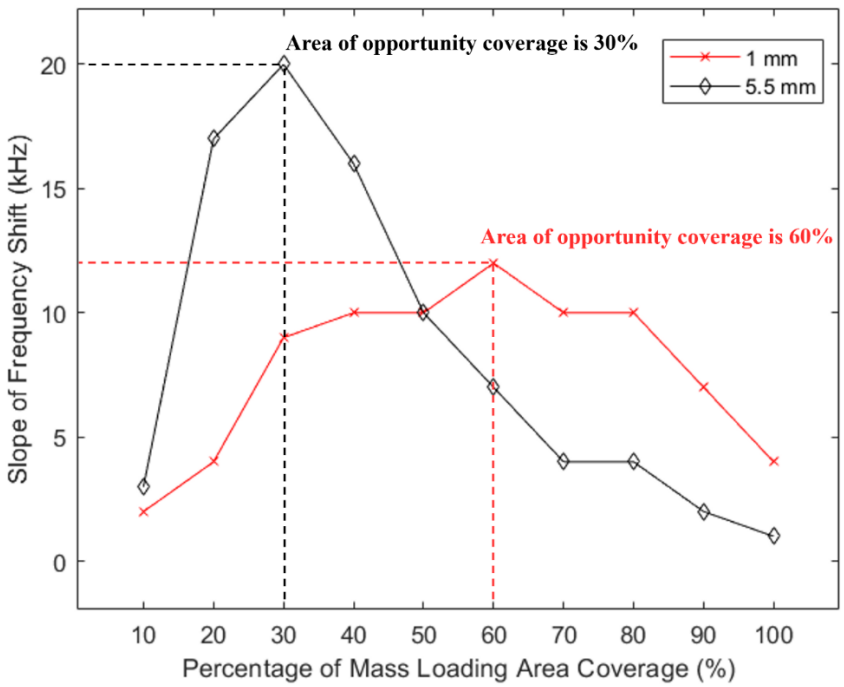

Figure 22. 2D plot of the results form COMSOL simulation illustrating the individual frequency shift values against the percentage of mass loading area as the slope of frequency shift vs percentage of mass loading area for electrode radii values 5.5 mm and 1 mm.

The DAIS design, predicated on the collective use of electrodes with reduced mass loading areas to enhance QCM sensitivity, maintains the outer electrode radius identical to that of the conventional electrode configuration. Figure 22 elucidates that, for an electrode radius of 5.5 mm, the optimal frequency shift point is attained at 30% mass loading area coverage, approximating an area of 28 mm². Consequently, the electrode radius is fixed at 2.96 mm. Similarly, for an electrode radius of 1 mm, the peak frequency shift is closer to 60% mass loading area coverage, leading to an electrode radius consideration of 0.76 mm to maximize coverage.

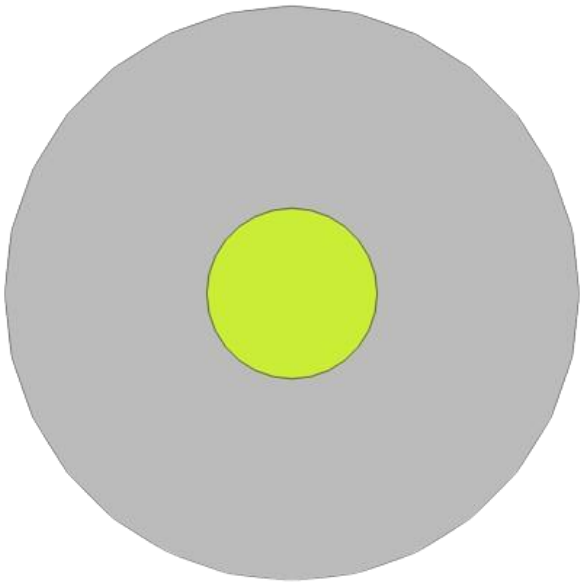

Figure 23. Schematic depiction of a 5 MHz QCM with conventional circular electrode configuration with a novel radius 2.96 mm, equivalent to inde.

Derived from empirical observations, a 5 MHz QCM, termed the Novelcircular-QCM, is constructed with a conventional circular electrode possessing a novel radius of 2.96 mm (equivalent to 30% mass loading area coverage for a 5.5 mm electrode radii), as depicted in Figure 23. This device is employed to determine the resonant frequency and frequency shift for an added mass per unit area of 20 μg/mm², thereby assessing its mass

sensitivity. Table 7 outlines the parameters utilized for designing the 5 MHz QCM in this analysis.

Table 7: Design parameters of Novelcircular-QCM.

Parameter	**Value**
Quartz radius	10 [mm]
Quartz thickness	333 [μm]
Electrode radius	2.96 [mm]
Electrode thickness	300 [nm]
Voltage	10 [V]

Employing COMSOL Multiphysics software, the device, with a total mass loading area of 27.52 mm², achieves a frequency shift of 83.5 kHz. Calculations indicate a mass sensitivity of 151.71 Hz/μg·mm², with a sensitivity distribution of 72.72%, evaluated using the area under curve (AUC) relative to the Sauerbrey assumption's best-case scenario.

The DAIS electrode configuration, termed DAIS(G1)-QCM (Generation 1), introduces a design featuring multiple smaller circular electrodes replacing a single larger electrode, aiming to maximize energy trapping. This configuration comprises seven circular electrodes positioned at the quartz's center, encircled by eight additional circular electrodes, each with a radius of 0.76 mm, corresponding to 60% mass loading area coverage for a 1 mm electrode radius, as illustrated in Figure 24.

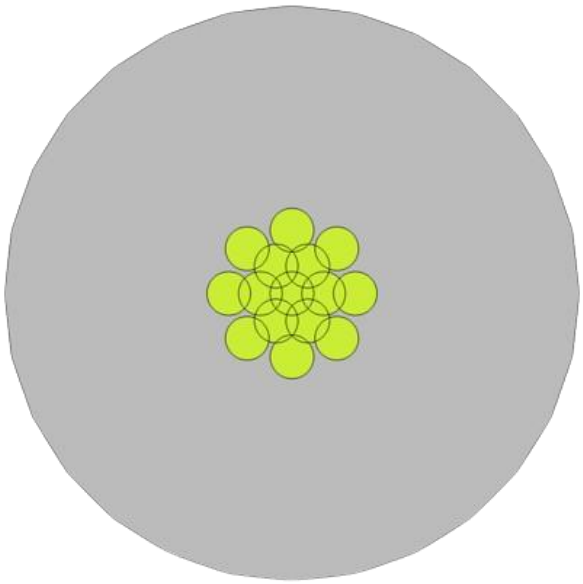

Figure 24. Schematic depiction of a 5 MHz QCM with novel DAIS electrode configuration of outer radius of 2.96 mm comprising of several smaller circular electrodes of radius 0.76 mm.

Employing this DAIS(G1)-QCM configuration, the device's resonant frequency and frequency shift concerning an added mass per unit area of 20 μg/mm² are evaluated to assess its mass sensitivity. Utilizing COMSOL simulations, the device exhibits a frequency shift of 82.5 kHz, featuring a total mass loading area of 22.21 mm². The derived mass sensitivity amounts to 185.73 Hz/μg·mm², accompanied by a sensitivity distribution of 69.54%.

A novel iteration of the DAIS electrode configuration, termed DAIS(G2)-QCM, is introduced to explore the impact of employing a single electrode in lieu of multiple smaller electrodes in the central region. In this second-generation DAIS model, the array of seven circular electrodes with a radius of 0.76 mm, as featured in the central area of the DAIS(G1)-QCM, is substituted by a single circular electrode with a radius of 1.75 mm, as depicted in Figure 25. Notably, the outer electrode radius remains unchanged at 2.96 mm.

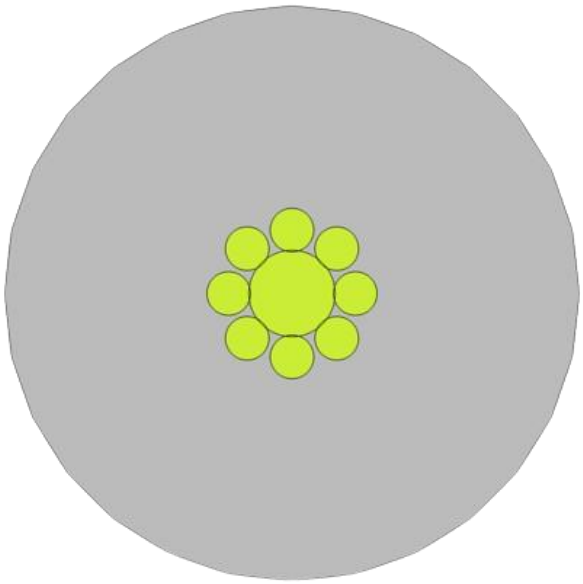

Figure 25. Schematic depiction of a 5 MHz QCM with novel DAIS electrode configuration (second generation) of outer radius of 2.96 mm comprising of a central circular electrode radius of 1.75 mm surrounded by smaller circular electrodes of radius 0.76 mm.

Through an assessment of the resonant frequency and frequency shift regarding an added mass per unit area of 20 μg/mm², the mass sensitivity of the DAIS(G2)-QCM is evaluated. The simulation outcomes indicate a frequency shift of 83.5 kHz, with a total mass loading area measuring 22.31 mm². This configuration achieves a calculated mass sensitivity of 187.14 Hz/μg·mm², accompanied by a sensitivity distribution of 64.93%.

Introducing the third iteration of the DAIS electrode configuration, termed DAIS(G3)-QCM, aims to scrutinize the impact of smaller electrodes on the device's mass sensitivity. In this third-generation model, the array of circular electrodes featuring a radius of 0.76 mm, as observed in the DAIS(G1)-QCM, is supplanted by smaller electrodes measuring 0.62 mm, as depicted in Figure 26. Notably, the outer electrode radius remains consistent at 2.96 mm.

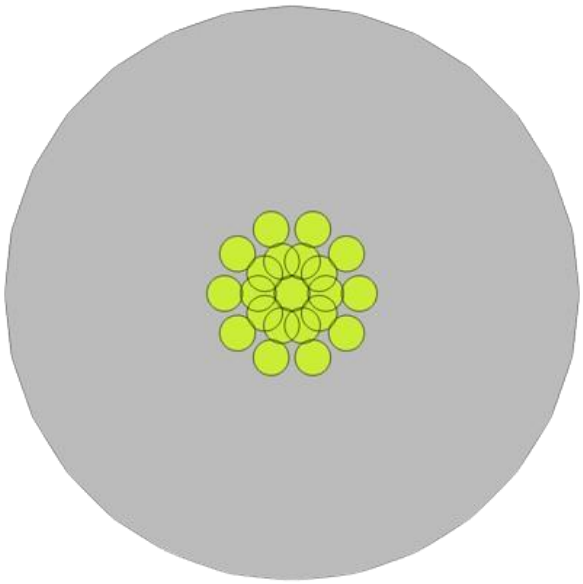

Figure 26. Schematic depiction of a 5 MHz QCM with novel DAIS electrode configuration (third generation) of outer radius of 2.96 mm comprising of several smaller circular electrodes of radius 0.62 mm.

Evaluation of the resonant frequency and frequency shift concerning an added mass per unit area of 20 μg/mm² provides insights into the mass sensitivity of the DAIS(G3)-QCM configuration. The simulation outcomes demonstrate a frequency shift of 83.81 kHz, with the total mass loading area measuring 21.33 mm². This configuration achieves a calculated mass sensitivity of 196.46 Hz/μg·mm², accompanied by a sensitivity distribution of 68.87%.

4.5 Conclusion

The investigation into QCM devices has unveiled advancements in enhancing mass sensitivity through utilizing the areas of opportunities for mass loading area. The Findings highlighted the pivotal role of mass loading area in influencing the resonant frequency shifts and, consequently, the mass sensitivity of QCM devices.

The exploration encompassed four distinct designs: the conventional QCM, Novelcircular-QCM, and three generations of the DAIS electrode configurations

(DAIS(G1)-QCM, DAIS(G2)-QCM, and DAIS(G3)-QCM). These designs, built upon alterations in electrode sizes and configurations, were meticulously evaluated for their resonant frequency shifts and mass sensitivity performances.

Table 8: Comparison of mass sensitivity and its distribution for a 5 MHz QCM with circular and DIAS electrode configurations.

	Conventional-QCM	**Novelcircular-QCM**	**DAIS(G1)-QCM**	**DAIS(G2)-QCM**	**DAIS(G3)-QCM**
Mass Loading Area (mm^2)	56.75	27.52	22.21	22.31	21.33
Frequency Shift (kHz)	84	83.5	82.5	83.5	83.81
Mass Sensitivity ($Hz/\mu g\ mm^2$)	74.01	151.71	185.73	187.14	196.46
Mass Sensitivity Distribution (%)	42.05	71.72	69.54	64.93	68.87

The comparison, listed in Table 8, for the five QCM devices reveals insights into their respective performances. The Conventional-QCM presents a baseline reference, exhibiting a larger mass loading area but relatively lower frequency shift and mass sensitivity. The Novelcircular-QCM demonstrates notable improvements in mass sensitivity and distribution by maximizing the energy trapping effect for the mass loading area. The DAIS configurations show consistent or increased frequency shifts compared to the Novelcircular-QCM. DAIS(G1)-QCM showcased advancements by replacing multiple smaller electrodes with a larger central electrode, exhibiting enhanced mass

sensitivity. However, DAIS(G2)-QCM, with a singular larger central electrode, maintained a similar frequency shift but showcased a slight reduction in mass sensitivity distribution. Remarkably, DAIS(G3)-QCM, employing smaller electrodes, achieved the highest mass sensitivity and distribution among all designs, showcasing the efficacy of smaller electrodes in maximizing sensitivity despite a slightly reduced overall mass loading area.

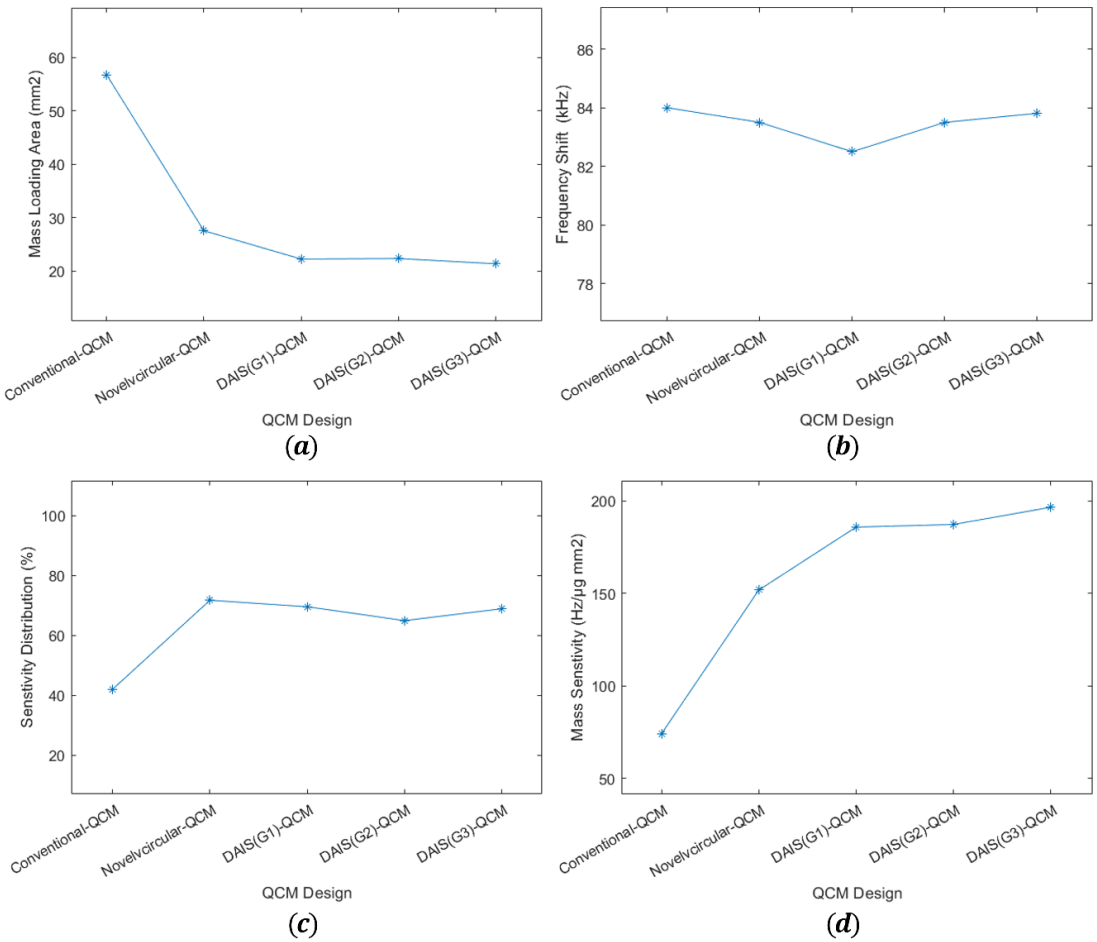

Figure 27. 2D plots of the results from COMSOL simulation illustrating (a) the mass loading area (mm²) (b) the frequency shift (kHz) obtained for an added mass per unit area of 20 µg/mm² (c) the mass sensitivity distribution values (d) the mass sensitivity values (Hz/µg mm²).

CHAPTER 5

Fabrication of Proposed QCM Sensor & Experimental Setup

5.1 Introduction

The experimental setup plays a crucial role in characterizing the proposed QCM sensors. The QCM sensors, derived from findings of the conducted FEA studies illustrated in the chapter 3, undergo fabrication process. These fabricated sensors are then exposed to target analytes within an environment regulated by a gas injection system, to evaluate their performance in response to target analytes exposure. The data acquisition system is used to acquire the sensors resonant frequencies, which vary in response to variations in the target analytes. The experimental system is carefully automated and synchronized to ensure the reliability and eliminate human error. In this chapter, the experimental setup is detailed, including the fabrication of proposed QCM sensors and the automated experimental system approach.

5.2 Fabrication of the Newly Developed QCM Sensors

The proposed designs for the QCM sensors are developed using SOLIDWORKS 2018 SP05 software, in the two-dimensional construction process. While the fabrication of the proposed QCM sensos, the electrical connection is taken into consideration. The conventional configuration and the wrap-around configuration, shown in Figure 28. diverge in their connection methodologies. While the conventional configuration allows both sides to function as sensing electrodes, it presents challenges in isolating the sensing electrode, thereby, it is not the preferred choice for liquid phase detection. Conversely, the wrap-around configuration allocates the top side for sensing and the bottom side for

electrical contact. This configuration readily enables the isolation of the contact electrode and stands as the favored configuration for liquid phase detection due to the ability of isolating the sensing electrode [124].

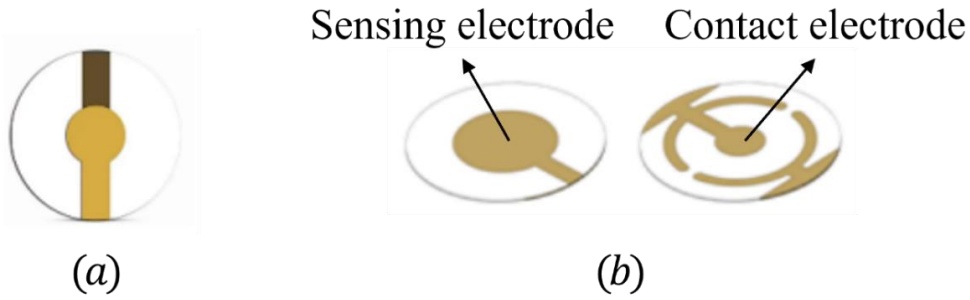

Figure 28. Schematic depiction of QCM sensor featuring (a) conventional configuration (b) wrap-around configuration.

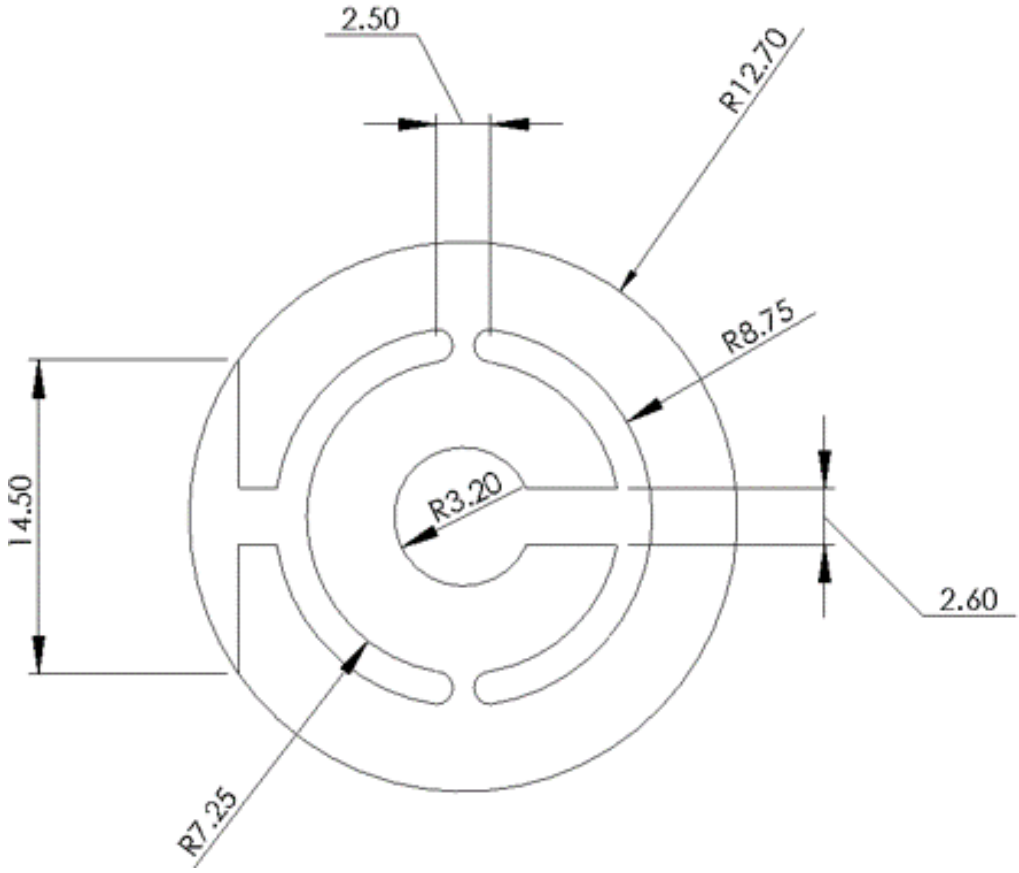

Figure 29. Schematic bottom-view of the proposed QCM design with detailed dimensions in mm.

For consistency and adherence to the chosen design, the side and bottom plans for all proposed QCMs remained identical, following the Wrap-around configuration as depicted in Figure 29. The SOLIDWORKS 2018 SP05 software facilitated the creation of five distinct topologies for the proposed QCM, illustrated in Figure 30.

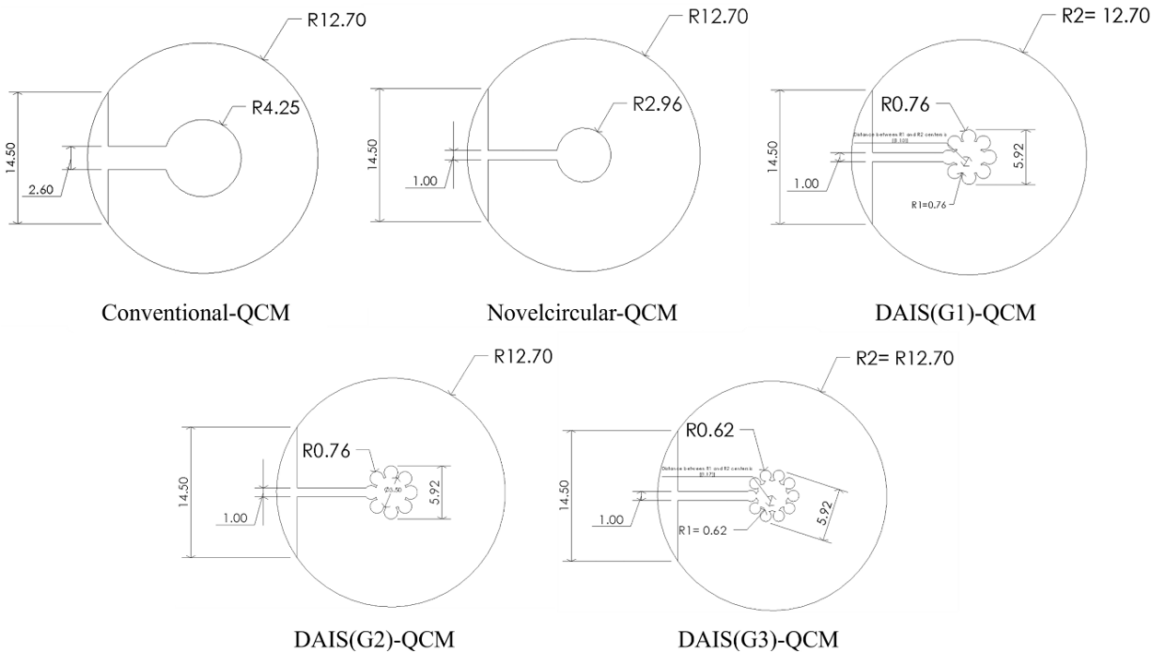

Figure 30. Schematic top-view of the proposed QCM designs with detailed dimensions in mm.

The fabrication process itself is executed by Angstrom Engineering Inc. , using final designs, introduced in section 4 of chapter 4. Derived from SOLIDWORKS 2018 SP05 software, the generated masks comprise front and rear invar sheets, each with a thickness of 0.15 mm, and an intermediate locating sheet precisely sized to the crystal's dimensions, 3 mm thickness and approximately 1-inch diameter, as illustrated in Figure 31. Laser cutting technology is used to create the invar masks and sheets, ensuring precision in their construction. The assembly was secured using aluminum retaining rings and M3 screws to apply clamping force, thereby holding the mask and crystals in place.

The retaining rings were also created via laser cutting to maintain consistency and precision throughout the assembly.

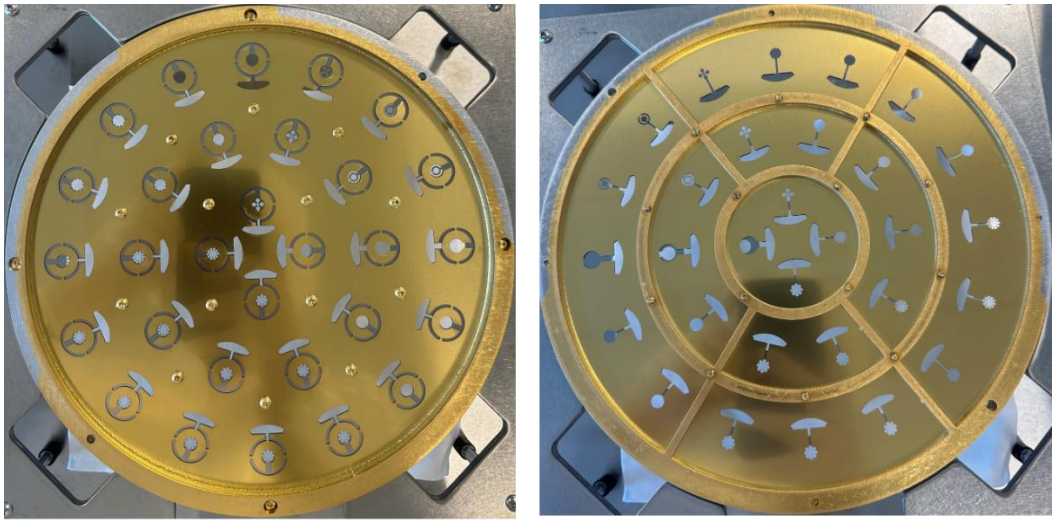

(*a*) (*b*)

Figure 31. Schematic (a) bottom-view (b) top-view of the generated mask used to fabricate the proposed QCM sensors.

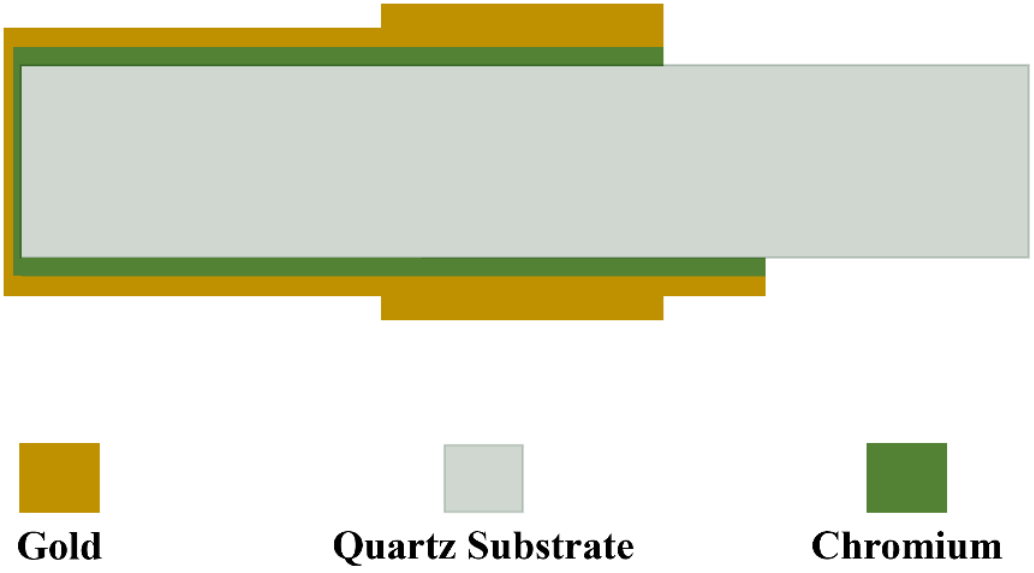

Figure 32. Schematic depiction of designed QCM device illustrating the layers and material used.

The fundamental geometry of the QCM involves a quartz crystal positioned between two electrode layers via an adhesion layer, as illustrated in Figure 32. The fabrication process adheres to a structured protocol to ensure the precise fabrication of the QCM. The utilization of 5 MHz 1" OD Quartz crystals maintained at a temperature of 25°C, is used as sensor substrate. The initial chamber pressure is set at 1E-06 Torr, and the samples undergo a thorough cleaning process involving Argon plasma for a duration of 5 minutes. Subsequently, an adhesion layer of 50 Å Chromium is deposited at a rate of 0.5 Å/s using eBeam evaporation. Following this, a gold layer of 1500 Å is deposited at a rate of 2 Å/s, again employing eBeam evaporation techniques. Figure 33 presents the fabricated QCM sensor with both conventional and proposed topologies.

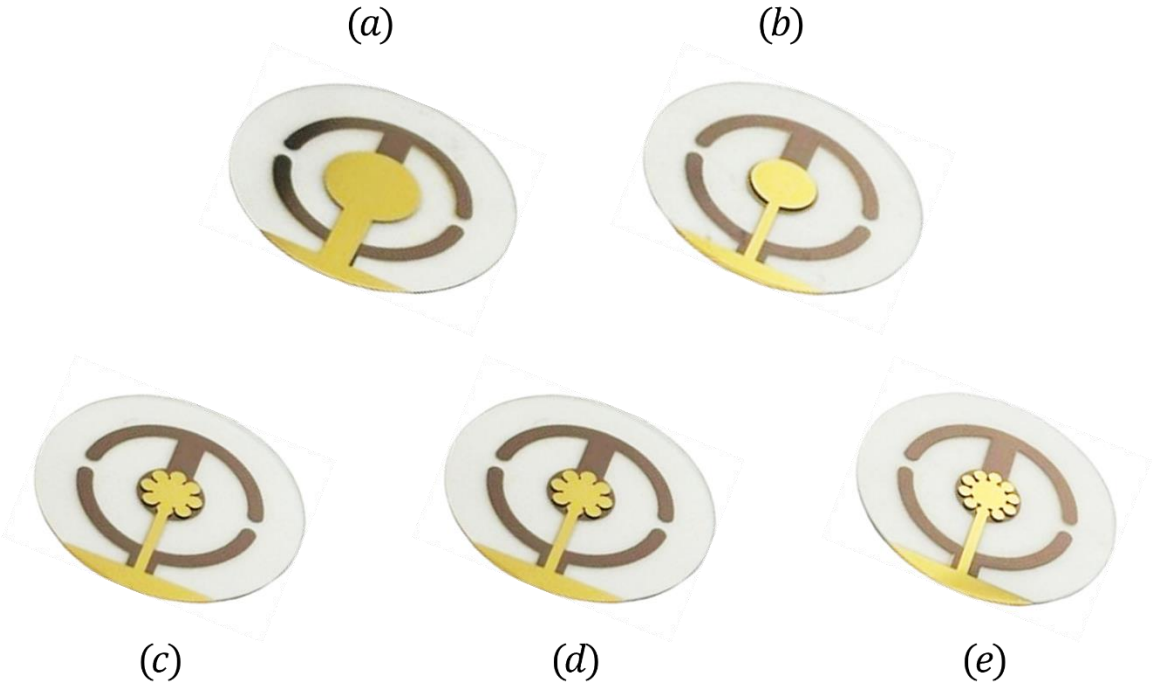

Figure 33. Depiction 5 MHz QCMs fabricated with varied topologies (a) Conventional-QCM (b) Novelcircular-QCM (c) DAIS(G1)-QCM (d) DAIS(G2)-QCM (e) DAIS(G3)-QCM.

5.3 Controlled Environmental Measurement Setup

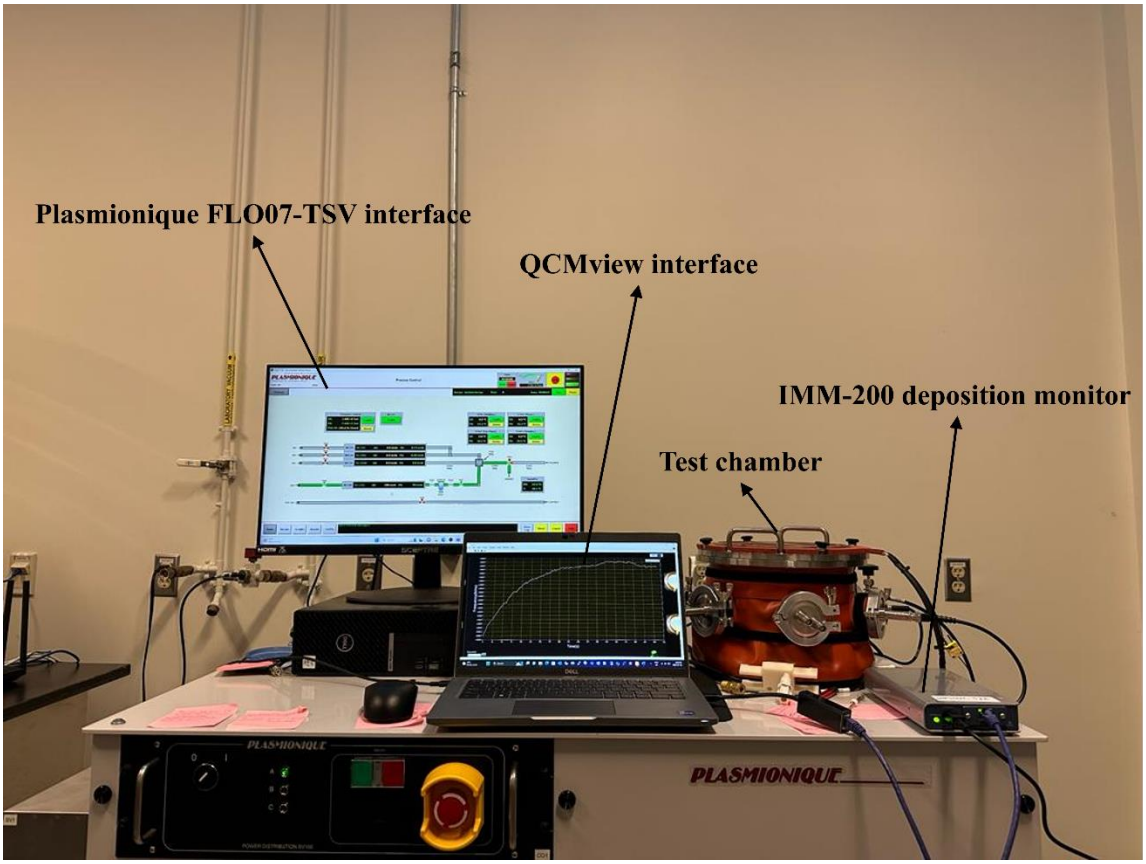

Figure 34. The experimental setup employed to establish the controlled environment necessary to evaluate the sensitivity of the fabricated QCM sensors.

The experimental setup, illustrated in Figure 34, employs the Plasmionique FLO07-TSV, a regulated gas injection system for controlled environmental measurements. The system is equipped with mass flow controllers with various flow ranges, and incorporates two bubblers for liquid vapor injection, as illustrated in Figure 35. The FLO07-TSV is integral for establishing the requisite controlled environment to evaluate the response of the QCM sensors. To regulate the concentration of the target analyte, an inert gas is employed to traverse a bubbler containing the desired analyte. This inert gas, termed the carrier gas, transports the target analyte molecules in vapor form to the test chamber. The dry ultra-high purity Nitrogen, , NI 5.0UH-T, is selected to

serve as carrier gas for its non-reactive properties with the utilized materials in the measurement system [125].

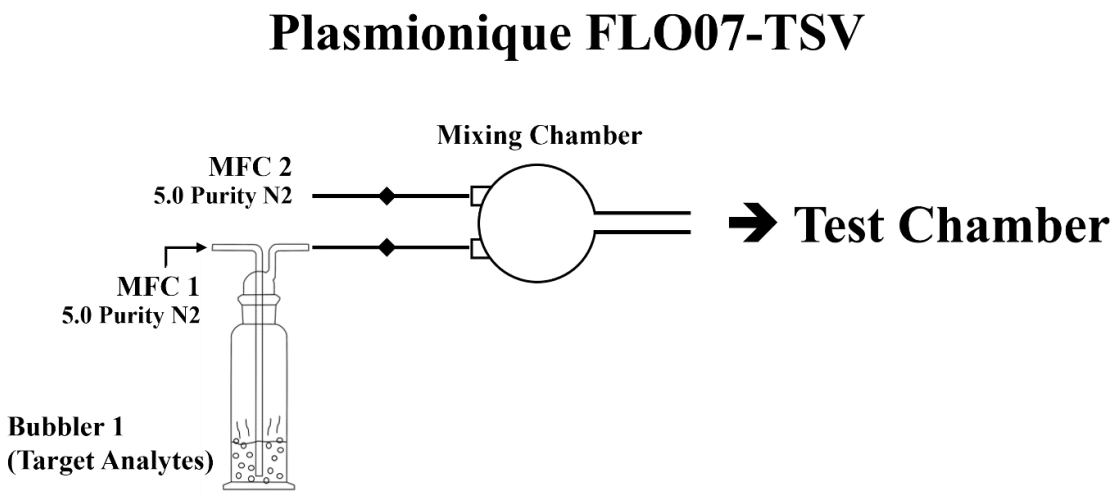

Figure 35. Schematic depiction of the Plasmionique FLO07-TSV, used to facilitate the controlled environment necessary to evaluate the sensitivity of the fabricated QCM sensors.

The test chamber, depicted in Figure 36, is designed to facilitate the appropriate exposure of target analytes to the fabricated QCM sensors in short duration, tested to be less that 15 mins, as presented in chapter 6. The chamber design is initially constructed using 2D assembly, which is later evolved into a 3D model for fabrication. The cylindrical design of the test chamber eliminates the presence of dead zones as well as any potential leakage, as the test chamber dimensions are aligned with the QCM holder to ensure seamless flow for the target analytes.

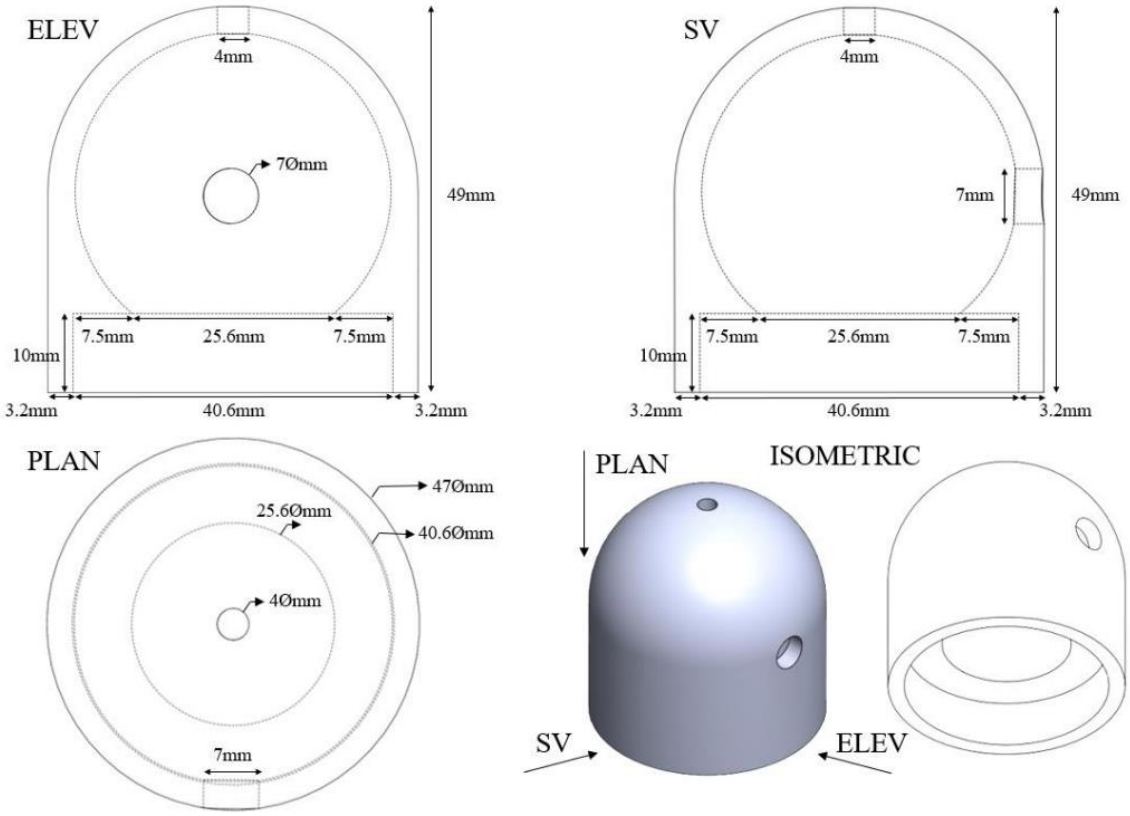

Figure 36. Schematic depiction of the designed test chamber , detailing elevation, side, and plan views.

The IMM-200, showed in Figure 37, is a deposition monitor pioneered by INFICON Inc., used to measure QCM sensor resonant frequency, which is the key parameter indicative of the sensor performance. Equipped with a single sensor input, the IMM-200 employs the ModeLock measurement technique. It operates within a frequency range of 6.0 MHz to 4.5 MHz. The device maintains reference frequency stability at ±2 ppm within a temperature range of 0–60°C and offers a frequency resolution of 0.0035 Hz per 100 ms [126]. For these specifications, the IMM-200 is chosen to be vital component in the experimental setup for assessing the proposed QCM sensors.

Figure 37. Depiction of the IMM-200 deposition monitor, used to acquire QCM sensor resonant frequency to evaluate the mass sensitivity of the fabricated QCM sensors.

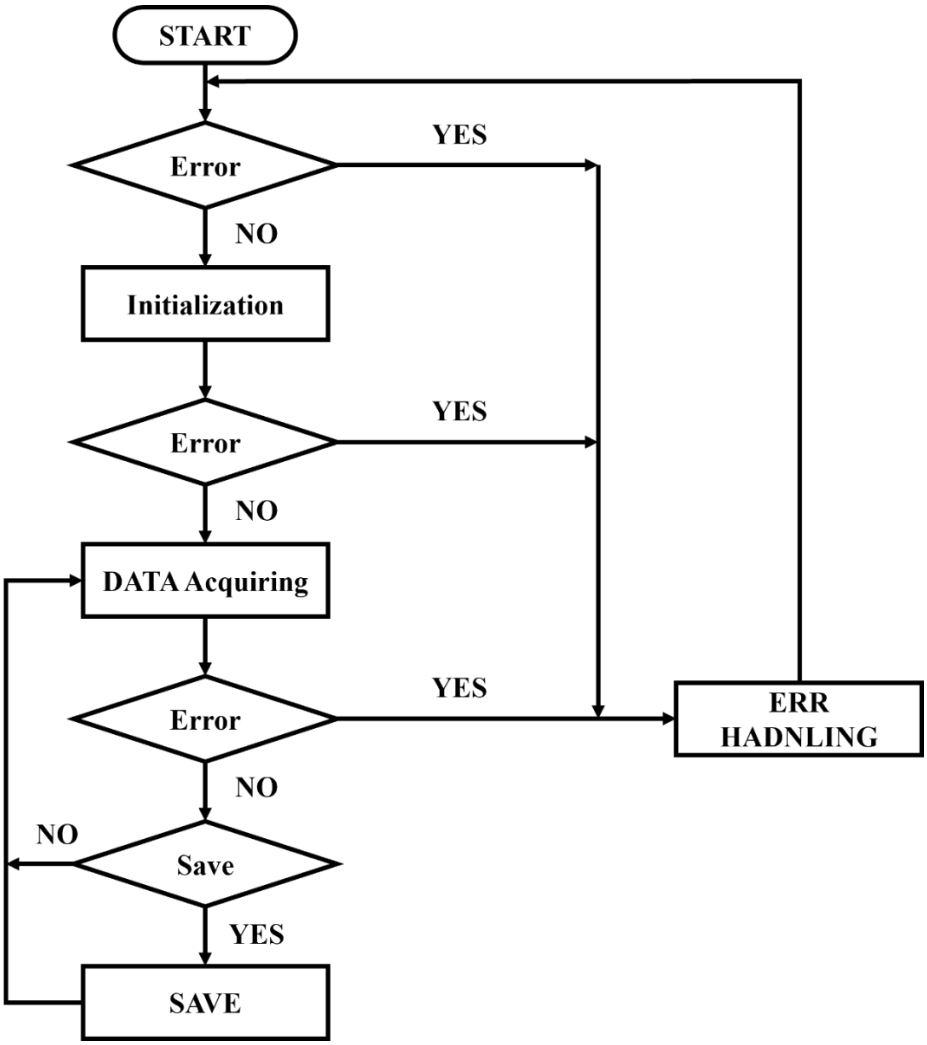

Figure 38. Flowchart of the state machine structure in the developed QCMView, illustrating the process from initialization to data storage.

The QCMView software, developed using NI LabVIEW, establishes a robust communication with the acquisition system. The IMM-200 employs the P3Plus communication protocol for packets transfer with computed CRC. A communication interface is developed via NI LabVIEW to receive, visualize, and store the data acquired from the IMM-200, adhering to a state machine structure. The state machine, depicted in Figure 38, encompasses four states: initialization, data acquisition, error handling, and saving. The initial state is designed to establish communication with Lantronix Xport, a server utilized by IMM-200 for data transmission. Subsequently, the data acquisition state assigns an RQA byte to 0x05 to request a read attribute, and two PID bytes are assigned to 0x02bf to identify the frequency parameter to be read. The third state is designed to handle errors by computing the CRC bytes received from the server. Finally, the acquired resonant frequency is stored in an Excel format.

The experimental setup is maintained to ensure consistent characterization of the fabricated proposed QCM sensors, thereby enhancing the reliability of the results obtained. The Plasmionique FLO07-TSV system is utilized to regulate the exposure of target analytes into the test chamber. The test chamber, designed specifically for this purpose, facilitates smooth flow of target analytes while minimizing the time required to achieve desired concentration levels. Both the Plasmionique FLO07-TSV system and the IMM-200 acquisition system are automated and synchronized, thereby omitting the potential for human error such as manual data entry mistakes and inconsistent operation procedures. This integrated approach provides a methodology that used for evaluating the proposed fabricated sensors performance.

CHAPTER 6

Characterization of Proposed QCM sensors

6.1 Introduction

To evaluate the sensing performance of the fabricated the QCM sensors, the experimental process is conducted in two phases differentiated by the presence of the polymer sensing layer. The first phase involves evaluating the sensors performance as standalone devices without applying a sensing layer to validate the outperformed performance of the proposed designs for the application that do not require presence of sensing layer such as monitoring the deposition of thin films [127]. The second phase of the experimental process is conducted after applying a polymer sensing layer to validate the use of the proposed novel QCM sensors for VOC detection application. The conventional QCM sensor servers as a baseline reference during the entire experimental process, as do the conducted simulations and analyses.

6.2 Experimental Process Phase I: QCM as a Standalone Device

The first phase of the experimental process involves testing the fabricated QCM sensor without the application of a sensing layer on top of the sensors. Applications such as deposition monitor in nanofabrication do not necessitate the presence of a sensing layer. In these applications, the QCM sensor operates as a standalone device where the changes in the sensor resonant frequency reflect the thickness of deposited layers [127]. Such applications require highly sensitive devices for precisely deposition as the deposition occurs in nanometer scale. For this purpose, the first phase is conducted to evaluate the performance of the fabricated sensors, which respond to identical target

analyte, select to be relative humidity (RH) which is reported to serve as a proof in concepts in related works [128].

To evaluate the sensors performance the experimental setup, introduced in chapter 5, is utilized to establish necessary controlled conditions. The AT-cut quartz crystal employed while fabricating the QCM sensors operates at a temperature of 25°C. Therefore, the temperature is maintained at 25±1°C to align with its operational temperature, which is reported to operate stably within a temperature range of 20-40°C [127]. The modulation of target analyte follows a designed pattern, with the QCM sensors are subjected to varying concentrations listed in Table 9, including the flow rates (%) and the corresponding values in parts per million (ppm). The concentration in ppm is evaluated using the following formula [129]:

$$C = \frac{J_{Bubbling}}{J_{Bubbling} + J_{BKG}} \times \frac{P_{gas}}{P_{atm}} \tag{21}$$

where $J_{Bubbling}$ and J_{BKG} are the flow rates of the bubbling and background (BGK) gases, respectively. P_{gas} represents the vapor pressure of the target gases, while P_{atm} is atmospheric pressure, which equals to 101.325 kpa (1 atm) [130].

Table 9: Regulated flow rates and adjusted RH concentrations injected into the test chamber.

RH flow rate (sccm)	BKG flow rate (sccm)	Concentration (ppm)
10	90	2300
20	80	4600
30	70	6900
40	60	9200
50	50	11500

The baseline measurements are firstly conducted by exposing the fabricated sensors with pure dry N_2 for 60 minutes to ensure a RH concentration of zero. these measurements serve as reference to monitor sensor performance through the observation of frequency shifts in sensors resonant frequency in response to regulated concentrations of target analytes. In addition to this, the baseline measurements, illustrated in Figure 39, provide preliminary insights. the proposed QCMs exhibit higher fundamental resonant frequency of over 7 kHz compared to conventional QCM. The fundamental resonant frequency influences the QCM performance according to Sauerbrey equation [107]:

$$\Delta f = -\frac{2f_0^2}{A\sqrt{\rho_q \mu_q}}\,\Delta m \tag{22}$$

where f_0 represents the fundamental resonant frequency, A is the active area of the quartz crystal situated between the electrodes, and Δm signifies the alteration in mass on the QCM surface due to analyte absorption. μ_q is the shear modulus of the quartz crystal, ρ_q is the quartz crystal density.

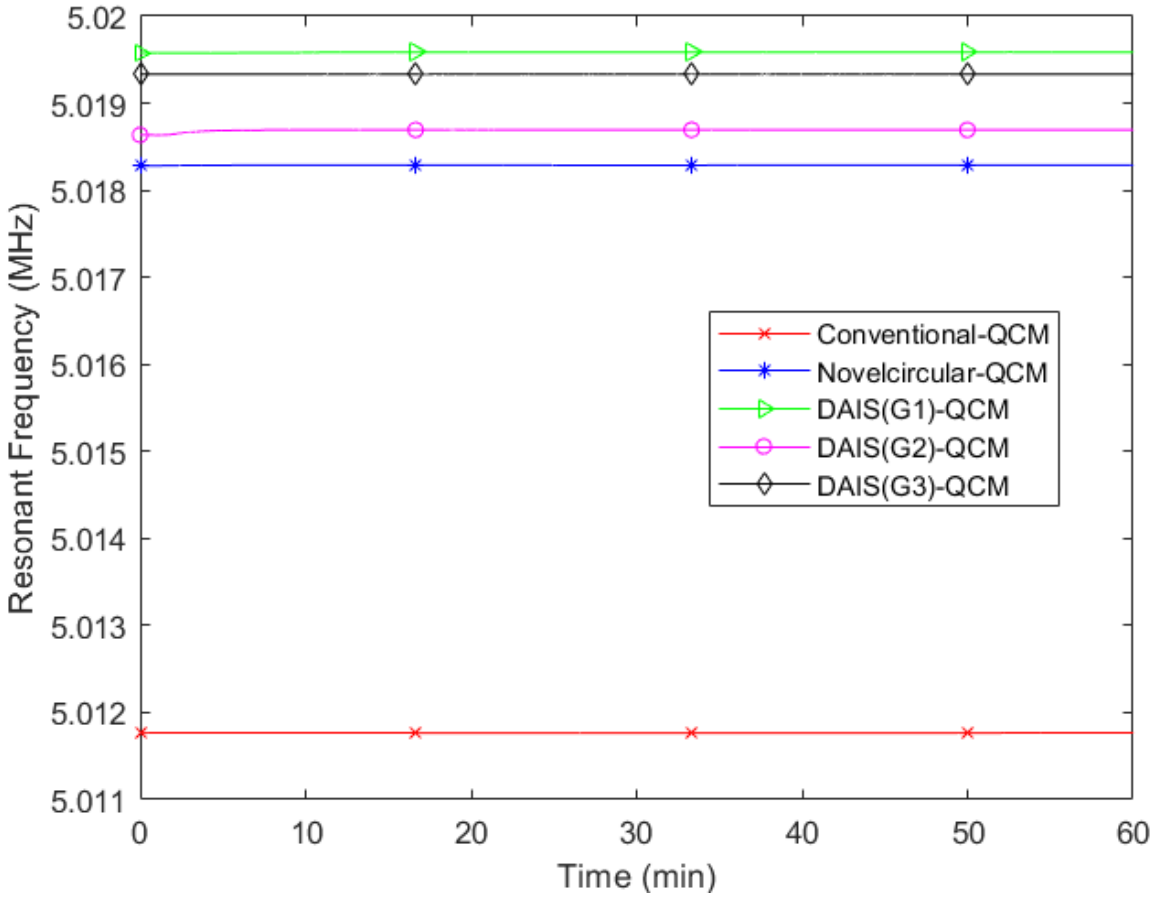

Figure 39. 2D plot of experimental results illustrating fundamental resonant frequency for QCM sensor, featuring both DAIS and conventional QCM designs.

The experimental pattern is designed to start with a gradual increase in RH concentration by 2300 ppm, with cleaning periods of only dry N_2 exposure in between each concentration shift to ensure a consistent environment for the fabricated QCM sensors. Following this, the second cycle involves a gradual decline in analyte concentrations by 2300 ppm per each shifting step, also accompanied by cleaning intervals. The time for the test chamber to reach the desired RH concentration is experimentally evaluated. The duration required to attain the targeted level is indicated by the shift in sensors resonant frequencies, as shown in Figure 40, and it is found to not exceed 800 seconds. The design of the experimental pattern, illustrated in Figure 39,

incorporates the findings from the study conducted to determine the time needed for the environment to reach the saturation status.

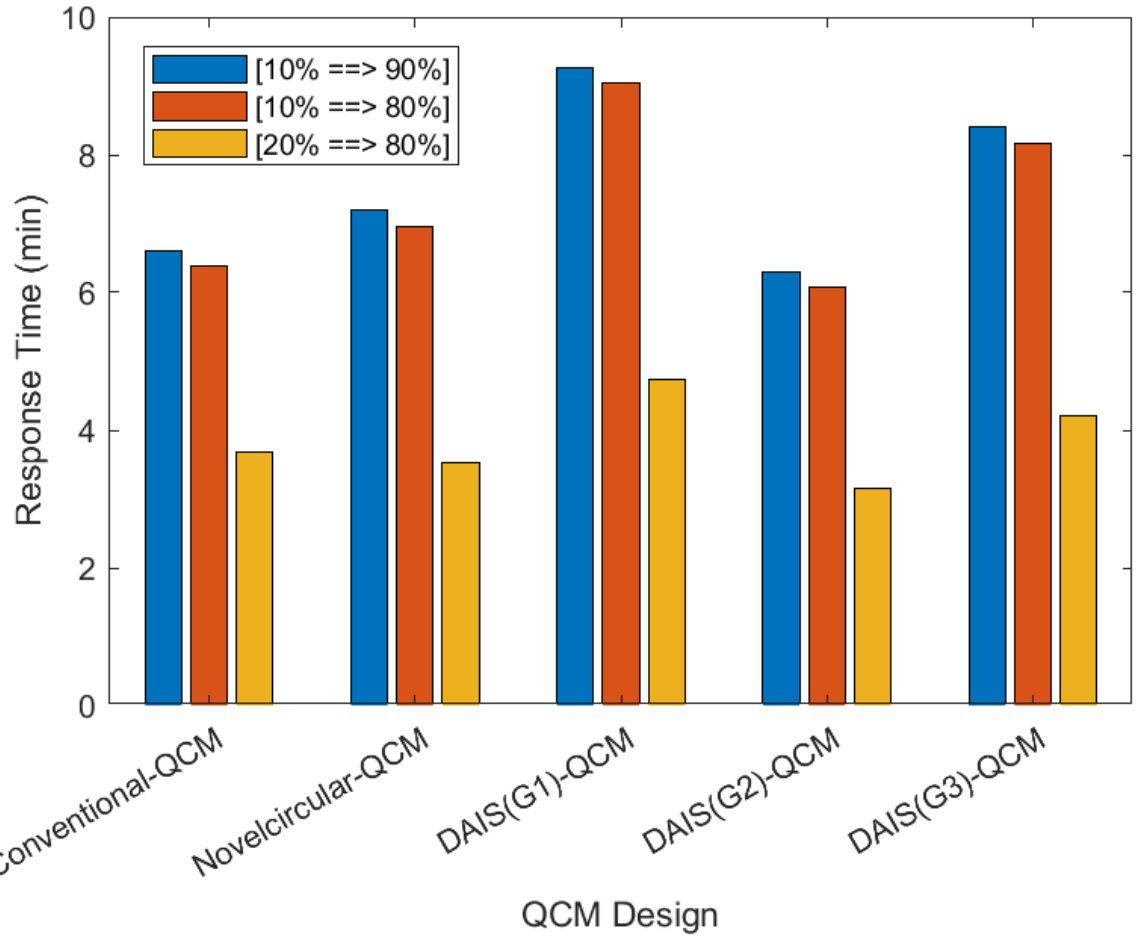

Figure 40. Bar graph of experimental results revealing the required time to reach saturation levels, which is found to not exceed 800 seconds indicated by the shift in sensors resonant frequencies.

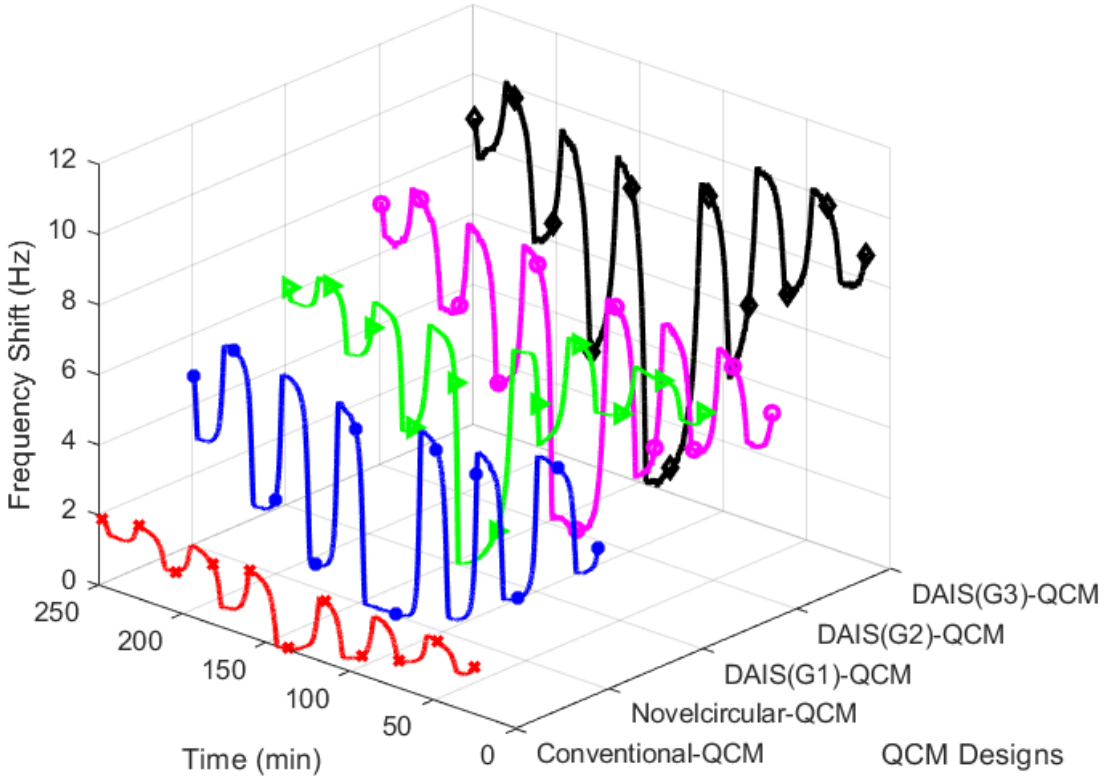

Figure 41. 3D plot of experimental results illustrating the responses of QCMs to variations in target analyte RH, which is modulated to follow a distinct pattern.

The frequency shift responses for RH concentrations ranging from 2300 ppm to 11500 ppm are presented in Figure 41. The proposed designs are found from the experimental results to outperform the conventional design. The enhanced is attributed to the strategic utilization of energy trapping effect by maximizing the corresponding regions where the energy is localized. The DAIS(G3)-QCM exhibits the highest response across all RH concentrations, achieving higher shift in its resonant frequency of over 5 times compared to the conventional QCM, as illustrated in Figure 42. followed by DAIS(G2)-QCM. DAIS(G1)-QCM and Novelcircular-QCM demonstrate comparable performances, with DAIS(G1)-QCM showcasing higher frequency shifts at high RH

concentrations while the latter exhibits a better response at lower concentrations compared to DAIS(G1)-QCM.

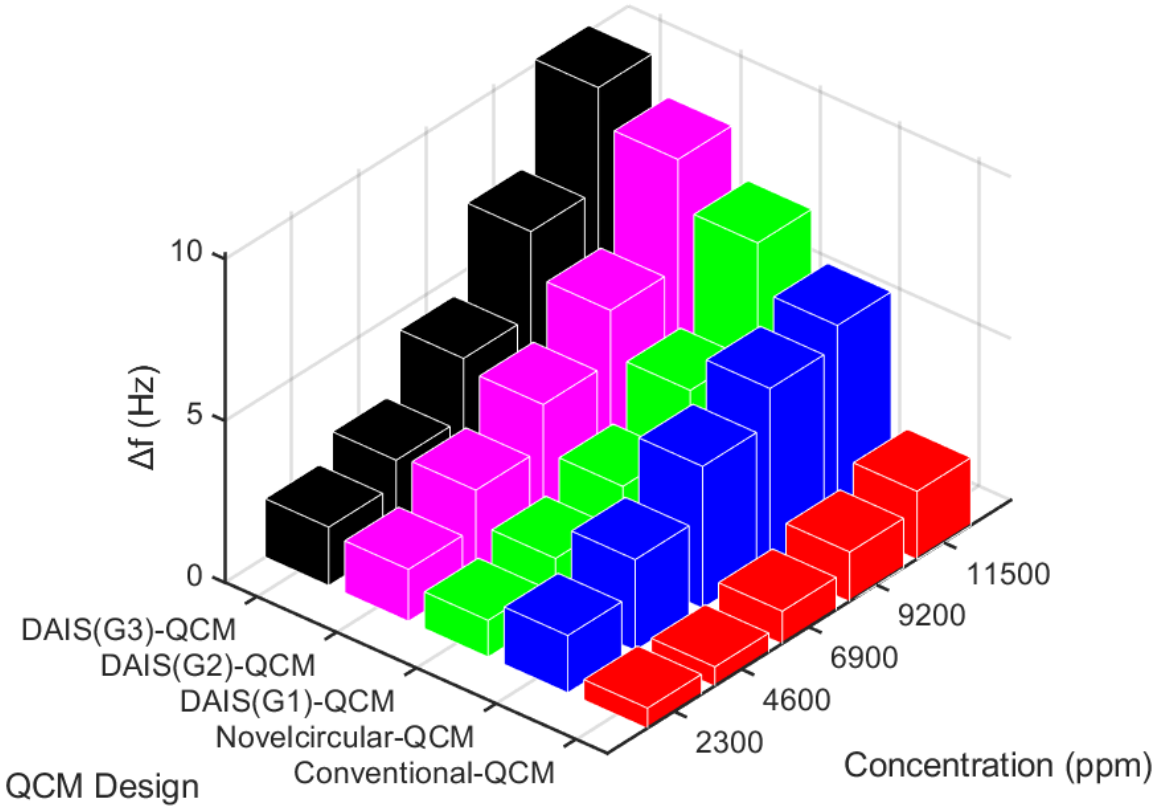

Figure 42. 3D bar graph of experimental results presenting a comparative frequency shift characterization of the candidate QCM designs for RH concentrations 2300, 4600, 6900, 9200, 11500 ppm.

6.3 Experimental Process Phase II: QCM for VOC Detection

In applications of VOC detection, the presence of sensing layer atop gas sensors plays a crucial role. The targeted VOCs, which are present in low concentrations in complex environments, require an effective detection methodology. Therefore, the gas sensors are coupled with a sensing layer to facilitate the adsorption process of the target molecules. The sensing layer materials span a wide spectrum, including metal oxides, functionalized carbon allotropes, and polymers. Among these, polymers are widely

adopted as sensing materials in gas sensing applications due to their simplicity in preparation and commercial availability. The fabricated QCM sensors are coated with a polymer sensing layer, selected to be Polyvinylpyrrolidone (PVP) for its reported applicability in similar characterization works [131]. The sensing material solution is prepared by dissolving 100 mg of PVP, sourced from Polysciences, Inc. (catalog# 01052-250), in 10 mL of methanol to produce a 0.1 weight percent (Wt.%) solution. The solution then undergoes 20 minutes of sonication to ensure the complete dissolution of the polymer. The deposition of the PVP polymer is achieved via spin coating technique, with specifications listed in Table 10. 100 µL of the solution is deposited, resulting in an approximate thickness of 0.1 µm. The thickness of the polymer sensing layer is evaluated using the following formula [131]:

$$T \approx \eta^{\frac{1}{3}} \times \omega^{-at} \tag{23}$$

Table 10: Adjusted parameters of spinner device.

Parameter	**Value**
Spin speed (ω)	1500 rpm
Duration (t)	60 sec
Acceleration (a)	010

Phase II commences with evaluating the sensors response to the same analyte as in phase I, at two modulated concentrations of 0 ppm and 11500 ppm. An increase in the frequency shift response is observed in sensors post-coating with the polymer sensing

layer, compared to uncoated sensors at the same RH concentration levels. This increase in frequency shift is attributed to the presence of the polymer sensing layer, which in turn facilitates the adsorption of a greater number of molecules. Table 11 lists the frequency shifts of the QCM designs, responding to a shift in RH concentration from 0 ppm to 11500 ppm. The QCM sensors, featuring the unique designs again exhibit an enhanced sensitivity in response to identical target analyte exposure as the conventional QCM. This is indicated by the acquired shift in sensor resonant frequency. The validated enhanced sensing performance exhibited by the DAIS designs emphasizes the efficacy of leveraging the energy trapping effect for mass loading area. The approach of maximizing the energy trapping effect region by replacing the conventional singular circular electrode with a strategically distributed smaller electrode offers a beneficial impact on the sensing capability of the QCM sensor.

Table 11: Frequency shifts for polymer- coated QCM sensors responding to shift in RH concentration from 0 to 1500 ppm.

Design	**Frequency shift (Hz)**
Conventional-QCM	69.3
Novelcircular-QCM	77.1
DAIS(G1)-QCM	70.1
DAIS(G2)-QCM	79.9
DAIS(G3)-QCM	91.5

The measurements conducted in phase II are centered on validating the enhanced sensitivity of the proposed QCMs in detecting varying concentrations of VOC target analyte. Methanol, a volatile organic compound, is introduced into the test chamber reaching saturation at regulated concentration level listed in Table 12. The resonant frequency values of the sensors reacting to methanol concentrations following the designed pattern, are plotted in Figure 43. The experimental results, illustrated as a comparative frequency shift characterization in Figure 44, reveal the superior performance of proposed DAIS QCMs in response to identical concentrations of methanol. Among DAIS QCMs, DAIS(G3) exhibits the best performance across all concentration levels achieving frequency shifts of 41, 59, 77, 96, and 116 Hz while the conventional QCM experiences frequency shifts of 31, 44, 58, 72, and 89 Hz reacting to identical methanol concentration levels 12600, 25200, 37800, 50500, and 63100 ppm. Furthermore, DAIS QCMs, including DAIS(G1)-QCM, DAIS(G2)-QCM, and DAIS(G3)-QCM exhibit a uniform frequency shift slope compared to the QCMs featuring a conventional single circular electrode. This uniform in frequency shift slope further underscores the enhanced performance of the proposed QCMs owing to their unique designs.

Table 12: Regulated flow rates and adjusted methanol concentrations injected into the test chamber.

RH flow rate (sccm)	BKG flow rate (sccm)	Concentration (ppm)
10	90	12600
20	80	25200
30	70	37800
40	60	50500
50	50	63100

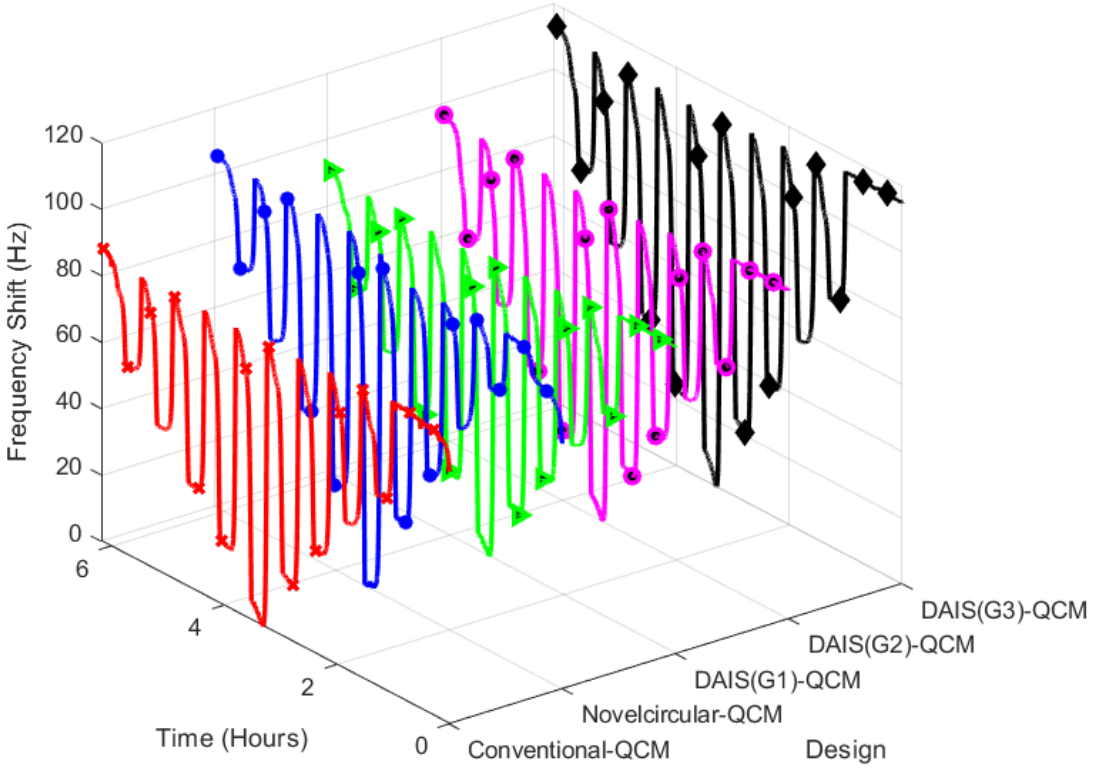

Figure 43. 3D plot of experimental results illustrating the response of both DAIS and conventional QCMs to variation in VOC target analyte methanol.

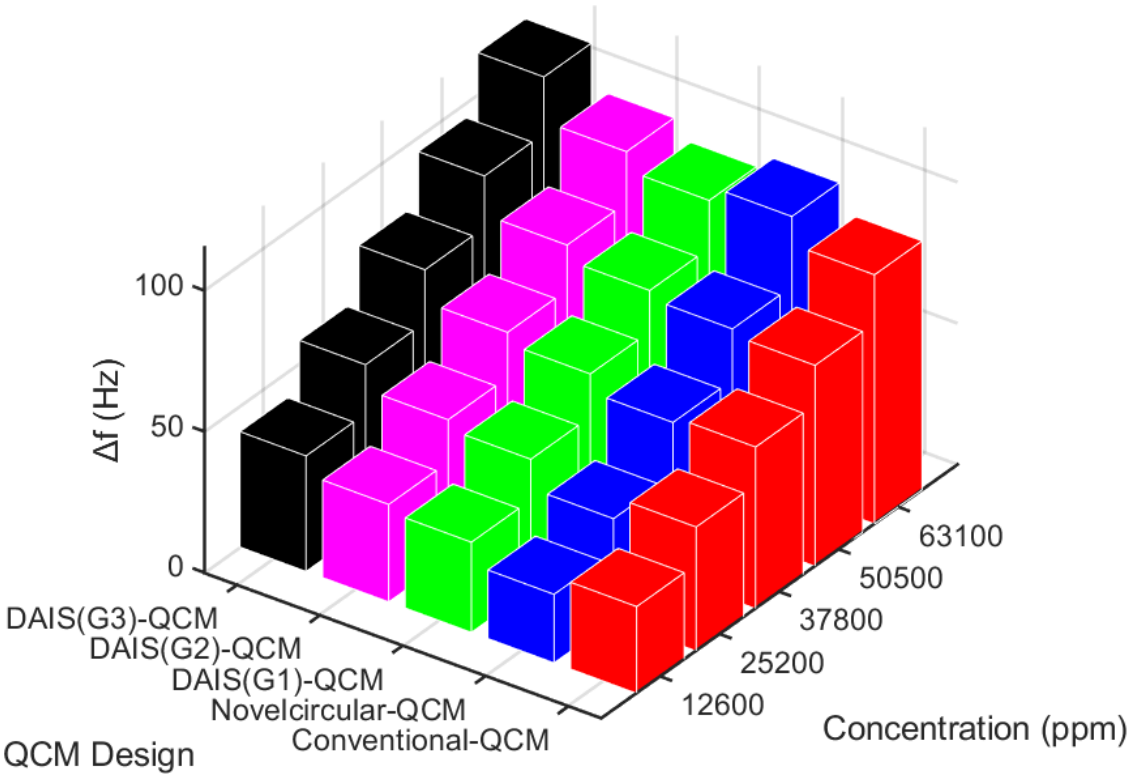

Figure 44. 3D bar graph of experimental results illustrating a Comparative frequency shift characterization for methanol concentrations 12600, 25200, 37800, 50500, and 63100 ppm.

Further experiments are conducted to evaluate sensors performance in response to lower concentrations of VOC target analyte, as illustrated in Figure 45. For this purpose, ethanol, a volatile organic compound, is selected to serve as a proof of concept. The concentrations are modulated at lowest levels available in Plasmionique FLO07-TSV system. Table 13 lists the regulated flow rates and their corresponding concentrations. The experimental results, as illustrated in Figure 46, further emphasis the enhanced sensing performance of DAIS QCMs. The DAIS(G3)-QCM achieves the highest frequency shifts of 19, 21, 23, 25, and 27 Hz while the conventional QCM has frequency sifts of 18, 19, 20, 22, and 23 Hz in response to ethanol concentrations 1100, 2300, 3400, 4600, and 5700 ppm. The replacement of the conventional electrode with smaller circular

electrodes in DAIS design in order to maximize the energy trapping effect region, results in enhancements in QCM sensor ability to detect even low concentrations of target analytes in comparison with the QCM sensors that feature conventional topology.

Table 13: Regulated flow rates and adjusted ethanol concentrations injected into the test chamber.

RH flow rate (sccm)	**BKG flow rate (sccm)**	**Concentration (ppm)**
2	98	1100
4	96	2300
6	94	3400
8	92	4600
10	90	5700

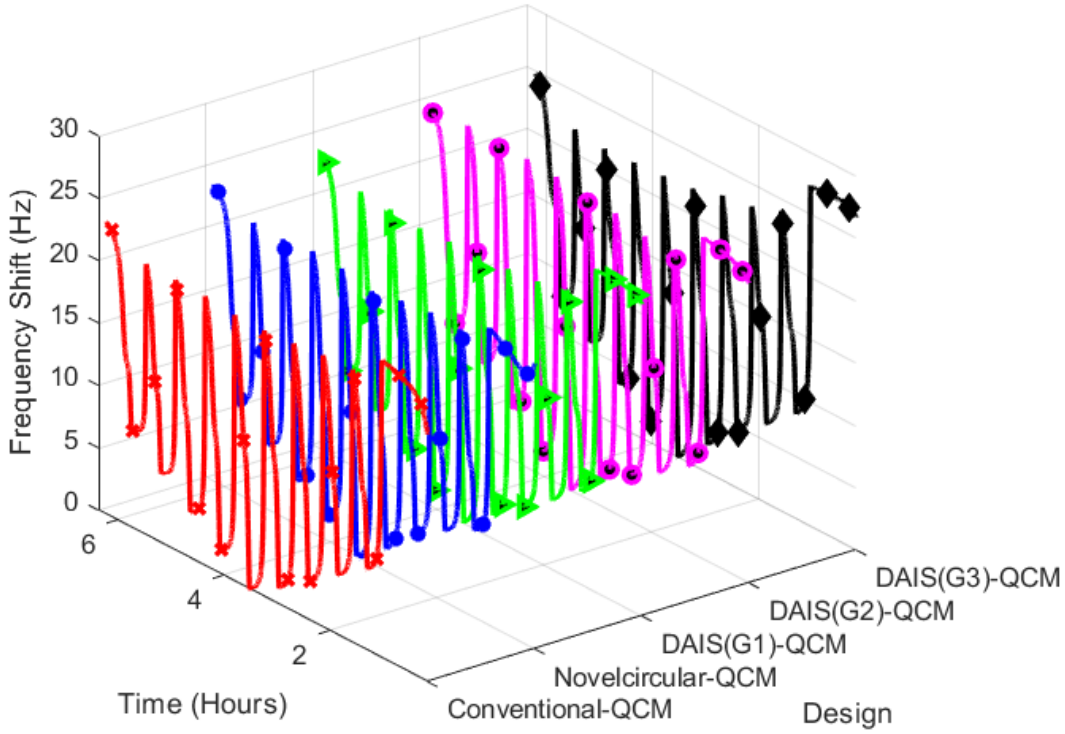

Figure 45. 3D plot of experimental results illustrating the response of both DAIS and conventional QCMs to variation in VOC target analyte ethanol.

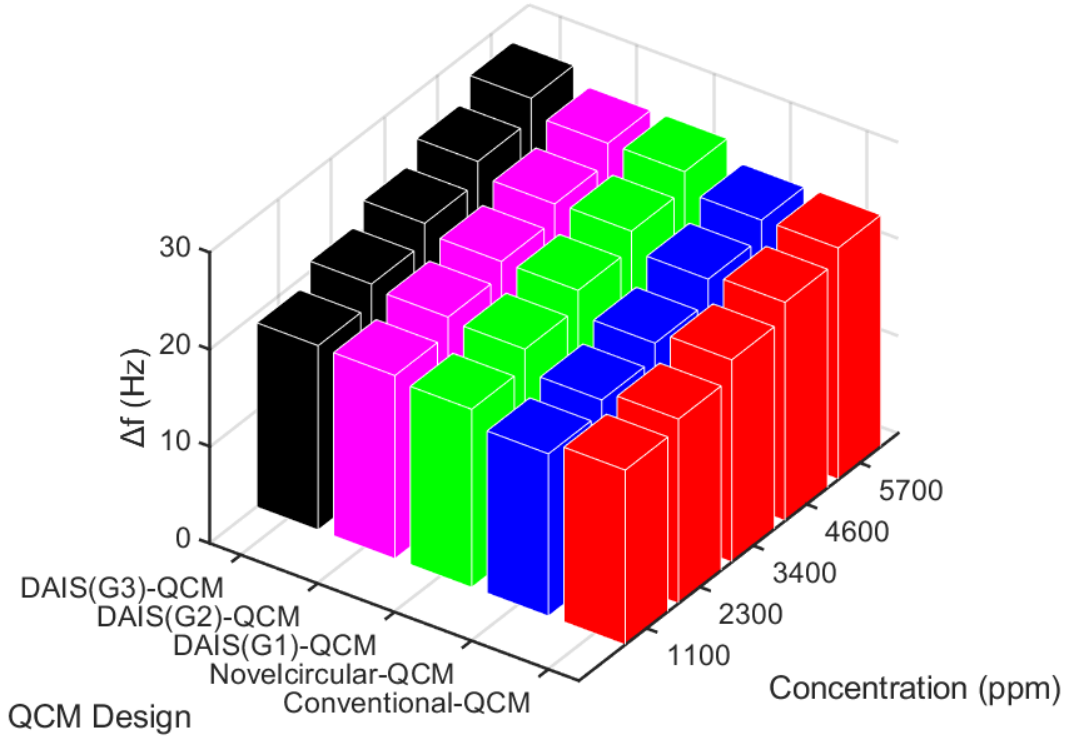

Figure 46. 3D bar graph of experimental results illustrating a Comparative frequency shift characterization for ethanol concentrations 1100, 2300, 3400, 4600, and 5700 ppm.

CHAPTER 7

Conclusion and Proposed Future Work

In this thesis, the development of QCM sensors as a sensing technology to be employed in wide scope of applications is presented. Through FEA simulations, the impact of energy trapping effect in QCM sensor is investigated with the aim of enhancing sensor mass sensitivity. The conducted investigation results in the novel concept of DAIS which based on replacing the conventional topology of QCM, a single circular electrode, with smaller circular electrodes to maximize the energy trapping effect for mass loading area. This enhancement not only improves sensor mass sensitivity but also its distribution uniformity, which is represented by a practical model equivalent to AUC, where the amplitude of vibration peaks at the center of the electrode and reduces in a gaussian pattern moving towards the edges of the active electrode area. Simulation outcomes demonstrate that replacing of the conventional topology with smaller electrodes achieves an enhancement in mass sensitivity. The novel proposed QCM sensor is then fabricated to validate their superior sensing performances compared to the conventional QCM sensor that serves as a reference throughout the entire characterization process. Various target analytes with differing concentrations are precisely introduced to a designed test chamber through a system for regulated gas injection. Additionally, high-resolution frequency monitor is used to capture real-time resonant frequencies during the experimental process. The characterisation of sensors performance by observing their frequency shifts in response to variant concentrations of target analytes, experimentally validate the theoretical models. This emphasises the outcome of the conducted FEA simulations where the strategic adoption of smaller electrodes, featuring a unique distributed pattern,

maximizes the energy trapping effect region, thereby yields enhancement in sensors mass sensitivity, the primary focus in this thesis.

The introduced concept of holds a promising avenue for enhancing the sensing capabilities of QCM sensor by improving it mass sensitivity. However, the optimization of QCM sensors includes improving sensor selectivity and sensor's signal-to-noise ratio (SNR). To enhance selectivity, utilization of sensor array is commonly employed technology to address limitations in detecting specific target analyte in complex environment [4]. Multi-transduction-mechanism technology is another promising approach introduced to enhance sensor performance and reduce the number of required sensors in arrays, achieving miniaturization by combing multiple transduction mechanisms into a signal substrate for increased degrees of freedom [15]. The validated QCM sensor, featuring a unique design derived from the novel concept of DAIS, can be integrated into the optimization of sensing technologies in the next generation of sensors to meet evolving needs in various fields, including medical, industrial, and environmental applications.

REFERENCES/BIBLIOGRAPHY

[1] A. Dan and W. Id, “Application of Electronic-Nose Technologies and VOC-Biomarkers for the Noninvasive Early Diagnosis of Gastrointestinal Diseases,” *Sensors 2018, Vol. 18, Page 2613*, vol. 18, no. 8, p. 2613, 2018, doi: 10.3390/S18082613.

[2] J. D. Fenske and S. E. Paulson, “Human breath emissions of VOCs,” *J Air Waste Manag Assoc*, vol. 49, no. 5, pp. 594–598, 1999, doi: 10.1080/10473289.1999.10463831.

[3] C. Lemaitre-Guillier *et al.*, “VOCs Are Relevant Biomarkers of Elicitor-Induced Defences in Grapevine,” *Molecules 2021, Vol. 26, Page 4258*, vol. 26, no. 14, p. 4258, Jul. 2021, doi: 10.3390/MOLECULES26144258.

[4] G. C. A. Raj, Y. E. Elnemr, P. Munirathinam, Y. Birjis, C. Love, and A. Emadi, “Polymer-Based Virtual Sensor Array Leveraging Fringing Field Capacitance for VOC Detection.,” *Proceedings of IEEE Sensors*, pp. 1–4, 2023, doi: 10.1109/SENSORS56945.2023.10324856.

[5] “What are volatile organic compounds (VOCs)? | US EPA.” Accessed: Jul. 08, 2023. [Online]. Available: https://www.epa.gov/indoor-air-quality-iaq/what-are-volatile-organic-compounds-vocs

[6] S. Swaminathan and A. Emadi, “Design and Analysis of a Novel Quartz Crystal Microbalance Utilizing Distributed Mass Loading Area for Improved Sensitivity,” *IEEE Sens J*, vol. 23, no. 6, pp. 5643–5649, Mar. 2023, doi: 10.1109/JSEN.2023.3242172.

[7] L. Kosuru, A. Bouchaala, N. Jaber, and M. I. Younis, “Humidity Detection Using Metal Organic Framework Coated on QCM,” *J Sens*, vol. 2016, 2016, doi: 10.1155/2016/4902790.

[8] A. Afzal, A. Mujahid, R. Schirhagl, S. Z. Bajwa, U. Latif, and S. Feroz, “Gravimetric Viral Diagnostics: QCM Based Biosensors for Early Detection of Viruses,” *Chemosensors 2017, Vol. 5, Page 7*, vol. 5, no. 1, p. 7, Feb. 2017, doi: 10.3390/CHEMOSENSORS5010007.

[9] K. Liu and C. Zhang, “Volatile organic compounds gas sensor based on quartz crystal microbalance for fruit freshness detection: A review,” *Food Chem*, vol. 334, p. 127615, Jan. 2021, doi: 10.1016/J.FOODCHEM.2020.127615.

[10] M. H. Zarifi, A. Sohrabi, P. M. Shaibani, M. Daneshmand, and T. Thundat, “Detection of volatile organic compounds using microwave sensors,” *IEEE Sens J*, vol. 15, no. 1, pp. 248–254, 2015, doi: 10.1109/JSEN.2014.2345477.

[11] S. Swaminathan and A. Emadi, “Design and Analysis of a Novel Quartz Crystal Microbalance Utilizing Distributed Mass Loading Area for Improved Sensitivity,” *IEEE Sens J*, Mar. 2023, doi: 10.1109/JSEN.2023.3242172.

[12] R. Epping and M. Koch, “On-Site Detection of Volatile Organic Compounds (VOCs),” *Molecules 2023, Vol. 28, Page 1598*, vol. 28, no. 4, p. 1598, Feb. 2023, doi: 10.3390/MOLECULES28041598.

[13] “Volatile Organic Compound Gas Detectors | VOC Monitor.” Accessed: Aug. 23, 2023. [Online]. Available: https://www.internationalgasdetectors.com/gases/volatile-organic-compounds/

[14] A. D. Wilson and M. Baietto, “Applications and Advances in Electronic-Nose Technologies,” *Sensors (Basel)*, vol. 9, no. 7, p. 5099, 2009, doi: 10.3390/S90705099.

[15] Y. E. Elnemr *et al.*, “Multi-Transduction-Mechanism Technology, an Emerging Approach to Enhance Sensor Performance,” *Sensors*, vol. 23, no. 9, p. 4457, May 2023, doi: 10.3390/S23094457.

[16] M. V. Nikolic, V. Milovanovic, Z. Z. Vasiljevic, and Z. Stamenkovic, “Semiconductor Gas Sensors: Materials, Technology, Design, and Application,” *Sensors (Basel)*, vol. 20, no. 22, pp. 1–31, Nov. 2020, doi: 10.3390/S20226694.

[17] R. Papaconstantinou *et al.*, “Field evaluation of low-cost electrochemical air quality gas sensors under extreme temperature and relative humidity conditions,” *Atmos Meas Tech*, vol. 16, no. 12, pp. 3313–3329, Jun. 2023, doi: 10.5194/AMT-16-3313-2023.

[18] Y. Deng, “Sensing Mechanism and Evaluation Criteria of Semiconducting Metal Oxides Gas Sensors,” *Semiconducting Metal Oxides for Gas Sensing*, pp. 23–51, 2019, doi: 10.1007/978-981-13-5853-1_2.

[19] Y. Huang, X. Fan, S. C. Chen, and N. Zhao, “Emerging Technologies of Flexible Pressure Sensors: Materials, Modeling, Devices, and Manufacturing,” *Adv Funct Mater*, vol. 29, no. 12, p. 1808509, Mar. 2019, doi: 10.1002/ADFM.201808509.

[20] Z. Zhai *et al.*, “Metal–Organic Frameworks Materials for Capacitive Gas Sensors,” *Adv Mater Technol*, vol. 6, no. 10, p. 2100127, Oct. 2021, doi: 10.1002/ADMT.202100127.

[21] A. Dos Santos, E. Fortunato, R. Martins, H. Águas, and R. Igreja, “Transduction Mechanisms, Micro-Structuring Techniques, and Applications of Electronic Skin Pressure Sensors: A Review of Recent Advances,” *Sensors 2020, Vol. 20, Page 4407*, vol. 20, no. 16, p. 4407, Aug. 2020, doi: 10.3390/S20164407.

[22] K. Lee *et al.*, “Rough-Surface-Enabled Capacitive Pressure Sensors with 3D Touch Capability,” *Small*, vol. 13, no. 43, p. 1700368, Nov. 2017, doi: 10.1002/SMLL.201700368.

[23] M. L. Hammock, A. Chortos, B. C. K. Tee, J. B. H. Tok, and Z. Bao, “25th Anniversary Article: The Evolution of Electronic Skin (E-Skin): A Brief History, Design Considerations, and Recent Progress,” *Advanced Materials*, vol. 25, no. 42, pp. 5997–6038, Nov. 2013, doi: 10.1002/ADMA.201302240.

[24] P. Bindra and · A Hazra, “Capacitive gas and vapor sensors using nanomaterials,” vol. 29, pp. 6129–6148, 2018, doi: 10.1007/s10854-018-8606-2.

[25] R. Seguine, “Capacitive Sensing Techniques and Considerations,” 2007, Accessed: May 03, 2024. [Online]. Available: http://www.mobilehandsetdesignline.com

[26] “Resistive gas sensor | How it works, Application & Advantages.” Accessed: May 03, 2024. [Online]. Available: https://www.electricity-magnetism.org/resistive-gas-sensor/

[27] A. Mirzaei, S. P. Bharath, J. Y. Kim, K. K. Pawar, H. W. Kim, and S. S. Kim, “N-Doped Graphene and Its Derivatives as Resistive Gas Sensors: An Overview,” *Chemosensors 2023, Vol. 11, Page 334*, vol. 11, no. 6, p. 334, Jun. 2023, doi: 10.3390/CHEMOSENSORS11060334.

[28] A. S. Morris and R. Langari, “Sensor technologies,” *Measurement and Instrumentation*, pp. 381–411, Jan. 2021, doi: 10.1016/B978-0-12-817141-7.00013-X.

[29] Z. Wang *et al.*, “Advances in functional guest materials for resistive gas sensors,” *RSC Adv*, vol. 12, no. 38, pp. 24614–24632, Aug. 2022, doi: 10.1039/D2RA04063H.

[30] Z. M. Rittersma, “Recent achievements in miniaturised humidity sensors—a review of transduction techniques,” *Sens Actuators A Phys*, vol. 96, no. 2–3, pp. 196–210, Feb. 2002, doi: 10.1016/S0924-4247(01)00788-9.

[31] A. S. Fiorillo, C. D. Critello, and A. S. Pullano, “Theory, technology and applications of piezoresistive sensors: A review,” *Sens Actuators A Phys*, vol. 281, pp. 156–175, Oct. 2018, doi: 10.1016/J.SNA.2018.07.006.

[32] D. Yong Park *et al.*, “Self-Powered Real-Time Arterial Pulse Monitoring Using Ultrathin Epidermal Piezoelectric Sensors,” *Advanced Materials*, vol. 29, no. 37, p. 1702308, Oct. 2017, doi: 10.1002/ADMA.201702308.

[33] C. Dagdeviren *et al.*, “Conformable amplified lead zirconate titanate sensors with enhanced piezoelectric response for cutaneous pressure monitoring,” *Nature*

Communications 2014 5:1, vol. 5, no. 1, pp. 1–10, Aug. 2014, doi: 10.1038/ncomms5496.

[34] Q. L. Zhao *et al.*, "Flexible Semitransparent Energy Harvester with High Pressure Sensitivity and Power Density Based on Laterally Aligned PZT Single-Crystal Nanowires," *ACS Appl Mater Interfaces*, vol. 9, no. 29, pp. 24696–24703, Jul. 2017, doi: 10.1021/ACSAMI.7B03929/SUPPL_FILE/AM7B03929_SI_002.AVI.

[35] A. Pimentel, A. Samouco, D. Nunes, A. Araújo, R. Martins, and E. Fortunato, "Ultra-Fast Microwave Synthesis of ZnO Nanorods on Cellulose Substrates for UV Sensor Applications," *Materials 2017, Vol. 10, Page 1308*, vol. 10, no. 11, p. 1308, Nov. 2017, doi: 10.3390/MA10111308.

[36] A. Samouco, A. C. Marques, A. Pimentel, R. Martins, and E. Fortunato, "Laser-induced electrodes towards low-cost flexible UV ZnO sensors," *Flexible and Printed Electronics*, vol. 3, no. 4, p. 044002, Dec. 2018, doi: 10.1088/2058-8585/AAED77.

[37] S. H. Shin, Y. H. Kim, M. H. Lee, J. Y. Jung, and J. Nah, "Hemispherically aggregated BaTiO3 nanoparticle composite thin film for high-performance flexible piezoelectric nanogenerator," *ACS Nano*, vol. 8, no. 3, pp. 2766–2773, Mar. 2014, doi: 10.1021/NN406481K/SUPPL_FILE/NN406481K_SI_003.PDF.

[38] A. L. Kholkin, N. A. Pertsev, and A. V. Goltsev, "Piezoelectricity and crystal symmetry," *Piezoelectric and Acoustic Materials for Transducer Applications*, pp. 17–38, 2008, doi: 10.1007/978-0-387-76540-2_2/COVER.

[39] H. J. Fan *et al.*, "Template-Assisted Large-Scale Ordered Arrays of ZnO Pillars for Optical and Piezoelectric Applications," *Small*, vol. 2, no. 4, pp. 561–568, Apr. 2006, doi: 10.1002/SMLL.200500331.

[40] H. Tang, Z. Zhou, and H. A. Sodano, "Large-scale synthesis of BaxSr1-xTiO3 nanowires with controlled stoichiometry," *Appl Phys Lett*, vol. 104, no. 14, p. 142905, Apr. 2014, doi: 10.1063/1.4870831/125422.

[41] M. Ha *et al.*, "Bioinspired Interlocked and Hierarchical Design of ZnO Nanowire Arrays for Static and Dynamic Pressure-Sensitive Electronic Skins," *Adv Funct Mater*, vol. 25, no. 19, pp. 2841–2849, May 2015, doi: 10.1002/ADFM.201500453.

[42] J. Park, M. Kim, Y. Lee, H. S. Lee, and H. Ko, "Nanomaterials: Fingertip skin-inspired microstructured ferroelectric skins discriminate static/dynamic pressure and temperature stimuli," *Sci Adv*, vol. 1, no. 9, Oct. 2015, doi: 10.1126/SCIADV.1500661/SUPPL_FILE/1500661_SM.PDF.

[43] S. Sripadmanabhan Indira, C. Aravind Vaithilingam, K. Satya Prakash Oruganti, F. Mohd, and S. Rahman, “nanomaterials Nanogenerators as a Sustainable Power Source: State of Art, Applications, and Challenges,” 2019, doi: 10.3390/nano9050773.

[44] Z. Zhao, Y. Lu, Y. Mi, J. Meng, X. Cao, and N. Wang, “Structural Flexibility in Triboelectric Nanogenerators: A Review on the Adaptive Design for Self-Powered Systems,” *Micromachines (Basel)*, vol. 13, no. 10, p. 1586, 2022, doi: 10.3390/mi13101586.

[45] J. Park, Y. Lee, M. Ha, S. Cho, and H. Ko, “Micro/nanostructured surfaces for self-powered and multifunctional electronic skins,” *J Mater Chem B*, vol. 4, no. 18, pp. 2999–3018, May 2016, doi: 10.1039/C5TB02483H.

[46] L. Lin *et al.*, “Triboelectric active sensor array for self-powered static and dynamic pressure detection and tactile imaging,” *ACS Nano*, vol. 7, no. 9, pp. 8266–8274, Sep. 2013, doi: 10.1021/NN4037514/SUPPL_FILE/NN4037514_SI_002.AVI.

[47] D. W. Kim, J. H. Lee, J. K. Kim, and U. Jeong, “Material aspects of triboelectric energy generation and sensors,” *NPG Asia Materials 2020 12:1*, vol. 12, no. 1, pp. 1–17, 2020, doi: 10.1038/s41427-019-0176-0.

[48] Y.-C. Lai *et al.*, “Actively Perceiving and Responsive Soft Robots Enabled by Self-Powered, Highly Extensible, and Highly Sensitive Triboelectric Proximity- and Pressure-Sensing Skins,” *Advanced Materials*, vol. 30, no. 28, p. 1801114, Jul. 2018, doi: 10.1002/ADMA.201801114.

[49] G. Zhao *et al.*, “Transparent and stretchable triboelectric nanogenerator for self-powered tactile sensing,” *Nano Energy*, vol. 59, pp. 302–310, May 2019, doi: 10.1016/J.NANOEN.2019.02.054.

[50] H. Zou *et al.*, “Quantifying the triboelectric series,” *Nature Communications 2019 10:1*, vol. 10, no. 1, pp. 1–9, 2019, doi: 10.1038/s41467-019-09461-x.

[51] J. Zhang, Z. Qin, D. Zeng, and C. Xie, “Metal-oxide-semiconductor based gas sensors: screening, preparation, and integration,” *Physical Chemistry Chemical Physics*, vol. 19, no. 9, pp. 6313–6329, Mar. 2017, doi: 10.1039/C6CP07799D.

[52] S. Swaminathan, “Development of a Novel Quartz Crystal Microbalance based on Distribution of Mass Loading Area for Improving Mass Sensitivity,” 2021. Accessed: May 11, 2023. [Online]. Available: https://scholar.uwindsor.ca/etd/8872

[53] H. Ji, W. Zeng, and Y. Li, “Gas sensing mechanisms of metal oxide semiconductors: a focus review,” *Nanoscale*, vol. 11, no. 47, pp. 22664–22684, Dec. 2019, doi: 10.1039/C9NR07699A.

[54] X. Gao and T. Zhang, “An overview: Facet-dependent metal oxide semiconductor gas sensors,” *Sens Actuators B Chem*, vol. 277, pp. 604–633, Dec. 2018, doi: 10.1016/J.SNB.2018.08.129.

[55] M. A. Han, H. J. Kim, H. C. Lee, J. S. Park, and H. N. Lee, “Effects of porosity and particle size on the gas sensing properties of SnO2 films,” *Appl Surf Sci*, vol. 481, pp. 133–137, Jul. 2019, doi: 10.1016/J.APSUSC.2019.03.043.

[56] L. Xu, W. Zeng, and Y. Li, “Synthesis of morphology and size-controllable SnO2 hierarchical structures and their gas-sensing performance,” *Appl Surf Sci*, vol. 457, pp. 1064–1071, Nov. 2018, doi: 10.1016/J.APSUSC.2018.07.018.

[57] A. Dey, “Semiconductor metal oxide gas sensors: A review,” *Materials Science and Engineering: B*, vol. 229, pp. 206–217, Mar. 2018, doi: 10.1016/J.MSEB.2017.12.036.

[58] D. Kwak, Y. Lei, and R. Maric, “Ammonia gas sensors: A comprehensive review,” *Talanta*, vol. 204, pp. 713–730, Nov. 2019, doi: 10.1016/J.TALANTA.2019.06.034.

[59] A. Joseph, “Design and Analysis of High-Frequency Quartz Crystal Microbalance Sensor Array with Concentric Electrodes and Dual Inverted Mesa Structure for Multiple Gas Detection,” 2019. Accessed: May 11, 2023. [Online]. Available: https://scholar.uwindsor.ca/etd/8168

[60] H. R. Kim, A. Haensch, I. D. Kim, N. Barsan, U. Weimar, and J. H. Lee, “The Role of NiO Doping in Reducing the Impact of Humidity on the Performance of SnO2-Based Gas Sensors: Synthesis Strategies, and Phenomenological and Spectroscopic Studies,” *Adv Funct Mater*, vol. 21, no. 23, pp. 4456–4463, Dec. 2011, doi: 10.1002/ADFM.201101154.

[61] S. S. Kaye and J. R. Long, “Hydrogen storage in the dehydrated prussian blue analogues M 3[Co(CN)6]2 (M = Mn, Fe, Co, Ni, Cu, Zn),” *J Am Chem Soc*, vol. 127, no. 18, pp. 6506–6507, May 2005, doi: 10.1021/JA051168T/SUPPL_FILE/JA051168TSI20050322_015052.PDF.

[62] H. Nazemi *et al.*, “Mass Sensors Based on Capacitive and Piezoelectric Micromachined Ultrasonic Transducers—CMUT and PMUT,” *Sensors 2020, Vol. 20, Page 2010*, vol. 20, no. 7, p. 2010, Apr. 2020, doi: 10.3390/S20072010.

[63] S. S. Ba Hashwan *et al.*, “A review of piezoelectric MEMS sensors and actuators for gas detection application,” *Discover Nano 2023 18:1*, vol. 18, no. 1, pp. 1–41, Feb. 2023, doi: 10.1186/S11671-023-03779-8.

[64] G. Korotcenkov, “Materials for Piezoelectric-Based Gas Sensors,” pp. 307–328, 2013, doi: 10.1007/978-1-4614-7165-3_13.

[65] H. Nazemi, A. Joseph, J. Park, and A. Emadi, “Advanced micro-and nano-gas sensor technology: A review,” *Sensors (Switzerland)*, vol. 19, no. 6, 2019, doi: 10.3390/s19061285.

[66] X. Yang and M. Zhang, “Review of flexible microelectromechanical system sensors and devices,” *Nanotechnology and Precision Engineering*, vol. 4, no. 2, p. 25001, Jun. 2021, doi: 10.1063/10.0004301/253452.

[67] L. Li and Z. J. Chew, “Microactuators: design and technology,” *Smart Sensors and MEMS: Intelligent Devices and Microsystems for Industrial Applications*, pp. 305–348, Jan. 2014, doi: 10.1533/9780857099297.2.305.

[68] F. Sammoura, S. Shelton, S. Akhbari, D. Horsley, and L. Lin, “A two-port piezoelectric micromachined ultrasonic transducer,” *2014 Joint IEEE International Symposium on the Applications of Ferroelectric, International Workshop on Acoustic Transduction Materials and Devices and Workshop on Piezoresponse Force Microscopy, ISAF/IWATMD/PFM 2014*, Oct. 2014, doi: 10.1109/ISAF.2014.6923004.

[69] A. S. Ergun, ; Goksen, G. Yaralioglu, and B. T. Khuri-Yakub, “Capacitive Micromachined Ultrasonic Transducers: Theory and Technology,” *J Aerosp Eng*, vol. 16, no. 2, pp. 76–84, Apr. 2003, doi: 10.1061/(ASCE)0893-1321(2003)16:2(76).

[70] T. A. Emadi and D. A. Buchanan, “Wide range beam steering capability of a 1-D MEMS transducer imager array with directional beam pattern,” *Sens Actuators A Phys*, vol. 202, pp. 193–196, Nov. 2013, doi: 10.1016/J.SNA.2013.01.017.

[71] L. Zhao *et al.*, “A Novel CMUT-Based Resonant Biochemical Sensor Using Electrospinning Technology,” *IEEE Transactions on Industrial Electronics*, vol. 66, no. 9, pp. 7356–7365, Sep. 2019, doi: 10.1109/TIE.2018.2878123.

[72] H. J. Lee, K. K. Park, Ö. Oralkan, M. Kupnik, and B. T. Khuri-Yakub, “CMUT as a chemical sensor for DMMP detection,” *2008 IEEE International Frequency Control Symposium, FCS*, pp. 434–439, 2008, doi: 10.1109/FREQ.2008.4623034.

[73] H. J. Lee, K. K. Park, M. Kupnik, Ö. Oralkan, and B. T. Khuri-Yakub, “Chemical vapor detection using a capacitive micromachined ultrasonic transducer,” *Anal Chem*,

vol. 83, no. 24, pp. 9314–9320, Dec. 2011, doi: 10.1021/AC201626B/SUPPL_FILE/AC201626B_SI_001.PDF.

[74] A. Alassi, M. Benammar, and D. Brett, “Quartz Crystal Microbalance Electronic Interfacing Systems: A Review,” *Sensors 2017, Vol. 17, Page 2799*, vol. 17, no. 12, p. 2799, Dec. 2017, doi: 10.3390/S17122799.

[75] G. Sauerbrey, “Verwendung von Schwingquarzen zur Wägung dünner Schichten und zur Mikrowägung,” *Zeitschrift für Physik*, vol. 155, no. 2, pp. 206–222, 1959, doi: 10.1007/BF01337937/METRICS.

[76] S. N. Songkhla and T. Nakamoto, “Overview of quartz crystal microbalance behavior analysis and measurement,” *Chemosensors*, vol. 9, no. 12, Dec. 2021, doi: 10.3390/CHEMOSENSORS9120350.

[77] S. E. Diltemiz, R. Keçili, A. Ersöz, and R. Say, “Molecular Imprinting Technology in Quartz Crystal Microbalance (QCM) Sensors,” *Sensors 2017, Vol. 17, Page 454*, vol. 17, no. 3, p. 454, Feb. 2017, doi: 10.3390/S17030454.

[78] N. Alanazi, M. Almutairi, and A. N. Alodhayb, “A Review of Quartz Crystal Microbalance for Chemical and Biological Sensing Applications,” *Sens Imaging*, vol. 24, no. 1, pp. 1–33, Dec. 2023, doi: 10.1007/S11220-023-00413-W/TABLES/1.

[79] L. Sartore, M. Barbaglio, L. Borgese, and E. Bontempi, “Polymer-grafted QCM chemical sensor and application to heavy metalions real time detection,” *Sens Actuators B Chem*, vol. 155, no. 2, p. 539, Jul. 2011, doi: 10.1016/J.SNB.2011.01.003.

[80] D. Migoń, T. Wasilewski, and D. Suchy, “Application of QCM in Peptide and Protein-Based Drug Product Development,” *Molecules*, vol. 25, no. 17, Sep. 2020, doi: 10.3390/MOLECULES25173950.

[81] Q. Zhou, C. Zheng, L. Zhu, and J. Wang, “A review on rapid detection of modified quartz crystal microbalance sensors for food: Contamination, flavour and adulteration,” *TrAC Trends in Analytical Chemistry*, vol. 157, p. 116805, Dec. 2022, doi: 10.1016/J.TRAC.2022.116805.

[82] D. A. Buttry and M. D. Ward, “Measurement of Interfaclal Processes at Electrode Surfaces with the Electrochemical Quartz Crystal Microbalance,” *Chem Rev*, vol. 92, no. 6, pp. 1355–1379, Feb. 1992, doi: 10.1021/CR00014A006/ASSET/CR00014A006.FP.PNG_V03.

[83] R. D. O’Neill, S. C. Chang, J. P. Lowry, and C. J. McNeil, “Comparisons of platinum, gold, palladium and glassy carbon as electrode materials in the design of

biosensors for glutamate," *Biosens Bioelectron*, vol. 19, no. 11, pp. 1521–1528, Jun. 2004, doi: 10.1016/J.BIOS.2003.12.004.

[84] D. Johannsmann, A. Langhoff, and C. Leppin, "Studying Soft Interfaces with Shear Waves: Principles and Applications of the Quartz Crystal Microbalance (QCM)," *Sensors 2021, Vol. 21, Page 3490*, vol. 21, no. 10, p. 3490, May 2021, doi: 10.3390/S21103490.

[85] "The Piezoelectric Effect - Piezoelectric Motors & Motion Systems." Accessed: Sep. 03, 2023. [Online]. Available: https://www.nanomotion.com/nanomotion-technology/the-piezoelectric-effect/

[86] T. J. Lewis, "The piezoelectric effect," *Annual Report - Conference on Electrical Insulation and Dielectric Phenomena, CEIDP*, vol. 2005, pp. 717–720, 2005, doi: 10.1109/CEIDP.2005.1560783.

[87] W. Xu, J. Appel, and J. Chae, "Real-time monitoring of whole blood coagulation using a microfabricated contour-mode film bulk acoustic resonator," *Journal of Microelectromechanical Systems*, vol. 21, no. 2, pp. 302–307, Apr. 2012, doi: 10.1109/JMEMS.2011.2179011.

[88] "Piezo Constants | Accelerometer tutorial." Accessed: Sep. 03, 2023. [Online]. Available: https://www.f3lix-tutorial.com/piezo-constants

[89] C. A. Mills, K. T. C. Chai, M. J. Milgrew, A. Glidle, J. M. Cooper, and D. R. S. Cumming, "A multiplexed impedance analyzer for characterizing polymer-coated QCM sensor arrays," *IEEE Sens J*, vol. 6, no. 4, pp. 996–1001, Aug. 2006, doi: 10.1109/JSEN.2006.877936.

[90] X. Su, D. Chen, N. Li, A. C. Stevenson, G. Li, and R. Hu, "A wireless electrode-free QCM-D in a multi-resonance mode for volatile organic compounds discrimination," *Sens Actuators A Phys*, vol. 305, p. 111938, Apr. 2020, doi: 10.1016/J.SNA.2020.111938.

[91] M. C. Dixon, "Quartz Crystal Microbalance with Dissipation Monitoring: Enabling Real-Time Characterization of Biological Materials and Their Interactions," *J Biomol Tech*, vol. 19, no. 3, p. 151, Jul. 2008, Accessed: Sep. 03, 2023. [Online]. Available: /pmc/articles/PMC2563918/

[92] M. Rodahl and B. Kasemo, "A simple setup to simultaneously measure the resonant frequency and the absolute dissipation factor of a quartz crystal microbalance," *Review of Scientific Instruments*, vol. 67, no. 9, pp. 3238–3241, Sep. 1996, doi: 10.1063/1.1147494.

[93] D. Johannsmann, *The Quartz Crystal Microbalance in Soft Matter Research*. in Soft and Biological Matter. Cham: Springer International Publishing, 2015. doi: 10.1007/978-3-319-07836-6.

[94] "Piezoelectric Materials: Crystal Orientation and Poling Direction | COMSOL Blog." Accessed: Sep. 03, 2023. [Online]. Available: https://www.comsol.com/blogs/piezoelectric-materials-crystal-orientation-poling-direction/

[95] Y. Yao, X. Chen, X. Li, X. Chen, and N. Li, "Investigation of the stability of QCM humidity sensor using graphene oxide as sensing films," *Sens Actuators B Chem*, vol. 191, pp. 779–783, Feb. 2014, doi: 10.1016/J.SNB.2013.10.076.

[96] "Fundamentals of Quartz Oscillators Application Note 200-2." Accessed: May 16, 2024. [Online]. Available: https://www.yumpu.com/en/document/view/18115907/fundamentals-of-quartz-oscillators-application-note-200-2

[97] D. Shen, Q. Kang, Y. E. Wang, Q. Hu, and J. Du, "New cut angle quartz crystal microbalance with low frequency–temperature coefficients in an aqueous phase," *Talanta*, vol. 76, no. 4, pp. 803–808, Aug. 2008, doi: 10.1016/J.TALANTA.2008.04.028.

[98] "Quartz Crystal Cuts: AT, BT, SC, CT . . » Electronics Notes." Accessed: Sep. 03, 2023. [Online]. Available: https://www.electronics-notes.com/articles/electronic_components/quartz-crystal-xtal/crystal-resonator-cuts-at-bt-sc-ct.php

[99] V. Matko, "Next generation AT-Cut quartz crystal sensing devices," *Sensors*, vol. 11, no. 5, pp. 4474–4482, May 2011, doi: 10.3390/S110504474.

[100] P. Salzenstein, "Recent progress in the performances of ultrastable quartz resonators and oscillators," *International Journal for Simulation and Multidisciplinary Design Optimization*, vol. 7, p. A8, 2016, doi: 10.1051/SMDO/2016014.

[101] E. K. Miguel, "TEMPERATURE COMPENSATED SC CUT QUARTZ CRYSTAL OSCILLATOR.," *Proceedings of the Annual IEEE International Frequency Control Symposium*, pp. 576–585, 1982, doi: 10.1109/FREQ.1982.200626.

[102] D. K. Bwambok *et al.*, "QCM Sensor Arrays, Electroanalytical Techniques and NIR Spectroscopy Coupled to Multivariate Analysis for Quality Assessment of Food Products, Raw Materials, Ingredients and Foodborne Pathogen Detection: Challenges and Breakthroughs," *Sensors (Basel)*, vol. 20, no. 23, pp. 1–42, Dec. 2020, doi: 10.3390/S20236982.

[103] R. Fernández, M. Calero, Y. Jiménez, and A. Arnau, “A real-time method for improving stability of monolithic quartz crystal microbalance operating under harsh environmental conditions,” *Sensors*, vol. 21, no. 12, Jun. 2021, doi: 10.3390/S21124166/S1.

[104] “Quartz Crystal Microbalance (QCM) - Nanoscience Instruments.” Accessed: Sep. 04, 2023. [Online]. Available: https://www.nanoscience.com/techniques/quartz-crystal-microbalance/

[105] A. A. Vives, “Piezoelectric transducers and applications,” *Piezoelectric Transducers and Applications*, pp. 1–532, 2008, doi: 10.1007/978-3-540-77508-9/COVER.

[106] E. Uttenthaler, M. Schräml, J. Mandel, and S. Drost, “Ultrasensitive quartz crystal microbalance sensors for detection of M13-Phages in liquids,” *Biosens Bioelectron*, vol. 16, no. 9–12, pp. 735–743, 2001, doi: 10.1016/S0956-5663(01)00220-2.

[107] G. Sauerbrey, “Verwendung von Schwingquarzen zur Wägung dünner Schichten und zur Mikrowägung,” *Zeitschrift für Physik*, vol. 155, no. 2, pp. 206–222, 1959, doi: 10.1007/BF01337937/METRICS.

[108] X. Su, Y. J. Wu, and W. Knoll, “Comparison of surface plasmon resonance spectroscopy and quartz crystal microbalance techniques for studying DNA assembly and hybridization,” *Biosens Bioelectron*, vol. 21, no. 5, pp. 719–726, Nov. 2005, doi: 10.1016/J.BIOS.2005.01.006.

[109] S. Kurosawa *et al.*, “Gas sensor using high-frequency quartz crystal microbalance,” *Proceedings of the Annual IEEE International Frequency Control Symposium*, pp. 462–464, 2001, doi: 10.1109/FREQ.2001.956274.

[110] “What is the Sauerbrey equation?” Accessed: Sep. 04, 2023. [Online]. Available: https://www.biolinscientific.com/blog/what-is-the-sauerbrey-equation

[111] M. Onoe, “Effect of energy trapping on performance of QCM,” *Proceedings of the IEEE International Frequency Control Symposium and Exposition*, vol. 2005, pp. 433–441, 2005, doi: 10.1109/FREQ.2005.1573970.

[112] X. Huang, Q. Bai, J. Hu, and D. Hou, “A Practical Model of Quartz Crystal Microbalance in Actual Applications,” *Sensors 2017, Vol. 17, Page 1785*, vol. 17, no. 8, p. 1785, Aug. 2017, doi: 10.3390/S17081785.

[113] H. Jiang, “Finite element analysis on electrode structure of QCM,” *2009 Chinese Control and Decision Conference, CCDC 2009*, pp. 3618–3621, 2009, doi: 10.1109/CCDC.2009.5192819.

[114] C. M. Seed, B. Acharya, and J. Krim, “QCM Study of Tribotronic Control in Ionic Liquids and Nanoparticle Suspensions,” *Tribol Lett*, vol. 69, no. 3, pp. 1–12, Sep. 2021, doi: 10.1007/S11249-021-01461-7/FIGURES/9.

[115] X. Huang, Q. Bai, Q. Zhou, and J. Hu, “The Resistance–Amplitude–Frequency Effect of In–Liquid Quartz Crystal Microbalance,” *Sensors (Basel)*, vol. 17, no. 7, Jul. 2017, doi: 10.3390/S17071476.

[116] D. Li, Z. Xie, M. Qu, Q. Zhang, Y. Fu, and J. Xie, “Virtual Sensor Array Based on Butterworth-Van Dyke Equivalent Model of QCM for Selective Detection of Volatile Organic Compounds,” *ACS Appl Mater Interfaces*, vol. 13, no. 39, pp. 47043–47051, Oct. 2021, doi: 10.1021/ACSAMI.1C13046/ASSET/IMAGES/LARGE/AM1C13046_0007.JPEG.

[117] Y. Seida and M. Ogawa, “Quartz Crystal Microbalance Monitoring of Poly(Vinyl Alcohol) Sol during the Freeze–Thaw Process,” *Journal of Materials Science Research*, vol. 5, no. 3, p. p42, Apr. 2016, doi: 10.5539/JMSR.V5N3P42.

[118] K. C. Vavra, G. Yu, M. Josowicz, and J. Janata, “Magnetic quartz crystal microbalance: Magneto-acoustic parameters,” *J Appl Phys*, vol. 110, no. 1, Jul. 2011, doi: 10.1063/1.3602998.

[119] F. Zhu *et al.*, “A Theoretical Model for Analyzing the Thickness-Shear Vibration of a Circular Quartz Crystal Plate with Multiple Concentric Ring Electrodes,” *IEEE Trans Ultrason Ferroelectr Freq Control*, vol. 68, no. 5, pp. 1808–1818, May 2021, doi: 10.1109/TUFFC.2020.3047808.

[120] P. Wang, J. Su, L. Gong, M. Shen, M. Ruths, and H. Sun, “Numerical simulation and experimental study of resonance characteristics of QCM-P devices operating in liquid and their application in biological detection,” *Sens Actuators B Chem*, vol. 220, pp. 1320–1327, Dec. 2015, doi: 10.1016/J.SNB.2015.07.024.

[121] Z. Lin, C. M. Yip, I. S. Joseph, and M. D. Ward, “Operation of an Ultrasensitive 30-MHz Quartz Crystal Microbalance in Liquids,” *Anal Chem*, vol. 65, no. 11, pp. 1546–1551, Jun. 1993, doi: 10.1021/AC00059A011/ASSET/AC00059A011.FP.PNG_V03.

[122] “AC/DC Module User’s Guide,” 1998, Accessed: Jan. 03, 2024. [Online]. Available: www.comsol.com/blogs

[123] A. Pereira and L. F. Melo, “Monitoring of biofilms in the food and beverage industries,” *Biofilms in the Food and Beverage Industries*, pp. 131–151, Jan. 2009, doi: 10.1533/9781845697167.1.131.

[124] T. W. Schneider *et al.*, “Chemically selective coated quartz-crystal-microbalance (QCM) array for detection of volatile organic chemicals,” *SPIE*, vol. 3539, pp. 85–94, Dec. 1998, doi: 10.1117/12.333735.

[125] nano-purification solutions, “N2 GEN2 Nitrogen Generators - Brochure”.

[126] “IMM-200 | INFICON.” Accessed: Apr. 01, 2024. [Online]. Available: https://www.inficon.com/en/products/thin-film-technology/imm-200

[127] “Research Crystals 1 inch (25.4mm) | INFICON.” Accessed: Apr. 26, 2024. [Online]. Available: https://www.inficon.com/en/products/thin-film-technology/research-crystals-1-inch-254mm

[128] C. Love, “Utilization of Fringing Fields for Improved Impedance-based Gas Detector Sensitivity,” *Electronic Theses and Dissertations*, Jan. 2022, Accessed: May 21, 2023. [Online]. Available: https://scholar.uwindsor.ca/etd/8717

[129] T. Iwata, M. Saeki, Y. Okura, and T. Yoshikawa, “Gas discrimination based on enhanced gas-species related information obtained by a single gas sensor with novel temperature modulation,” *Sens Actuators B Chem*, vol. 354, p. 131225, Mar. 2022, doi: 10.1016/J.SNB.2021.131225.

[130] V. Daněk, “Vapor Pressure,” *Physico-Chemical Analysis of Molten Electrolytes*, pp. 313–326, Jan. 2006, doi: 10.1016/B978-044452116-3/50008-8.

[131] “Spin coating of thin polymer film and thickness determination by ellipsometry”, Accessed: Apr. 26, 2024. [Online]. Available: http://www.semiconductor.net/article/203104-How_to_Minimize_Resist_Usage_During_Spin_Coating.php

VITA AUCTORIS

NAME:	Youssef Ezzat Youssef Elnemr
PLACE OF BIRTH:	SAU
YEAR OF BIRTH:	1997
EDUCATION:	Tanta High School, Tanta, Egypt, 2015
	Çukurova University, B.Sc., Adana, Turkey, 2021
	University of Windsor, M.Sc., Windsor, ON, 2024